Abstract

Title of dissertation: THE EFFECT OF LIQUID COMPRESSIBILITY AND DOMAIN VOLUME ON THE COLLAPSE OF CYLINDRICAL VAPOR CAVITIES

Derrick M. Treichler, Doctor of Philosophy, 2014

Dissertation directed by: Professor Kenneth T. Kiger
Department of Mechanical Engineering

The dynamics of slender vapor cavities is studied experimentally and with a compressible multi-material Euler equation solver. For the computational study, the cavity was approximated as an infinitely long cylinder. Compressibility is shown to be a controlling factor in the dynamics of the cavity collapse, both as a means to limit the amount of fluid mass accelerated and as a source of radiated energy. As a result, cavities reach an invariant collapse time for fluid domains large enough that acoustic waves traveling outward from the cavity wall are unable to return before collapse. The dynamics of the collapse are studied using an inviscid compressible hydrocode and are compared to those given by the incompressible cylindrical analogue of the Rayleigh-Plesset equation. The incompressible solution is known to depend on the size of the domain due to a logarithmic dependence in the governing equation, predicting a monotonically-increasing collapse time with increasing fluid domain size. Thus, for sufficiently large fluid domains, the analytic incompressible solution greatly over-predicts the cavity collapse time observed in the compressible calculation. Using the results of this study, a compressibility-limited collapse time can be predicted for a cylindrical bubble using the incompressible model, providing a rational upper limit for the effective domain size often used in slender-body approximation models.

In the experimental study, supercavitating projectiles with a mass of 55 g, and cavitator radii of 3 and 6 mm were fired vertically into a shallow hydroballistics

tank at velocities between 194 and 434 m/s. Cavity morphology and dynamics are extracted from high-speed video footage with two image processing techniques. Resulting cavity radial flow histories are compared to a model adapted from Bergmann et al. (2009). The model uses the volume of the hydroballistics tank as the upper limit for the amount of fluid available for cavity expansion and collapse. It accurately predicts cavity radial dynamics where local three-dimensionality (e.g. surface seal and axial flow) does not dominate the flow. The resulting model is capable of predicting gross cavity behavior and collapse mode. For cavities where the collapse is primarily radial, the model accurately predicts the time and location of collapse. These predictions could facilitate estimates of cavity collapse loading on adjacent structures.

The Effect of Liquid Compressibility and Domain Volume on the Collapse of Cylindrical Vapor Cavities

by

Derrick M. Treichler

Dissertation submitted to the Faculty of the Graduate School of the
University of Maryland, College Park in partial fulfillment
of the requirements for the degree of
Doctor of Philosophy
2014

Advisory Committee:

Professor Kenneth T. Kiger, Chair
Professor Balakumar Balachandran
Professor James H. Duncan
Professor Johan Larsson
Professor Richard V. Calabrese, Dean's representative

Preface

This work was supported by the Office of Naval Research under grant number N00014-06-1-0151, Mr. Brian Almquist, Program Manager.

Acknowledgments

I would like to acknowledge my parents for the support they have provided me over the years. From an early age, they instilled the sense of curiosity, the thirst for knowledge, and the drive to do my absolute best that have stayed with me to this day.

I would also like to thank my wife, Whitney. She has been with me since (quite literally) day one at the University of Maryland. Whenever my confidence has faded, she has been there to get me back on my feet. Without her unconditional support, I would not have made it this far.

Finally, I wish to express my immense gratitude to my advisor, Dr. Kenneth Kiger. I have deeply enjoyed working so closely with him over the course of these many years. His passion for teaching and genuine care for his students has made this pursuit a truly fulfilling experience.

Contents

List of Figures

List of Tables

Chapter 1

Introduction

Vapor cavities in liquids are a phenomenon often associated with high-energy events. They can be generated by a variety of sources on a wide range of scales, from microbubbles formed via focused laser radiation or ultrasonic fields [4, 5], to the cavities formed by supercavitating projectiles [3, 6], up to the very large bubbles that are be formed by the detonation of explosives underwater [7, 8]. These cavities come in an array of shapes, from the approximately spherical cavities formed by underwater detonation, to the approximately cylindrical cavities formed by line charges and supercavitating projectiles, to the asymmetric cavities formed by shape charges.

Due to their relative ubiquity, much attention has been given to spherical cavities. Lord Rayleigh is credited with first solving the problem of a cavity collapsing in a very large mass of incompressible fluid [9]. His elegant formulation is often sufficient for predicting the primary expansion and collapse of a roughly spherical bubble. The assumption of incompressibility, however, neglects damping of bubble oscillation resulting from the radiation of acoustic waves. Later work by Keller and Herring took compressibility into account, allowing for the first-order prediction of the subsequent rebound and collapse cycles of a spherical bubble[8, 10, 11, 12].

The current work is motivated by shallow water entry of supercavitating projectiles, such as the one shown in Figure 1.1. These projectiles create very slender, unsteady cavities that are better approximated by cylindrical rather than spherical geometry. Due to the specialized nature of this flow, less consideration has been given to this problem in comparison to the spherical case.

An incompressible, Rayleigh-like solution is possible for a axisymmetric cylin-

Figure 1.1: Supercavitating anti-mine projectile.

drical bubble [13]. Combining many of these one-dimensional solutions together with an appropriate time delay has been a common means of modeling the transient cavity created by a supercavitating projectile [3, 6]. One difficulty, however, stems from the fact that the governing equation for the local radial motion of the cavity wall includes a logarithmic dependence on a dimensionless parameter, $S^\star = S/R_{max}$, where S is the location of the far-field boundary and R_{max} is the maximum cavity radius. Unlike the spherical formulation (which has a power law decay), the logarithmic term in the cylindrical case diverges as the domain size approaches infinity. Consequently, for an unbounded fluid, the incompressible formulation predicts a static liquid-vapor interface that never collapses.

This indicates that some modification is required to bring the predicted dynamics in line with observed behavior. Although often idealized as uncoupled one-dimensional layers of incompressible fluid, in reality, the dynamics are practically limited by the combination or dominance of three possible behaviors:

1. volume-limited behavior,
2. compressibility-limited behavior, and/or
3. radial-axial flow coupling.

As will be shown, in cases where the flow is volume-limited, the amount of fluid "available" for cavity dynamics is set by the size of the size physical volume, e.g. a hydroballistics tank, as is illustrated in Figure 1.2a. However, if the physical volume is large enough, the flow becomes compressibility-limited, as the amount of

fluid involved in the cavity dynamics is dictated by the speed of sound in the fluid, as is shown in Figure 1.2b. The third possibility is the dominance of radial-axial flow coupling. In real cavities, the flow is never purely radial, and the three-dimensional motion of the expanding leading edge and collapsing tail (e.g. jetting) of the bubble creates an effective limit on the participating volume, as demonstrated in Figure 1.2c. This mechanism has been covered in depth by Bergmann and Lohse, whose model is discussed and applied in Chapter 4 [2, 14, 15].

The current work seeks to more rigorously explore the effects of finite volume and compressibility on the collapse of idealized cylindrical vapor cavities through a computational parametric study and a series of related experiments. The end result will be greater insight into how to appropriately choose a far-field boundary location (i.e. value of $S^\star$) to accurately predict the collapse of a cylindrical bubble.

An examination of the governing equation for an idealized cylindrical bubble in an incompressible fluid leads to an important question: when will a cylindrical cavity behave as though it is in an unbounded fluid? That is to say, assuming purely radial flow, what is the upper bound on the amount of fluid that can participate in cavity dynamics? Work aiming to provide an answer this question is presented in Chapter 3. This study simplifies the ballistic vapor cavities by approximating them as infinitely long cylinders. These cavities are simulated using a compressible multi-material Euler equation solver, Gemini, over a wide range of ambient pressures. We find that above a critical domain size (i.e. value of $S^\star$), the cavity collapse behavior becomes independent of the amount of fluid available for the collapse motion. The critical value of $S^\star$ is a function of the driving pressure difference and corresponds to the case where an acoustic wave originating at the cavity wall has enough time to travel to the distant radial boundary of the liquid domain, be reflected, and return to the cavity boundary at the time of final collapse. The result of this work is an empirical relationship between driving pressure and maximum collapse time. This allows the use of the incompressible formulation to model cavity dynamics.

Chapter 4 presents an analysis of high-speed water entry experiments. In this

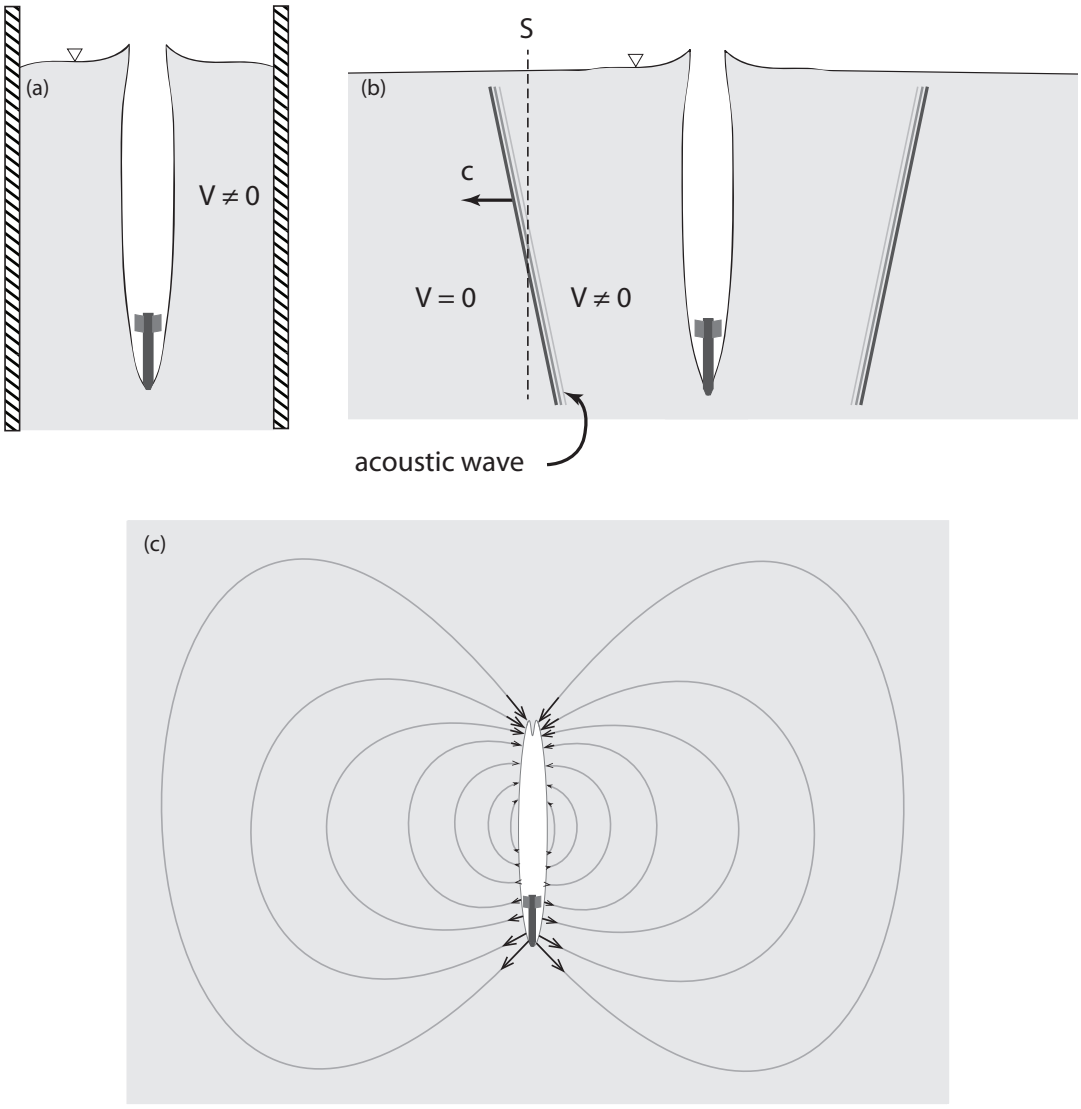

Figure 1.2: Schematic illustration for a supercavitating projectile entering water. (a) A volume-limited case, in which the flow is controlled by the size of an experimental volume. (b) A compressibility-limited case, in which the fluid flow is controlled by the propagation of an acoustic wave moving at a finite sound speed, c. (c) A case in which three-dimensional effects are important. At lower Froude numbers, the cavity is expanding at its nose while, not far away, the tail of the cavity collapses, forming a re-entrant jet.

work, a 55 g blunt-nosed supercavitating dart with a nominal cavitator radius of 3 mm was fired vertically into a 1 m deep by 1.2 m square water tank at velocities between 194 and 434 m/s, yielding a cavitation number, $Ca = 2\Delta P/\rho v_o^2$, on the order of 2×10^{-3}. Cavity profiles were extracted from high-speed video to facilitate analysis of the cavity dynamics. Two distinct collapse modes were observed. At higher velocities, which produce tapered cavities, the cavity detaches from both the free surface and the target plate, with both ends collapsing axially and meeting in the middle of the volume. At lower entry velocities, the cavity is slender with a less pronounced taper. The resulting collapse is primarily radial, with the cavity closing at each depth in sequence, in a top-down fashion which follows the projectile.

An existing model is adapted from the work of Bergmann et al., who studied the dynamics of cavities created by a plunging disk at Froude numbers less than 500 [2, 15]. The adapted model presented here takes into consideration the effect of confinement by the tank walls, matching the observed cavity dynamics well in regions where local three-dimensional effects do not dominate. We conclude from these results that the collapse behavior of the experimental cases was influenced by the size of the hydroballistic tank. The model is then used to further explore the parameter space, considering the effect of changes in cavitator radius, projectile mass, initial velocity, and tank hydraulic radius. This model is capable of predicting the general collapse mode: top-to-bottom or bottom-to-top. However, neglecting local three-dimensionality, in particular at the free surface where surface seal and the re-entrant jet dominate the flow, means that the specifics of the collapse (such as the timing and precise location of collapse) are not always accurately predicted. Despite this shortcoming, the results are still useful to determine conditions that would cause adjacent structures to see loads due to cavity collapse.

Chapter 2

Literature Review

2.1 Modeling Spherical Cavities

2.1.1 The Rayleigh Model

At the root of all studies of cavity collapse dynamics is the seminal work by Lord Rayleigh, who solved the problem of the collapse of an empty cavity in a large volume of incompressible liquid [9].

Assuming spherical symmetry and an inviscid fluid, Rayleigh started with the equations of continuity,

$$\nabla \cdot \vec{u} = 0, \tag{2.1}$$

and momentum,

$$\frac{\partial \varphi}{\partial t} + \frac{1}{2}u_r^2 + \frac{p}{\rho} = \frac{p_\infty}{\rho}, \tag{2.2}$$

where $\vec{u} = u_r \hat{r}$ is the radial velocity vector, and the velocity potential, φ, is defined such that $u_r = \partial\varphi/\partial r$. Bernoulli's equation is evaluated at the two known points on the streamline: the bubble interface at $r = R$, and a far field reference point, $r \to \infty$ where the pressure is some reference pressure, p_∞, and the velocity field vanishes. A kinematic boundary condition is required to arrive at an equation for the dynamics of the bubble wall,

$$u_r(r = R(t), t) = \dot{R}(t), \tag{2.3}$$

where $R(t)$ is the radius of the bubble as a function of time, and the dot denotes a derivative with respect to time. Using this boundary condition, continuity requires that

$$u_r = \frac{R^2 \dot{R}}{r^2}. \tag{2.4}$$

Integrating Equation 2.4 from $r = R$ to $r = \infty$, the velocity potential, φ is

$$\varphi = -\frac{R^2\dot{R}}{r}. \tag{2.5}$$

To complete the formulation, the forces acting on the bubble surface must be considered. There are four forces which are balanced at the bubble-liquid interface:

1. the ambient pressure in the liquid,
2. the internal pressure of the bubble,
3. the surface tension at the bubble-liquid interface, and
4. the viscous force of the liquid.

This force balance can be written as

$$p(R) = p_i - \frac{2\sigma + 4\mu\dot{R}}{R}, \tag{2.6}$$

where p_i is the internal pressure of the bubble, σ is the surface tension, and μ is the viscosity of the ambient liquid. In reality, the internal pressure of the bubble can vary spatially. Driven bubbles can collapse strongly enough that energy focusing in the cavity gas leads to the emission of light. This has been studied extensively in the field of sonoluminesence [16, 17]. In the work presented in this thesis, however, the pressure inside the bubble is assumed to be uniform. Further, it is a simple matter to adjust p_i such that it varies with time or bubble radius (e.g. for a bubble filled with a compressible gas) but, for this initial formulation, p_i is considered to be a constant. Substituting Equations 2.4 and 2.6 into Equation 2.2 and neglecting viscosity and surface tension, the governing equation for the dynamics of the bubble interface is found to be

$$R\ddot{R} + \frac{3}{2}\dot{R}^2 = \frac{p_i - p_\infty}{\rho}. \tag{2.7}$$

The solution is a second-order, linear, non-dissipative ordinary differential equation which, as a result, is harmonic. Nonetheless, it is a good predictor of bubble dynamics through the first collapse.

This equation of motion can be reformulated to account for other phenomena that were not originally considered by Rayleigh, such as the collapse of bubbles in compressible fluids and the collapse of cylindrical cavities. These adjustments will be considered in the following sections.

2.1.2 Spherical Bubbles in Compressible Fluids

The effects of compressibility on spherical cavities were first considered in connection with underwater detonation of explosives. Herring built upon the Rayleigh model by estimating the energy lost due to pressure waves, which he assumed were acoustic [8]. Keller and Kolodner built further upon this assumption [10]. They used the wave equation for the velocity potential, φ, instead of Laplace's equation, as in Section 2.1.1.

The use of the wave equation was continued by Prosperetti and Lezzi, who applied the standard acoustic approximation to develop a family of first-order approximate equations for the motion of a spherical bubble in a compressible fluid [11].

In the compressible case, the fluid is governed by continuity,

$$\frac{\partial \rho}{\partial t} + \nabla \cdot (\rho \vec{u}) = 0, \tag{2.8}$$

and the momentum equation,

$$\frac{\partial \varphi}{\partial t} + \frac{1}{2} u_r^2 + \frac{p}{\rho} = \frac{p_\infty}{\rho}. \tag{2.9}$$

When considering vapor cavities, it is helpful to make a distinction between limiting cases according to the importance of thermal effects, as variations in temperature inside a cavity can strongly influence its vapor pressure. To highlight this, Plesset and Prosperetti consider a vapor bubble that expands to a radius, R_o in a time Δt [18]. The amount of latent energy transferred from the liquid through the vaporization of liquid is given by

$$Q = \frac{4}{3} \pi R_o^3 \rho_v L, \tag{2.10}$$

where ρ_v is the vapor density and L the latent heat of the liquid. This energy comes from a shell of liquid around the bubble, with an approximate thickness based on the thermal diffusivity, D, of the liquid:

$$\delta R = \sqrt{D\Delta t} = \sqrt{\frac{k\Delta t}{\rho_l c_l}}, \tag{2.11}$$

where k is the thermal conductivity of the liquid, ρ_l is the liquid density and c_l is the speed of sound in the liquid. The amount of energy taken from this shell of liquid is then given approximately by

$$\begin{aligned} Q &\simeq 4\pi R_o^2 \delta R \Delta T \rho_l c_l \\ &\simeq 4\pi R_o^2 \Delta T \sqrt{k\Delta t \rho_l c_l}. \end{aligned} \tag{2.12}$$

Combining Equations 2.10 and 2.12, the temperature drop in the surrounding liquid can be computed as

$$\Delta T \simeq \frac{R_o \rho_v L}{\sqrt{k\Delta t \rho_l c_l}} \tag{2.13}$$

For the kinds of cavities to be considered in this work, e.g. a 1 cm cavity in water at 15°C, the above equation yields $\Delta T \sim 2$°C. This, in turn, means a change in the vapor pressure of the liquid of a few percent. This allows the assumption that thermal effects will be unimportant.

Because thermal effects can be neglected, the liquid state can be defined by a single variable. This allows the use of the speed of sound, c, given by

$$c^2 = \frac{dp}{d\rho} \tag{2.14}$$

and enthalpy, h, given by

$$h = \int_{p_\infty}^{p} \frac{dp}{\rho}. \tag{2.15}$$

Using these definitions, as well as the previous definition of velocity potential, Equations 2.8 and 2.9 can be rewritten as

$$\nabla^2 \varphi + \frac{1}{c^2}\left(\frac{\partial h}{\partial t} + u\frac{\partial h}{\partial r}\right) = 0 \tag{2.16}$$

and

$$\frac{\partial \varphi}{\partial t} + \frac{1}{2}u_r^2 + h = 0. \tag{2.17}$$

A modified Tait equation of state is used to provide the relationship between pressure and density in the fluid

$$\frac{p+B}{p_\infty + B} = \left(\frac{\rho}{\rho_\infty}\right)^n. \tag{2.18}$$

Values of $B = 3049$ bars and $n = 7.15$ are known to provide excellent results up to pressures on the order of 1×10^5 bars [11, 19]. From this, sound speed and enthalpy are given by

$$c^2 = \frac{n\,(p+B)}{\rho} \tag{2.19}$$

and

$$h = \frac{c^2 - c_\infty^2}{n-1}. \tag{2.20}$$

Assuming that the pressure does not vary greatly from the ambient, p_∞, Equation 2.15 can be expanded such that

$$\begin{aligned} h &= \int_{p_\infty}^{p} \left(\frac{1}{\rho_\infty} - \frac{p' - p_\infty}{\rho_\infty^2 c_\infty^2} + \dots\right) dp' \\ &= \frac{p-p_\infty}{\rho_\infty}\left(1 - \frac{1}{2}\frac{p-p_\infty}{\rho_\infty c_\infty^2} + \dots\right). \end{aligned} \tag{2.21}$$

In a similar fashion, Equation 2.14 can be expanded around p_∞ so

$$\begin{aligned} c^{-2} &= c_\infty^{-2}\left[1 - \frac{2}{c_\infty}\frac{dc}{dp}\bigg|_\infty (p-p_\infty) + \dots\right] \\ &= c_\infty^{-2}\left(1 - \frac{B}{A}\frac{p-p_\infty}{\rho_\infty c_\infty^2} + \dots\right), \end{aligned} \tag{2.22}$$

where B/A is the standard non-linearity parameter of acoustics, given by

$$\frac{B}{A} = 2\rho c_\infty \frac{dc}{dp}\bigg|_\infty. \tag{2.23}$$

From here, Equations 2.21 and 2.22 can be substituted into the continuity and momentum relationships, Equations 2.16 and 2.17, to yield

$$\nabla^2\varphi + \frac{1}{\rho_\infty c_\infty^2}\left(\frac{\partial p}{\partial t} + u\frac{\partial p}{\partial r}\right)\left[1 - \left(1 + \frac{B}{A}\right)\frac{p-p_\infty}{\rho_\infty c_\infty^2} + \dots\right] = 0, \tag{2.24}$$

and

$$\frac{\partial \varphi}{\partial t} + \frac{1}{2}u^2 + \frac{p - p_\infty}{\rho_\infty}\left[1 - \frac{1}{2}\frac{p - p_\infty}{\rho_\infty c_\infty^2} + \ldots\right] = 0. \tag{2.25}$$

If the sound speed is assumed to be very large ($c_\infty \to \infty$) we recover Equations 2.1 and 2.2, the incompressible formulation of this problem:

$$\nabla^2 \varphi = 0, \tag{2.26}$$

$$\frac{\partial \varphi}{\partial t} + \frac{1}{2}u^2 + \frac{p - p_\infty}{\rho_\infty} = 0. \tag{2.27}$$

This differs from the exact solution, given by Equations 2.21 and 2.22, because it ignores the contribution of two effects: the finite speed of sound in the fluid and the elastic energy stored in fluid by changing its density. Prosperetti and Lezzi argue, however, that, in the vicinity of the bubble ($r \approx R_o$), the consequence of ignoring these effects is negligible. The first is negligible because the time scale of the motion of the bubble interface, t_o, is much longer than propagation times for traveling waves. The second effect can be ignored because the kinetic and pressure energy in the vicinity of the bubble is much larger than the compression energy. As a result, the incompressible solution can be used in the vicinity of the bubble.

Far from the bubble ($r \approx c_\infty t_o$), however, the finite speed of sound needs to be considered. Here, though, the velocity field is so diminished that it can be ignored. This allows Prosperetti and Lezzi to linearize Equations 2.21 and 2.22 as

$$\nabla^2 \varphi + \frac{1}{\rho_\infty c_\infty^2}\frac{\partial \rho}{\partial t} = 0, \tag{2.28}$$

$$\frac{\partial \varphi}{\partial t} + \frac{p - p_\infty}{\rho_\infty} = 0. \tag{2.29}$$

From Equations 2.28 and 2.29, the wave equation for velocity potential follows:

$$\nabla^2 \varphi + \frac{1}{c_\infty^2}\frac{\partial^2 \varphi}{\partial t^2} = 0. \tag{2.30}$$

Using Equations 2.26 through 2.29, Prosperetti and Lezzi constructed a singular perturbation problem which allowed them to arrive at a family of first-order

accurate equations for the radius of a spherical bubble in a compressible fluid, given by

$$\begin{aligned}\left[1-\frac{(\lambda+1)}{c_\infty}\frac{dR}{dt}\right]R\frac{d^2R}{dt^2}+\frac{3}{2}\left[1-\frac{1}{3}\frac{(3\lambda+1)}{c_\infty}\frac{dR}{dt}\right]\left(\frac{dR}{dt}\right)^2 \\ =\left[1+\frac{(1-\lambda)}{c_\infty}\frac{dR}{dt}\right]\left(h_B-\frac{p_v}{\rho_\infty}\right)+\frac{R}{c_\infty}\frac{d}{dt}\left(h_B-\frac{p_v}{\rho_\infty}\right),\end{aligned} \tag{2.31}$$

where λ is an arbitrary parameter smaller than $c_\infty t_o/R_o$, and h_B is a first order approximation of the enthalpy at the bubble given by

$$h_B \simeq \frac{p_i - p_\infty}{\rho_\infty}. \tag{2.32}$$

Setting $\lambda = 1$ recovers the equation of motion derived by Herring [8]. Making $\lambda = 0$ recovers the Keller formulation [10]. As such, Prosperetti and Lezzi coin Equation 2.31 the general Keller-Herring equation.

Their work continued with a companion paper which attempted to increase accuracy to second order [12]. This is achieved by using a more sophisticated matched asymptotic expansion technique. Their resulting formulation has two free parameters and a significant increase in complexity. They conclude, however, that unless the bubble wall Mach number exceeds 0.5 or that ratio of p_∞/p_i exceeds 5000, it does not provide a significant enough increase in accuracy to warrant this increase in complexity. There does not appear to be an analogous form considering the effects of compressibility on cylindrical bubbles.

2.2 Cylindrical Cavities

2.2.1 Experimental Studies

The formation and collapse of cylindrical cavities is relevant primarily in the field of hydroballistics. It has been a topic of interest for more than a century, dating back to Worthington and Cole's late-20th century research studying the effect of surface roughness on the cavities created by free-falling steel spheres [20, 21]. Work in

hydroballistics began in earnest in relation to World War II. Gilbarg and Anderson performed important research, studying the effect of ambient atmospheric pressure on the dynamics of cavities generated by spheres entering water [22]. Albert May performed thorough experiments documenting the water entry of steel spheres, varying several parameters to gage their effect [23, 24, 25].

More recent studies have focused on the water entry of hydrophobic spheres at moderate Froude numbers, on the order of 1 to 100. Duclaux et al. conducted experiments dropping soot-covered glass spheres with radii between 6 mm and 20 mm at velocities between 1.4 and 8.0 m/s [26]. They examined the effect of sphere radius and entry velocity on cavity dynamics, highlighting variations in pinch–off time and depth, in particular. They proceeded to develop a model, starting with the Rayleigh equation, to predict the evolution of the cavity from creation to collapse. This model uses the assumption that the relationship between the cavity radius, R, and the location of the far–field boundary, S, where radial motion is diminished, is $\log(R/S) \sim 1$. They find good agreement between their model and experiments.

Aristoff et al. continue in this vein, studying the cavities created by spheres treated with a superhydrophobic coating [1]. In their first study, steel spheres with radii between 0.6 and 9.0 mm were dropped into water at velocities between 0.1 and 10 m/s. In a parametric study varying Bond ($Bo = \rho g R_o^2/\sigma$) and Weber ($We = \rho v_o^2 R_o/\sigma$) numbers, they recorded four distinct cavity collapse behaviors, as shown in Figure 2.1. At low Weber number ($We \sim 1$), they observed what were termed "quasi–static" cavities, where the sphere was fully wetted and sank, creating a cavity with a volume smaller than that of the sphere itself. At moderately–low Weber number ($We \sim 10$), shallow seal was observed. In this mode, the cavity pinches off near the free surface, at a distance on the order of the capillary length. At higher Weber number ($We \sim 100$), they observed deep seal, where the cavity pinched in two approximately halfway between the sphere and the free surface. At the highest Weber numbers studied ($We \sim 1000$), they observed a fourth behavior:

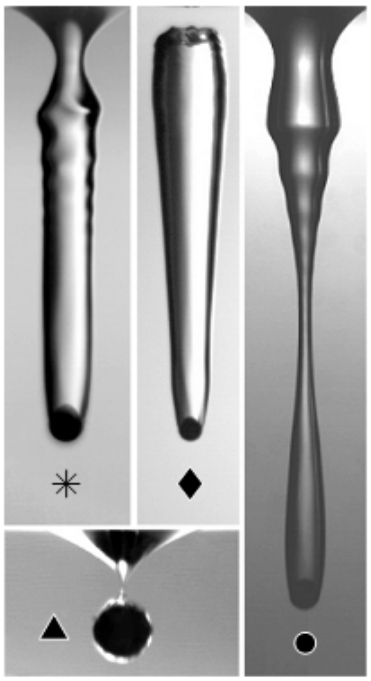

Figure 2.1: Different cavity collapse modes for varying Weber number, $We = \rho v_o^2 R_o/\sigma$: quasi-static, $We \sim 1$ (triangle); shallow seal, $We \sim 10$ (asterisk); deep seal, $We \sim 100$ (circle); and surface seal, $We \sim 1000$ (diamond). Image reproduced from Aristoff and Bush [1].

surface seal. In these cases, the splash at the free surface domes over the opening, sealing the cavity, which continues to expand before detaching from the free surface. They develop a model to predict pinch–off time in the limit of zero Bond number using the Rayleigh equation, like Duclaux et al. [26] before them. They couple this to a high Weber number splash curtain model, finding reasonable agreement with their experiments.

In further work, Aristoff et al. studied the water entry of low–density spheres, to explore the effect of deceleration on the shape of the air cavity [27]. Spheres with densities from 0.2 g/cm^3 and 7.86 g/cm^3 were dropped into water. They found that as sphere density decreases, both pinch-off time and depth decrease. They expand on the model created by Aristoff and Bush [1] to develop analytic expressions for

pinch–off time and depth, finding good agreement with their experimental results.

Truscott et al. studied the cavity dynamics of a sphere shot into water at low Froude number with spin transverse to the axis of penetration [28]. They find that spin highly alters cavity dynamics. As expected, the spin generates lift on the sphere, causing curvature in the trajectory, similar to that of a baseball. At the free surface, when the spin parameter ($\mathcal{S} = r\Omega_o/v_o$) is greater than 0.3, spin creates asymmetry in the splash crown due to the no-slip condition on the surface of the sphere. The no-slip condition also creates a persistent wedge of fluid that is dragged across the cavity by the sphere. They find that spin has minimal effect on cavity pinch-off and collapse compared to Froude number.

Mansoor et al. explored cavity dynamics with a unique modification [29]. By placing a conical "splash–guard" at the free surface of their tank, they are able to study high Froude number water entry cavities in the absence of surface seal. They observe very smooth cavities that are unmarred by re-entrant jets. Their parametric study finds that when surface seal is prevented, pinch-off time is unchanged by Froude number for a given sphere radius. The effect of radial confinement was also explored, by varying the tank geometry from 50 by 50 cm, where wall effects are assumed to be negligible, down to 15 by 15 cm. They find that wall effects delay deep seal. Also, confinement results in ripples along the cavity interface, with wavelength that decreases with tank cross-sectional width. Using particle image velocimetry (PIV), they studied the bulk fluid flow, finding that in cases where wall effects are significant, the radial flow caused by cavity expansion is turned unidirectionally upward by the tank wall before turning radially inward as the cavity collapses.

Shi et al. studied supercavitation in the water entry of high-speed projectiles [30, 31, 32, 33]. In this work, a rifle was used to fire a .22 caliber bullet vertically into an 80 cm deep water tank at 352 m/s ($Fr = 2.2\times10^6$). The resulting cavity was observed via high-speed video captured at 2000 frames per second. In cases where the bullet did not tumble, they observed a slender axisymmetric cavity. At the

free surface, the upward splash generated by impact closes the cavity, which then retracts from the surface. As the cavity retracts, a re-entrant jet forms, disturbing the cavity walls. After a pinching event near the top of the cavity, it collapses, leaving behind a helical wake. They find moderate agreement with theoretical models reported by Savchenko [34] and Lee [3].

2.2.2 Modeling Supercavitating Bodies

Bodies traveling through or entering water at a high enough velocity cause boundary layer separation which produces a vapor cavity that envelops the entire projectile in what is known as supercavitation [34, 35]. Supercavitation allows underwater projectiles to achieve much higher velocity by the virtue of reduced drag. A properly designed supercavitator generates a cavity at its tip, effectively eliminating skin friction. As a result, much has been done in the defense community to study the steady cavity produced by a supercavitating body for use in torpedo design.

There are two categories of supercavitation: vaporous and ventilated. Vaporous supercavitation occurs when a projectile reaches a high enough velocity that water vaporizes at it passes the nose. Ventilated supercavitation is achieved at lower velocities by supplying a gas to the cavity behind the projectile, often at near ambient pressures. In both cases, the cavity shape is a single-valued function of the cavitation number, which is given by

$$Ca = \frac{p_\infty - p_i}{\frac{1}{2}\rho U_\infty^2}, \tag{2.33}$$

where p_i is the pressure in the cavity, either vapor pressure of that of the ventilated gas, and U_∞ is the freestream velocity [36].

Assuming that viscous effects are confined to a thin boundary layer near the surface of the cavitator enables the use of potential flow techniques to predict fluid flow around a supercavitating body, based only on a kinematic condition and a boundary condition. Given that the fluid is incompressible and the flow is

irrotational, the flow is governed by Laplace's equation,

$$\nabla^2\varphi = 0, \tag{2.34}$$

where φ is the velocity potential. As there is no mass transfer across the cavity boundary (nor through the cavitator), the velocity is tangent to the body-cavity surface, requiring that

$$\frac{\partial\varphi}{\partial n} = -\hat{n}\cdot\vec{U}_\infty, \tag{2.35}$$

where $\hat{n}$ is the cavity wall normal vector.

To complete the potential flow model, a cavity termination model is required. One of the earliest and simplest closure methods is the Riabouchinsky termination model [36, 37]. Using this method, the cavity is closed with an "image" of the body placed such that the streamlines close smoothly onto it. Along this mirror image, the kinematic condition is satisfied. This model is often used out of a desire for simplicity rather than physical validity. Riabouchinsky's method is most useful when considering very large cavities as the effect of the presence of an image body is diminished with distance.

At the other end of the spectrum, Joukowski suggested an open-wake model [38]. Using this formulation, the problem is solved by considering the potential flow formulation up to a point on the streamline and then extending the streamlines off to infinity parallel with the surrounding streamlines. Using this model, the wake is much larger than what is observed experimentally. When considered alongside the Riabouchinsky method, which neglects a wake altogether, these two methods bracket what is observed experimentally.

A more physically-accurate yet complex model uses a re-entrant jet to terminate the cavity [36]. In this model, a re-entrant jet is inserted into the model at the closure point where the free streamline nears the axis of symmetry. At this point, it is assumed that the surface is cylindrical and that the velocity has reached a constant value. This implies that the conditions on the jet face are

$$\frac{\partial\varphi}{\partial n} = U_\infty(\sqrt{1+Ca}+1) \tag{2.36}$$

and

$$\frac{\partial \varphi}{\partial s} = 0. \tag{2.37}$$

All of these models provide the final piece required to calculate steady-state cavity shapes for supercavitating projectiles. The kinds of projectiles motivating the current work, however, penetrate a small amount of water before reaching their target. Consequently, they do not produce steady-state wakes. Instead, their wakes are extremely unsteady and short-lived, with typical time scales on the order of 10 ms, meaning, the above work inadequately describes the dynamics of the resulting cavities.

2.2.3 Modeling with the Slender Body Approximation

Those concerned with modeling the growth and collapse of unsteady two-dimensional cavities have primarily taken two approaches which are discussed below: the slender body approximation and an incompressible formulation. The slender body approximation assumes that the fluid is composed of discrete layers of uncoupled fluid that can modeled independently using an energy balance. The incompressible formulation uses a method analogous to that of Rayleigh (Section 2.1.1) to model the collapse of two-dimensional cavities.

The slender body approximation can be used to break a complex water-entry problem into an uncoupled set of one-dimensional cylindrical cavity collapse problems [39]. Lee et al. developed a model that builds on previous work by Birkhoff and Zarantanello [6]. Their work considers a force balance on the water-entry body and an energy balance in the liquid to develop an analytic model to predict the closure time and depth for high-speed water-entry cavities [3].

The trajectory of a projectile penetrating a fluid along the z-axis can be calculated using Newton's second law,

$$m_p a = m_p \frac{dv_p}{dt} = m_p g - \frac{1}{2}\rho v_p^2 C_D A_p \tag{2.38}$$

where m_p is the mass of the projectile, ρ is the density of the liquid, A_p is the projected area of the projectile, and v_p is the projectile velocity. For high-speed water entry, the Froude number, $Fr = v_p^2/gr_p$, is large enough for the effect of gravity in Equation 2.38 to be neglected. Using the above equation, one can calculate the rate of change of kinetic energy of the projectile with respect to depth,

$$\frac{dE_p}{dz} = -\frac{d}{dz}\left(\frac{1}{2}m_p v_p^2\right) = -m_p\frac{dv_p}{dt}. \tag{2.39}$$

Substituting in the results from Newton's second law, Equation 2.38, the amount of energy deposited by the projectile into a thin layer of fluid of thickness dz can be expressed as

$$\frac{dE_p}{dz} = \frac{1}{2}\rho v_p^2 C_D A_p. \tag{2.40}$$

The flow caused by the body entering the fluid is modeled with distributed point sources along the trajectory of the projectile. These sources require a time-delay to account for the motion of the body. Through the use of linearized potential flow equations by Lee, the radial velocity of the fluid is found to be proportional to the source strength, ζ [40],

$$u_r = \frac{2}{r}\zeta\left(z,t\right). \tag{2.41}$$

To calculate the strength of a given point source, the kinetic energy in a ring of fluid extending from the cavity wall at R to some finite distance, S, is computed

$$dE_{l,k} = \pi\rho\int_R^S u_r^2 r dr dz. \tag{2.42}$$

Combining Equations 2.41 and 2.43 and integrating, the kinetic energy in a slice of fluid can be expressed as

$$dE_{l,k} = 4\pi\rho_l\zeta^2\log\frac{S}{R}dz. \tag{2.43}$$

The resulting logarithmic term, $\log\left(S/R\right)$, is set as a constant value. Previous work by Birkhoff and Zarantanello suggested values for S/R in the range of 15 to 30 [6].

To complete the conservation of energy, one needs to account for the potential energy stored in a fluid ring with height dz. This energy is in form of work against a pressure difference in the section and is given by,

$$dE_{l,p} = \Delta P \pi R^2 dz \tag{2.44}$$

where the pressure difference, ΔP, can vary with penetration depth to account for the hydrostatic gradient.

The base assumption of this model is that all of the energy lost by the projectile goes directly into kinetic and potential energy in the fluid. As such, Equation 2.40 can be equated with the sum of Equations 2.43 and 2.44 to derive an equation for the motion of the cavity wall at any given depth. To keep notation concise, the variables $C(z)$ and $D(z)$ are introduced such that

$$[C(z)]^2 = \frac{\rho_l v_p^2 C_D A_p}{2\pi \Delta P} \tag{2.45}$$

and

$$[D(z)]^2 = \frac{\Delta P}{\rho \log(S/R)}. \tag{2.46}$$

Using these variables, the source strength can be expressed as

$$\zeta = \pm \frac{1}{2} D(z) \sqrt{[C(z)]^2 - [R(z)]^2}. \tag{2.47}$$

To complete this formulation, a kinematic boundary condition is applied on the cavity wall, as in Equation 2.3. Combining this boundary condition with the source strength given by linearized potential flow equations in Equation 2.41, the kinematic boundary condition can be expressed as

$$\zeta = \frac{1}{2} R\dot{R}, \tag{2.48}$$

where $\dot{R}$ is the cavity wall velocity. Combining Equations 2.47 and 2.48 the governing equation for the motion of the cavity wall is

$$R\dot{R} = D(z) \sqrt{[C(z)]^2 - [R(z)]^2}. \tag{2.49}$$

Integrating Equation 2.49 with the initial condition of $R(t_r) = r_p$ gives an equation of the cavity radius versus time at a given depth

$$R^2 - r_p^2 = 2D\sqrt{C^2 - r_p^2}\,(t - t_r) - D^2\,(t - t_r)^2 \tag{2.50}$$

where r_p is the projectile radius, and t_r is the time of projectile arrival at a given depth. For simplicity, Lee et al. assume that the projectile radius is small compared to the maximum diameter of the cavity diameter and, as such, neglect r_p.

Lee et al. compare the results of this model to results available in the open literature and to their own numerical work using Autodyn. They find generally good agreement, except in cases where seal of the surface splash modified the cavity pressure, changing the dynamics.

2.2.4 Incompressible Modeling

The Rayleigh-like governing equation for axisymmetric cylindrical cavities presents innate difficulties because the governing equation contains a term that is proportional to logarithm of the radial distance of the far-field boundary from the cavity wall. As a result, the solution diverges in the limit of a large fluid domain.

In studying the growth and detachment of bubbles from needles, Oğuz and Prosperetti developed a Rayleigh-like equation for the collapse of two-dimensional cavities [41]. This formulation was not explored at depth, but was instead used as an asymptote for the behavior of their bubbles. Duclaux et al. use a similar approach to model transient air cavities in water. In their work, they assume that the extent of the radial motion of the fluid is such that $\log S/R \sim 1$ [26]. Lohse et al. use a similar model to predict the dynamics of cavities generated by dropping steel spheres into a fluidic sand bed [14]. In this work, Lohse et al. treated the logarithmic term as being on the order of the experimental system size and dismissed changes caused by varying this term as minimal. Bergmann et al. continued this work, exploring the dynamics of cavities created by disks impacting a free surface [2, 15]. This work focused on modeling the behavior of

the pinching neck in the cavities generated by these plunging disks. As discussed below, they developed a more sophisticated model for the pinch point of two-dimensional vapor cavities that accounts for the asymmetry in the growth and collapse stages.

In a manner similar to that of Rayleigh, a model for the dynamics starts with the Euler equations, this time in cylindrical coordinates, with axial and azimuthal components neglected to give

$$\frac{\partial \varphi}{\partial t} + \frac{1}{2}u_r^2 + \frac{p}{\rho} = f(t). \tag{2.51}$$

Using the kinematic boundary condition (Equation 2.3) and continuity (Equation 2.1) the radial velocity, u_r, and velocity potential, φ, can be represented by

$$u_r = \frac{R\dot{R}}{r}, \tag{2.52}$$

$$\varphi = R\dot{R}\log r. \tag{2.53}$$

Substituting Equations 2.52 and 2.53 into Equation 2.51 and evaluating at the bubble radius, R, and some far-field point, S, where the pressure is p_∞ yields

$$\frac{d(R\dot{R})}{dt}\log\frac{R}{S} + \frac{1}{2}\dot{R}^2\left(1 - \frac{R^2}{S^2}\right) + \frac{p_i - p_\infty}{\rho} = 0, \tag{2.54}$$

which is a governing equation for a cylindrical bubble in an incompressible fluid analogous to the Rayleigh equation for a spherical bubble(Equation 2.7 on page 7).

Unlike the Rayleigh equation, however, this equation includes a dependence on the location of the far-field boundary, which cannot be eliminated by allowing S to become very large. Historically, others have dealt with this term in an approximate manner. As was mentioned previously, Lee et al. followed Birkhoff and Zarantanello's suggestion of a value between 15 and 30 for S/R [3, 6]. In their study of the water entry of decelerating spheres, Aristoff et al. followed the assumption of Duclaux et al. that the radial extent of the fluid motion on the order of the radius of the sphere ($\log(S/R) \sim 1$) [26, 27]. Lohse and Bergmann, as will

be discussed shortly, use experimental results to estimate values for this parameter [2, 14, 15].

Given a Rayleigh-like equation for the cavity radius, Bergmann et al. split the dynamics into three regimes: expansion, contraction, and collapse [2]. Expansion is defined as the time between the arrival of the disk, $t = t_r$, and when the cavity expands from its initial radius, R_o, to its maximum radius, R_{max} at time $t = t_m$. Contraction is the time when the cavity recedes from its maximum toward the initial radius of the cavity, R_o. Collapse is the final stage, when the cavity collapses from R_o at $t = t_x$ to zero at $t = t_c$. By dividing the problem into these three stages, Equation 2.54 can be simplified as appropriate.

Since $\dot{R}(t_m) = 0$, the wall velocity is assumed to be small near the maximum radius, allowing $\dot{R}$ to be neglected in the expansion and contraction stages, yielding

$$\frac{d(R\dot{R})}{dt}\log\frac{R}{S} + \frac{p_i - p_\infty}{\rho} = 0. \tag{2.55}$$

Since $\dot{R}$ is assumed to be small in these stages, $\log(R/S)$ is assumed to change slowly, allowing it to be replaced with the constant $\beta = -\log(R_{max}/S)$. This yields a parabolic solution to Equation 2.55:

$$R^2(z,t) = R_{max}^2 - \frac{p_i - p_\infty}{\rho\beta}(t - t_m)^2. \tag{2.56}$$

In the collapse stage, R approaches zero, causing the logarithm to diverge. In order to maintain validity, its pre-factor must go to zero, meaning

$$\frac{d(R\dot{R})}{dt} = 0. \tag{2.57}$$

Integrating Equation 2.57 twice yields a power law for the radius during this stage:

$$R(z,t) = C\sqrt{t_c - t}, \tag{2.58}$$

where C is a constant that is determined by the continuity of R and $\dot{R}$.

Bergmann et al. argue that different, constant values for β should be used during the expansion and contraction due to fundamental differences in the flow

field caused by the two stages. As a result, β takes on the form of a step function given by

$$\beta = \begin{cases} \beta_e = -\log \frac{R_{max}(t)}{S_e} & t < t_m \\ \beta_c = -\log \frac{R_{max}(t)}{S_c} & t > t_m \end{cases}. \tag{2.59}$$

To solve the equations for all three stages, appropriate initial conditions are needed for each. At the beginning of the expansion and the end of the collapse stage, the radius is $R = R_o$ and the velocity is, $\dot{R}$, proportional to the velocity of the disk, V, such that

$$\dot{R}(t_r) = \alpha_e V, \tag{2.60}$$

$$\dot{R}(t_x) = -\alpha_c V, \tag{2.61}$$

where α_e and α_c are positive quantities.

With the use of the above, the model now has four unknown parameters. They can be used to find the value of the constant in Equation 2.58. Using Equation 2.61 and the fact that $R(t_x) = R_o$ in Equation 2.58 and its derivative, the constant C can be written as

$$C = \sqrt{2VR_o\alpha_c}. \tag{2.62}$$

Furthermore, the continuity of R and $\dot{R}$ at $t = t_m$ permits the four parameters to be related to one another, allowing α_c to be uniquely determined as

$$\alpha_c = \alpha_e \sqrt{\frac{\beta_e}{\beta_c}}. \tag{2.63}$$

This reduces the model to three free parameters, allowing it to be expressed as the following set of equations:

$$R(z,t) = \begin{cases} \sqrt{R_{max}^2 - \frac{p_i - p_\infty}{\rho\beta_e}(t - t_m)^2} & \text{for } t_r < t \leq t_m, \\ \sqrt{R_{max}^2 - \frac{p_i - p_\infty}{\rho\beta_c}(t - t_m)^2} & \text{for } t_m < t \leq t_x, \\ \sqrt{2VR_o\alpha_c(t_c - t)} & \text{for } t_x < t \leq t_c. \end{cases} \tag{2.64}$$

Bergmann et al. performed experiments and numerical simulations of a disk plunging into water at a constant velocity, varying disk velocity and diameter, studying the cavity at its pinch point (where it first closes below the surface). They then used a least-squares fit to determine values of the parameters α and β in Equation 2.64 as a function of Froude number. They found values of β_e increased from 0.4 to 1.2 as Froude number increased from 1 to 500. For the same range, β_c increased from 0.8 to 2.8. They found that the model was capable of accurately reproducing cavity dynamics at the pinch point of the cavity, including the maximum radius and collapse time.

2.3 Conclusions

A review of the literature shows that compressibility effects in the collapse of axisymmetric cylindrical cavities has not been fully considered. Typically, the logarithmic term present in the Rayleigh-like model for a cylindrical cavity is dealt with in an off-hand and approximate manner, particularly in Lee et al. [3], Duclaux et al. [26], and Birkhoff and Zarantanello [6]. Work by Bergmann et al. was the first to use experimental data to determine appropriate values for the logarithmic term for an unbounded fluid for Froude numbers up to 500 [2]. The work in the following chapters seeks to continue this, exploring the effect of compressibility and finite volume in determining cavity dynamics.

Chapter 3

Compressibility Effects in the Collapse of Long Cylindrical Cavities

3.1 Introduction

The problem of a collapsing spherical bubble has received considerable attention. Rayleigh first solved the problem of a collapsing cavity in a large mass of incompressible liquid [9]. This formulation is typically adequate for predicting the initial collapse of a spherical cavity from some initial radius, R_o.

Cylindrical cavities, as described previously, require more careful consideration. A Rayleigh-like equation for cylindrical bubbles is dependent on the non-dimensional parameter, $S^\star$, that is proportional to the radial location of the far-field boundary. Unlike the spherical case, the term containing the fluid boundary does not vanish in the limit of an unbounded domain, leading instead to the prediction of an infinitely long collapse time. To make use of the incompressible cylindrical equations, $S^\star$ needs to be assigned a finite value (often based on comparison to experimental results or an *ad hoc* assumption [3, 6, 42]) or neglected in some other fashion [2].

The assumption of incompressibility neglects any damping effects on the bubble motion resulting from the propagation of energy by acoustic waves, which is required to accurately predict the subsequent rebound and collapse cycles. Compressible effects were later considered for spherical cavities by assuming the velocity potential, φ, satisfies the wave equation [8, 10, 11, 12]. The resulting solution, the Keller-Herring equation, is compared to the Rayleigh-Plesset equation in Figure 3.1. Here it can be seen that the incompressible formulation does a good job

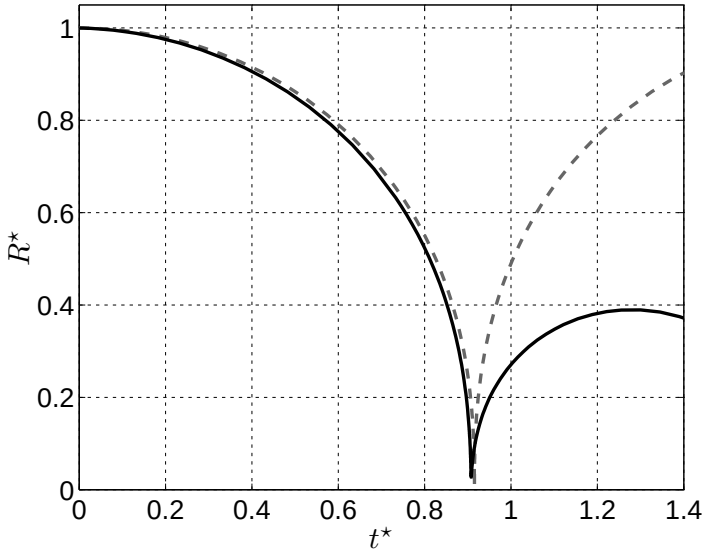

Figure 3.1: Results of numerical integration of the Rayleigh-Plesset equation (dashed line) compared to results of Keller-Herring equation for $\lambda = 0$ (solid line). $R_o/R_{eq} = 5$. Time is scaled by $T_o = R_{eq}\sqrt{\rho/\Delta P}$. $p_\infty = 500$ kPa.

predicting the initial collapse time of the bubble, with an error of 0.1% for the conditions shown.

The work presented in this chapter seeks to demonstrate the effect of compressibility on the collapse of infinitely long cylindrical bubbles. In this case, the compressibility of the ambient fluid, in addition to being a source of damping, sets an effective far-field boundary, $S^\star = S^\star_{crit}$, that dictates the collapse dynamics. The calculation of this effective far-field boundary allows the use of the incompressible solution when predicting the initial collapse behavior in the same fashion as the Rayleigh-Plesset equation.

3.1.1 Compressibility in Spherical Bubbles

Compressibility plays a key role in spherical bubble dynamics beyond the initial collapse cycle. As a bubble oscillates and its pressure varies, pressure waves are

transmitted outward into the fluid. These waves are a source of energy loss, which result in the damped oscillations like those seen in Figure 3.1.

The effects of compressibility were first considered in connection with underwater explosive detonation. Herring built upon the Rayleigh model by estimating the energy lost due to pressure waves which were assumed to be acoustic [8]. Keller and Kolodner built further upon this assumption [10]. They used the wave equation for the velocity potential φ, instead of Laplace's equation. The use of the wave equation was continued by Prosperetti and Lezzi who used the standard acoustic approximation to develop a family of first-order approximate equations for the motion of a bubble in a compressible fluid [11, 12].

Their solution, discussed in-depth in Section 2.1.2, is

$$\left[1-(\lambda+1)\frac{\dot{R}}{c_\infty}\right]R\ddot{R}+\frac{3}{2}\left[1-\frac{1}{3}(3\lambda+1)\frac{\dot{R}}{c_\infty}\right]\dot{R}^2 = \left(h_B-\frac{p_v}{\rho_\infty}\right)+\frac{R}{c_\infty}\frac{d}{dt}\left(h_B-\frac{p_v}{\rho_\infty}\right), \tag{3.1}$$

where λ is an arbitrary parameter smaller than $c_\infty t_o/R_o$ and h_B is a first-order approximation of the enthalpy at the bubble given by

$$h_B \simeq \frac{p_i-p_\infty}{\rho_\infty}. \tag{3.2}$$

Setting $\lambda = 1$ recovers the equation of motion derived by Herring [8]. Making $\lambda = 0$ recovers the Keller formulation [10]. Prosperetti and Lezzi coin Equation 3.1 the general Keller-Herring equation [11].

3.1.2 Modeling Cylindrical Bubbles in an Incompressible Fluid

To model a collapsing bubble in an incompressible fluid, we use the formulation given by Prosperetti [13]. Consider a symmetric shell of incompressible fluid in N-dimensional space between $R(t) \leq r \leq S(t)$. The bubble occupies space between $0 \leq r < R(t)$, where the pressure is uniformly p_i, which can be a function of time.

The far-field is located at $r = S$, where the pressure is initially p_∞. The motion of the bubble interface is given by:

$$\frac{1}{N-2}\left[1-\left(\frac{R}{S}\right)^{N-2}\right]\left[R\ddot{R}+(N-1)\dot{R}^2\right] \\ -\frac{1}{2}\left[1-\left(\frac{R}{S}\right)^{2N-2}\right]\dot{R}^2=\frac{p_i-p_\infty}{\rho}, \tag{3.3}$$

where dots denote time derivatives and ρ is fluid density.

For the special case of $N = 3$, Equation 3.3 yields the motion of a spherical bubble, given by:

$$\left(1-\frac{R}{S}\right)\left[R\ddot{R}+2\dot{R}^2\right]-\frac{1}{2}\left[1-\left(\frac{R}{S}\right)^4\right]\dot{R}^2=\frac{p_i-p_\infty}{\rho}. \tag{3.4}$$

In the limit of a very large fluid domain ($S \to \infty$), this becomes the classical Rayleigh-Plesset equation for the motion of a bubble in an unbounded fluid: [9]

$$R\ddot{R}+\frac{3}{2}\dot{R}^2=\frac{p_i-p_\infty}{\rho}. \tag{3.5}$$

Setting $N = 2 + \epsilon$ and limiting $\epsilon \to 0$, Equation 3.3 yields the equation of motion for an infinitely long cylindrical bubble:

$$-\log\frac{R}{S}\left[R\ddot{R}+\dot{R}^2\right]-\frac{1}{2}\left[1-\left(\frac{R}{S}\right)^2\right]\dot{R}^2=\frac{p_i-p_\infty}{\rho}. \tag{3.6}$$

In this case, the logarithmic term in S diverges for the limiting case of $S \to \infty$. As a result, there is no unique limiting solution for the collapse of a cylindrical bubble in an unbounded fluid.

To demonstrate the ramifications of the logarithmic term in S, the ODEs in Equations 3.4 and 3.6 were solved numerically for $R(t)$ using a range of values for $S^\star = S/R_o$. The cavity contents were modeled as a polytropic gas with a ratio of specific heats, $\gamma = 1.4$. The collapse time for each case is taken as the time when the bubble radius reaches a minimum ($\dot{R} = 0$) and the cavity begins to expand. These results are shown in Figure 3.2. The resulting collapse times

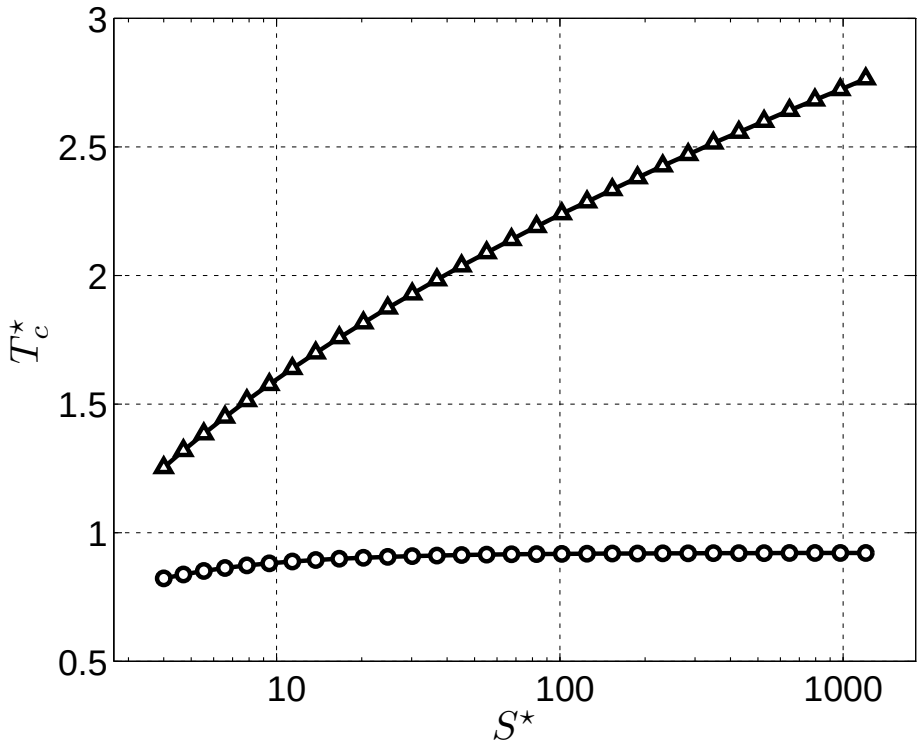

Figure 3.2: Collapse time versus fluid domain size, $S^\star$ for cylindrical (triangles) and spherical (circles) cavities. Collapse time is scaled by $R_o\sqrt{\rho/\Delta P}$. S is scaled by the initial cavity radius, R_o.

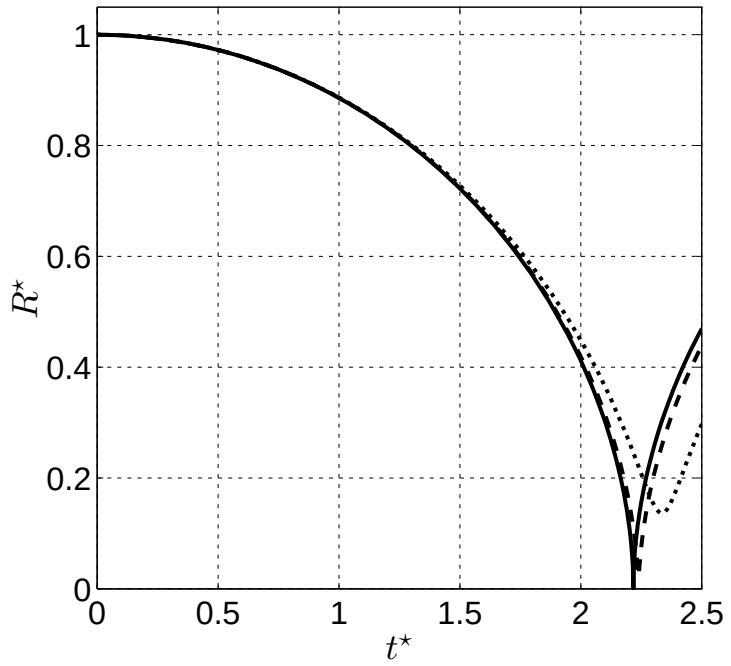

Figure 3.3: Cavity radius history for $S^\star$=100 for initial pressure ratio, p_∞/p_o, of 10 (dotted), 25 (dashed), and 1000 (solid). Cavity contents are modeled as a polytropic gas with a ratio of specific heats, $\gamma = 1.4$.

show very little variation for the spherical case (Equation 3.4), increasing from 0.880 to 0.915, quickly approaching within 1% of the asymptotic value given by the Rayleigh-Plesset equation by $S^\star \approx 30$. The values for the cylindrical case (Equation 3.6), on the other hand, show a monotonic trend, increasing from 1.1 to 2.8 in the nearly three decades shown. If $S^\star$ were allowed to grow to infinity, the collapse time, $T_c^\star$ would similarly become infinite.

The collapse behavior is also dependent on the initial pressure in the cavity. Figure 3.3 shows cavity collapse for three cases with varying initial pressure ratio, p_o/p_∞, where p_o is the initial value of p_i. For low initial pressure ratios, the bubble wall is slowed by the higher cavity pressure, leading to a more gradual collapse to a larger minimum radius at a later time. Above values of approximately 200,

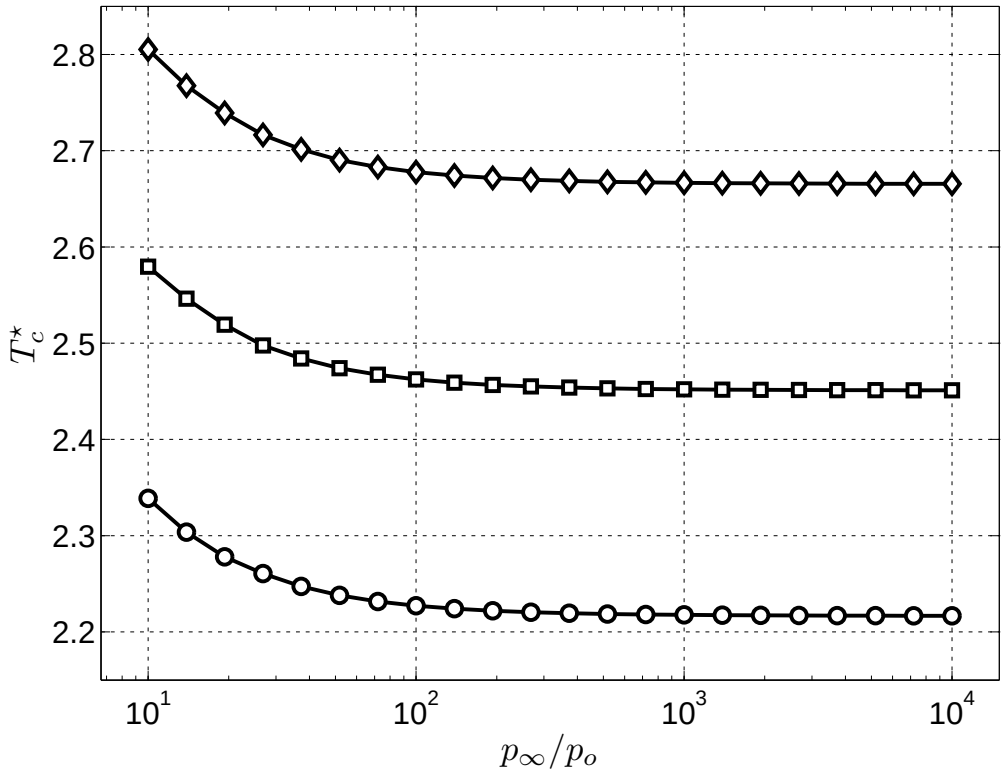

Figure 3.4: Collapse time versus initial pressure ratio, p_∞/p_o, for $S^\star$=100 (circles), $S^\star$=300 (squares), and $S^\star$=900 (diamonds). Cavity contents are modeled as a polytropic gas with a ratio of specific heats, $\gamma = 1.4$.

collapse time is insensitive to initial pressure ratio, as demonstrated in Figure 3.4. For the remainder of the work presented in this chapter, the initial pressure ratio is fixed at 1000 in order to minimize the effect of initial cavity pressure.

3.1.3 Treating the Logarithmic Singularity

The logarithmic singularity in Equation 3.6 has been dealt with in multiple ways. The most elementary is to assume a constant value of $S^\star$ for the entire time of interest. This is demonstrated with some success by Lee et al. [3] who, following the precedent of Birkhoff [6] and Lundstrom [42], assigned $S^\star$ a value in the range of 15 to 30 when developing a model to predict cavity profiles for subsonic projectiles entering water.

Other methods correlate a physical parameter with the value of $S^\star$. Lohse et al. use a Rayleigh-type model, like Equation 3.6, to predict the dynamics of cavities generated by dropping steel spheres into a fluidic sand bed [14]. In this work, Lohse et al. treated the logarithmic term as being on the order of the experimental system size and dismissed changes caused by varying this term as minimal.

Bergmann et al. continued this work, exploring the dynamics of the pinch point of cavities created by disks impacting a free surface [2]. They developed a more sophisticated model for axisymmetric cylindrical vapor cavities that accounts for the asymmetry in the growth and collapse stages by changing how the logarithmic dependence on S is handled. The result of their work, discussed at greater depth in Section 2.2.4, is a set of equations that models the cavity expansion and collapse in three stages:

$$R(z,t) = \begin{cases} \sqrt{R_{max}^2 - \frac{p_i - p_\infty}{\rho \beta_e}(t - t_m)^2} & t_r < t \leq t_m, \\ \sqrt{R_{max}^2 - \frac{p_i - p_\infty}{\rho \beta_c}(t - t_m)^2} & t_m < t \leq t_x, \\ \sqrt{2V R_o \alpha_c (t_c - t)} & t_x < t \leq t_c. \end{cases} \tag{3.7}$$

3.2 The Gemini Euler Solver

Despite the logarithmic singularity in the governing equation, a cylindrical cavity in an unbounded fluid will, indeed, collapse in a finite time. Previous work has sought to deal with the diverging logarithmic term by approximation, as described in Section 3.1.3. The current work seeks an alternate approach, exploring the limiting effect of liquid compressibility on collapse dynamics. This problem in cylindrical coordinates, however, does not readily lend itself to the asymptotic expansions used to achieve the Keller-Herring equation in Section 2.1.2. In place of an analytic solution, the Gemini fluid solver is used to numerically integrate the Euler equations.

Gemini is a compressible, multi-material Euler equation solver developed by the Naval Surface Warfare Center, Indian Head Explosive Ordnance Disposal Technology Division (NSWC IHEODTD) for use simulating underwater explosions. It is part of the larger DYSMAS hydrocode suite, which includes a Lagrangian structural code. These two codes can be two-way coupled, allowing for accurate prediction of damage caused by underwater explosions. The focus of the current work, however, only requires the use of the Euler solver, Gemini.

Gemini is designed primarily for use simulating underwater explosions. As a result, there is a strong focus on accurately capturing phenomena common in explosions, in particular shocks and bubble collapse and jetting.

3.2.1 Scheme

Gemini solves the Euler equations using a time split higher-order Godunov method [43]. The solution is advanced by performing one-dimensional sweeps in each coordinate direction, solving the one-dimensional Euler equations:

$$\frac{\partial U}{\partial t} + \frac{\partial F}{\partial r} = \Phi, \tag{3.8}$$

in which

$$U = r^n \begin{bmatrix} \rho \\ \rho u \\ \rho E \\ \rho \xi \end{bmatrix}, \; F = r^n \begin{bmatrix} \rho u \\ \rho u^2 + p \\ \rho u E + p u \\ \rho u \xi \end{bmatrix}, \; \Phi = \begin{bmatrix} 0 \\ n r^{n-1} p + \rho g \\ \rho g u \\ 0 \end{bmatrix}, \tag{3.9}$$

where $n = 0, 1, 2$ for spherical, cylindrical, and Cartesian coordinate systems, respectively, and ξ is any convected scalar variable, including velocity components perpendicular to the sweep direction (e.g. v and w for the x-sweep in three dimensions).

The standard Godunov method assumes the solution is piecewise constant over grid cells at each time step [44]. To advance the solution in time, a Riemann shock tube problem is solved between neighboring cells. This avoids the use of series approximations for derivatives, which can cause undesirable oscillations in the vicinity of shocks. However, since the piecewise approximation has errors of the order Δx, this scheme achieves only first-order spatial accuracy.

To increase accuracy, Gemini employs a Monotone Upstream-centered Scheme for Conservation Laws (MUSCL) based on work by van Leer and Colella [45, 46]. This scheme allows Gemini to have second-order spatial accuracy. The solution is calculated using a predictor-corrector method. In the predictor step, the cell edge properties are calculated at the half time step using the method of characteristics. The predictor method employs numerical derivatives whose magnitudes are limited near shocks. This prevents the slopes of fluid properties from becoming unrealistically high in these areas. The limiting process drives the derivatives to zero in these regions, returning instead to the standard first-order Godunov method.

The result of the predictor step is two sets of conditions at each cell edge: one from the cell adjacent to the left and another from the cell to the right. These conditions serve as the initial conditions for a Riemann shock tube problem. For efficiency, Gemini uses approximate Riemann solutions between adjacent cells in place of the full problem. The solution of this problem is used to compute fluxes

at each cell edge. Using these fluxes, the solution is advanced.

In addition, a Lagrange plus re-map method, similar to that described by van Leer [45], is used to handle cells with two or more materials, known as mixed cells. Cell edges adjacent to mixed cells are convected with the edge velocities, allowing fluxes to be computed. From here, the contents of each mixed cell are broken into material-specific components. The solution is then mapped back on to the original mesh with materials re-distributed by the Simple Line Interface Computation (SLIC) algorithm [47]. This assures that the appropriate materials are convected at mixed cell interfaces. Gemini's Lagrange plus re-map method has first-order spatial accuracy.

3.2.2 Equations of State

Gemini uses a Tillotson equation of state to represent the water [48]. This formulation was first developed in connection with hypervelocity impacts on metal. It is accurate across large ranges of pressure. For a given density and energy, e, pressure is given by

$$p = p_o + (\gamma - 1)\rho(e - e_o) + A\mu + B\mu^2 + C\mu^3 \tag{3.10}$$

where γ is the ratio of specific heats; $\mu = \rho/\rho_o - 1$; A, B, and C are constants; and p_o, ρ_o, and e_o define a known reference state.

The air in the problem is represented with a gamma law equation of state. This assumes an adiabatic process, as is common [10, 49]. For a given energy and density, pressure is given by

$$p = \rho(\gamma - 1)e. \tag{3.11}$$

3.2.3 Validating with the General Keller-Herring Equation

To demonstrate accuracy, Gemini simulations of spherical bubbles were performed for varying ambient pressures and compared to the results predicted by the Keller-Herring equation (Equation 3.1) for $\lambda = 0$ and $\lambda = 1$. For all cases, the equilibrium

radius, R_{eq} (the radius at which the internal pressure of the bubble equals the ambient pressure), was held constant. It can be expressed as

$$R_{eq} = R_o \left(\frac{p_o}{p_\infty} \right)^{1/N\gamma} \tag{3.12}$$

where γ is the ratio of specific heats for the cavity contents and N is the number of dimensions; $N = 3$ for spherical and $N = 2$ for cylindrical cavities. For the spherical cases used in this validation, $R^\star_{eq} = R_{eq}/R_o = 0.2$. In order to obtain a grid-independent solution, grid spacing in the vicinity of the cavity is $\Delta r^\star \simeq 0.002$.

As shown in Figure 3.5a, the agreement between Gemini and the Keller-Herring solution is good through two collapse cycles for $p_\infty = 30$ kPa. Prior to the initial collapse at $t^\star = 0.914$, the root mean square (RMS) deviation of the bubble size (Figure 3.5b) is 0.06 percent for $\lambda = 0$ and 0.09 percent for $\lambda = 1$. After the initial collapse, the agreement is not as good, with a RMS deviation starting at 1 percent and increasing toward 10 percent by the second collapse. It should be noted here that this deviation is largely due to a shift in the period of the bubble oscillation.

Figure 3.5d shows results for $p_\infty = 3000$ kPa. Prior to collapse at $t^\star = 0.902$, the agreement is like that for $p_\infty = 30$ kPa, with RMS differences of 0.1 and 0.08 percent for $\lambda = 0$ and $\lambda = 1$, respectively. During the rebound and subsequent collapse, the differences are approaching 50 percent, again, primarily due to a phase offset caused by a difference in maximum radius during the rebound.

The behavior of the difference is due to the first-order nature of the Keller-Herring equation. While the bubble wall Mach number (Figs. 3.5c,f) is small ($Ma < 0.01$), the error is negligible and keeps a constant maximum value. As Ma increases, however, the error in the approximation will similarly increase, as demonstrated in Figures 3.5e,f. The Mach number reaches its maximum value at the initial collapse. For $p_\infty = 30$ kPa, the maximum is 0.37. For $p_\infty = 3000$ kPa, this maximum is much larger, $Ma \sim 1$. In turn, the error in the Keller-Herring solution for the second case is much larger. Gemini, which is a second-order solver, is expected to have greater accuracy in these high Mach number situations.

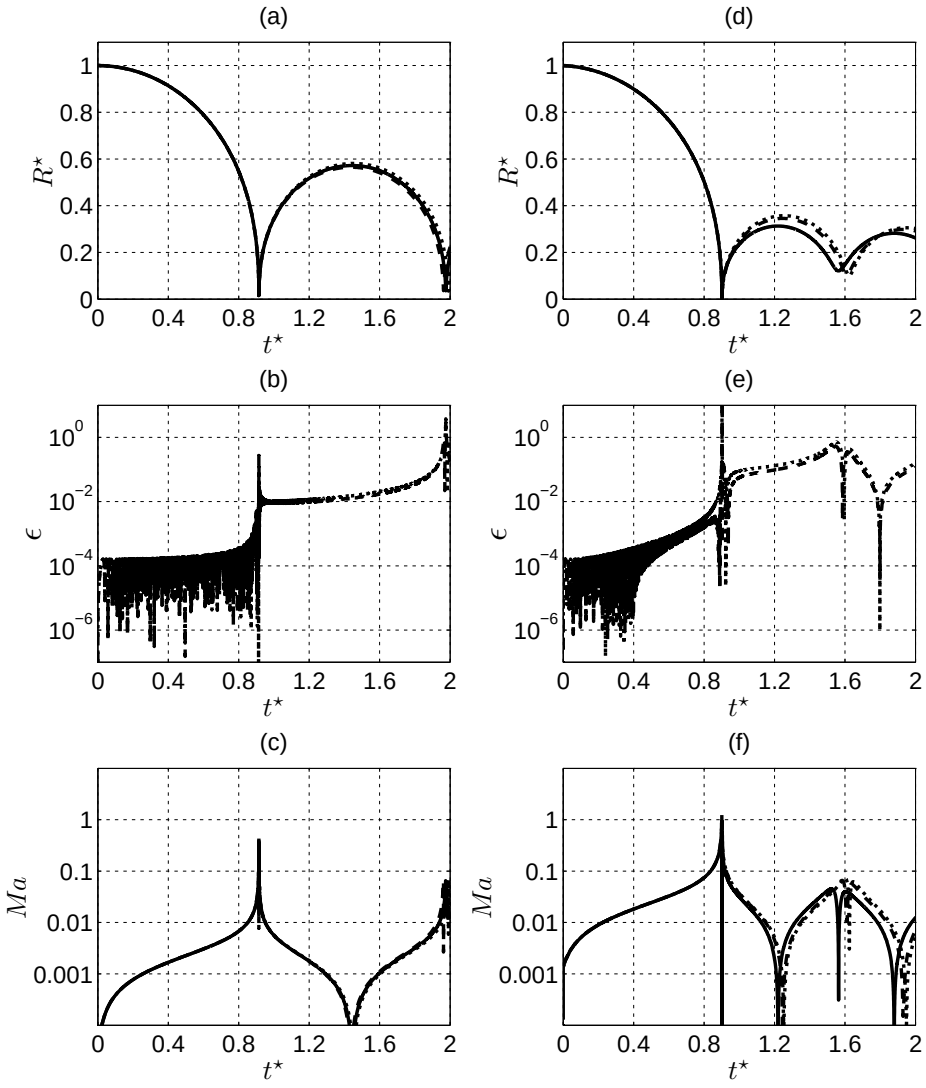

Figure 3.5: Gemini results (solid line) compared to results of Keller-Herring equation for $\lambda = 0$ (dotted line) and $\lambda = 1$ (dashed line). $R^\star_{eq} = 0.2$. Time is scaled by $T^\star_c = R_o\sqrt{\rho/\Delta P}$. $p_\infty = 30$ kPa: (a) Cavity radius versus time. (b) Error in Keller-Herring predicted radius, as compared to Gemini results. (c) Bubble wall Mach number in liquid versus time. Subfigures (d-f) show the same quantities for $p_\infty = 3000$ kPa.

3.3 Results and Discussion

3.3.1 Comparison to Incompressible Model

Figure 3.6 shows the collapse time for a cylindrical bubble as a function of $S^\star$ for varying ambient pressures compared to the results from the incompressible formulation (Equation 3.6) with the same initial conditions.

The results from the cylindrical incompressible formulation are all self-similar, collapsing onto one curve. For clarity, only one such curve is shown. For low values of $S^\star$, the results for all values of p_∞ collapse on to this curve. However, as $S^\star$ increases, each of the curves calculated by Gemini plateaus, reaching a constant collapse time, $T^\star_{c,crit}$, independent of $S^\star$. The critical value of $S^\star$ at which these plateaus occur decreases with increasing p_∞.

The critical fluid domain size, S_{crit}, corresponds to half the distance an acoustic wave would travel before the collapse time,

$$S_{crit} = \frac{1}{2} c T_{c,crit}, \tag{3.13}$$

where $T_{c,crit}$ is a function of ΔP, as demonstrated in Figure 3.6. Non-dimensionalizing by $T_o = R_o\sqrt{\rho/\Delta P}$ yields

$$S^\star_{crit} = \frac{1}{2}\frac{T^\star_{c,crit}}{\sqrt{\Delta P^\star}}. \tag{3.14}$$

where ρ and c are fluid density and sound speed, S_{crit} is non-dimensionalized by R_o, and the driving pressure difference has been scaled as $\Delta P^\star = \Delta P/\rho c^2$.

3.3.2 Limited Collapse Behavior

Figures 3.7a and 3.7b show space-time plots of the pressure field predicted by Gemini for $S^\star = 31$ and $S^\star = 401$, respectively for $p_\infty = 95$ kPa and $p_o = 0.095$ kPa. Horizontal lines in these plots are at a constant spatial location while vertical lines are for a fixed time. For this value of p_∞, the critical fluid domain size is $S^\star_{crit} = 171$. This means that the $S^\star = 31$ case, as shown in Figure 3.7a, is not

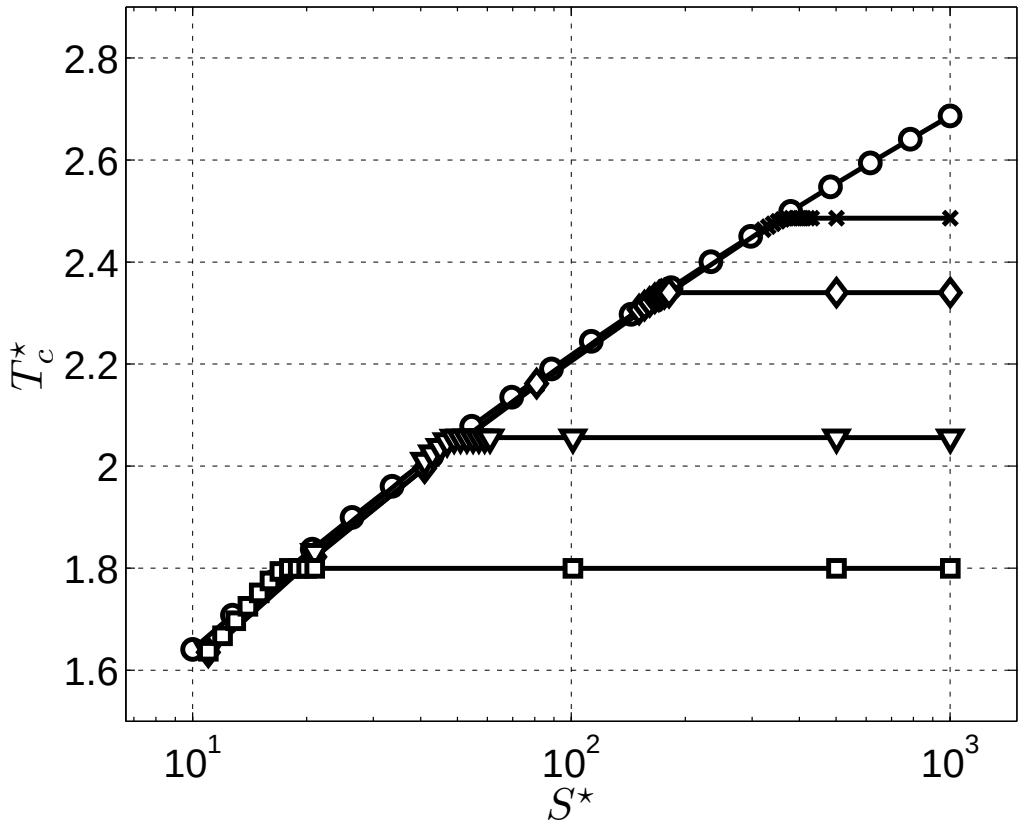

Figure 3.6: Cylindrical cavity collapse time, $T_c^\star$ versus domain size, $S^\star$ for various values of p_∞. The incompressible solution is self-similar, so one representative curve is shown (circles). All cases have a constant initial pressure ratio, $p_\infty/p_o = 1000$. Ambient pressures are 25 kPa (crosses), 95 kPa (diamonds), 1000 kPa (triangles), and 6400 kPa (squares).

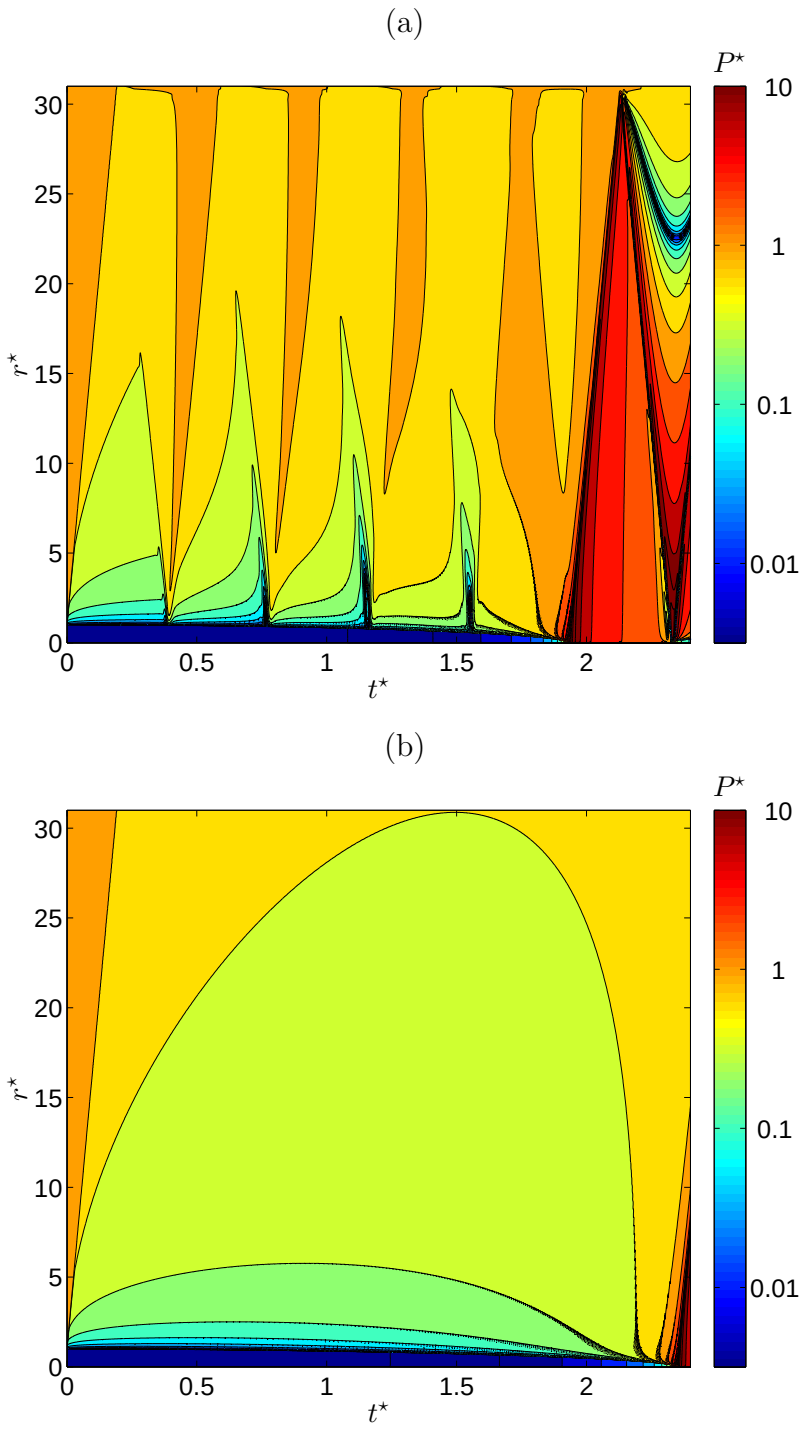

Figure 3.7: Pressure field in the vicinity of collapsing cylindrical cavities. $p_\infty = 95$ kPa. (a) $S^\star = 31$. (b) $S^\star = 401$.

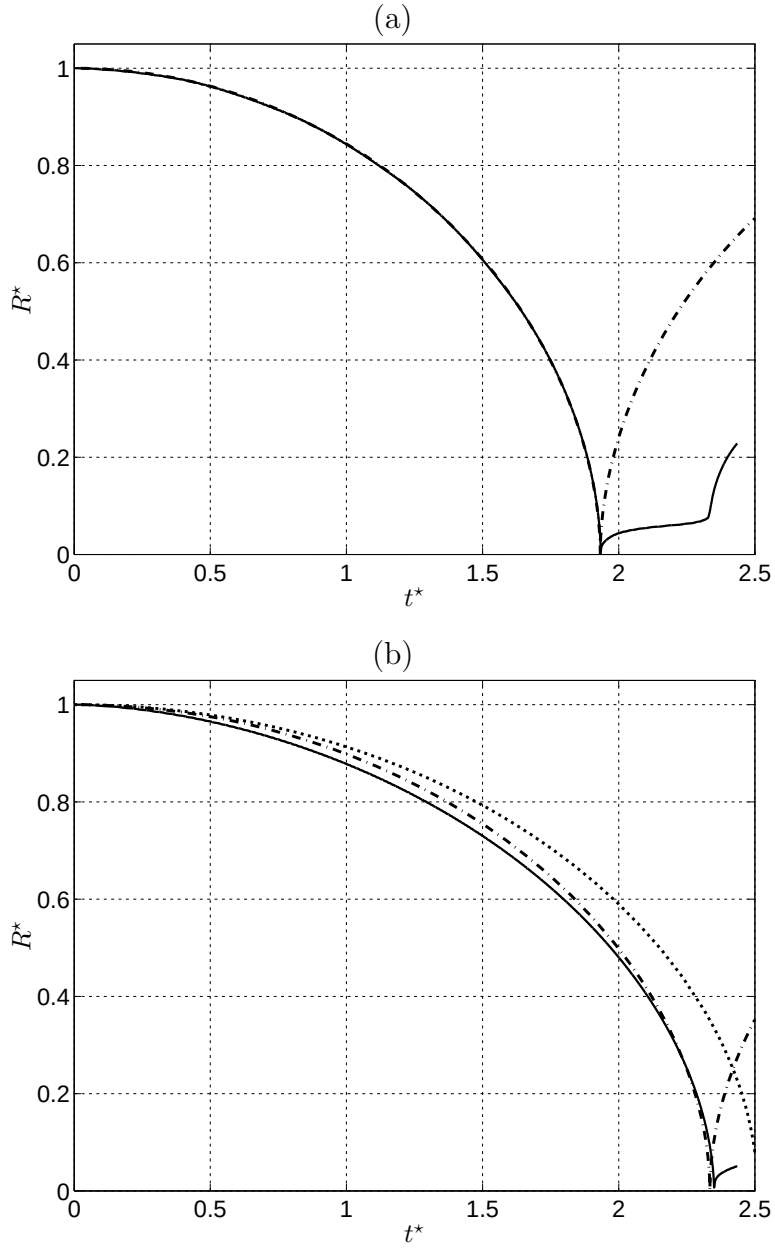

Figure 3.8: Gemini solutions for cylindrical bubble with $p_\infty = 95$ kPa, $p_o = 0.095$ kPa compared to results from the incompressible formulation. (a) $S^\star = 31$ for Gemini (solid line) and incompressible case (dashed line) (b) Gemini (solid line) with $S^\star = 401$ and incompressible solutions with $S^\star = S^\star_{crit} = 171$ (dashed line) and $S^\star = 401$ (dotted line)

in the compressibility-limited regime. As a result, information, in the from of an acoustic wave, has time to travel out to the fluid boundary at $S^\star$ and back to the bubble wall before collapse. This wave can be seen in Figure 3.7a as a series of triangular shapes, leaving the bubble surface at $t^\star = 0$ and returning at intervals of $t^\star = 0.4$. The returning wave modifies the collapse behavior, causing a shorter collapse time. Figure 3.8a shows the bubble radius as a function of time for this case with the results of Equation 3.6 for the same value of $S^\star$. The results of the two match well during the collapse phase. They deviate on the following rebound cycle due energy lost to fluid compressibility effects caused by the high pressure at collapse.

As a comparison, Figure 3.7b shows results for the same ambient pressure for $S^\star = 401$, which is greater than $S^\star_{crit}$. In this case, the acoustic wave does not have time to propagate to the fluid boundary and back. As a result, the bubble effectively never "knows" about the boundary, and collapses as if it were in an infinite medium. Figure 3.8b shows the bubble radius as a function of time for this case as compared to incompressible results for $S^\star = 171$ and $S^\star = S^\star_{crit}$. In this case, the incompressible results with equivalent $S^\star$ over-predict the collapse time, while the case at $S^\star_{crit}$ matches the behavior of the compressible bubble well.

3.3.3 Energy Balance

The differences between the incompressible and compressible formulations is further illuminated by considering an energy balance on the fluid volume. This allows insight into where the energy is being redistributed to make the collapse behavior different.

Considering, in the manner of Prosperetti [50], the fluid in the volume, $\mathcal{V}$, bounded by the cavity surface, $\mathcal{S}_R$, and a large concentric surface far away, $\mathcal{S}_\infty$, conservation of energy demands that

$$\frac{d}{dt}\frac{1}{2}\int_{\mathcal{V}} \rho\vec{u}\cdot\vec{u}d\mathcal{V} = \int_{\mathcal{V}} p\nabla\cdot\vec{u}d\mathcal{V} - \int_{\mathcal{S}_R+\mathcal{S}_\infty} p\vec{u}\cdot\hat{n}d\mathcal{S} \tag{3.15}$$

where $\vec{u}$ and p are the local velocity and pressure fields, $\hat{n}$ is the outward normal of the fluid volume, and viscosity has been neglected. The term on the left hand side represents the time rate of change of the kinetic energy in the fluid. The terms on the right hand side are the rate of work due to volume change and the rate of work on the surfaces, respectively.

In an incompressible fluid, continuity requires that the divergence of the velocity field be exactly zero, so the volume work term in Equation 3.15 is exactly zero. Using this same condition, the velocity field is $u = R\dot{R}/r$. This allows the left hand side of Equation 3.15 to be expressed as

$$\frac{d}{dt}\frac{1}{2}\int_{\mathcal{V}} \rho\vec{u}\cdot\vec{u}d\mathcal{V} = 2\rho\pi R\dot{R}\left[\log\frac{R}{S}\left(R\ddot{R}+\dot{R}^2\right)+\frac{\dot{R}^2}{2}\left(1-\frac{R^2}{S^2}\right)\right], \tag{3.16}$$

where S is the location of the far-field surface, $\mathcal{S}_\infty$.

The pressure field in the liquid can be determined using Bernoulli's equation,

$$\frac{\partial\varphi}{\partial t}+\frac{1}{2}u^2+\frac{p}{\rho}=f(t) \tag{3.17}$$

where f is a function of time only and φ is the velocity potential, given by

$$\varphi = \int u dr = R\dot{R}\log r. \tag{3.18}$$

Using Equations 3.6, 3.17 and 3.18, the pressure field is found to be

$$\frac{p-p_i}{\rho} = \left(R\ddot{R}+\dot{R}^2\right)\log\frac{R}{r}+\frac{1}{2}\dot{R}^2\left(1-\frac{R^2}{r^2}\right). \tag{3.19}$$

This allows the remaining term on the right hand side of Equation 3.15 to be re-written as

$$\begin{aligned}\int_{\mathcal{S}_R+\mathcal{S}_\infty} p\vec{u}\cdot\hat{n}dS &= 2\pi R\dot{R}\left(p(S)-p_i\right)\\ &= 2\pi\rho R\dot{R}\left[\log\frac{R}{S}\left(R\ddot{R}+\dot{R}^2\right)+\frac{\dot{R}^2}{2}\left(1-\frac{R^2}{S^2}\right)\right]\end{aligned} \tag{3.20}$$

Substituting Equations 3.16 and 3.20 into Equation 3.15 shows that energy is conserved.

Similar quantities can be calculated using the pressure and velocity fields given by Gemini. Figures 3.9, 3.10, and 3.11 show the results of this energy balance for three cases where $p_\infty = 95$ kPa and $p_o = 0.095$ kPa. Time has been non-dimensionalized by

$$t_o = R_o \sqrt{\frac{\rho}{\Delta P}}, \tag{3.21}$$

where ρ is fluid density. Rates of work have been scaled by $\dot{W}_o = E_o/t_o$, where E_o is the potential energy initially stored in the bubble:

$$E_o = \pi R_o^2 \Delta P. \tag{3.22}$$

All three figures are logarithmic in the ordinate, with the upper and lower portions showing positive and negative quantities, respectively. Magnitudes of less than 1×10^{-4} have been truncated.

Figure 3.9 shows the results for $S^\star = 31$, a case whose behavior is affected by the size of the fluid domain. For comparison, the analytic incompressible solutions for the kinetic energy and surface work terms are shown. In early time ($t^\star < 0.2$), the change in kinetic energy in the fluid is balanced almost entirely by the volume change work, as the motion of the bubble wall causes an expansion wave in the fluid. The contribution to the surface work term at the inner surface ($r = R$) is non-zero during this time. However, the relatively small area and velocity there yield a much lower net rate of work than the volume change work due to the expansion wave.

At $t^\star = 0.2$, the expansion wave reaches the outer surface at $r^\star = S^\star$ and reflects, becoming a compression wave. This causes a change in sign in the volume work term. The reflection gives the outer boundary a finite negative velocity. The surface work term is now dominated by this contribution, due primarily to its relatively large area, causing a change in sign. At this point, the value of the surface work term matches the analytic incompressible solution well. The rate of work done at the outer surface is an order of magnitude larger than the volume work term, nearly balancing the kinetic energy term in its entirety. When

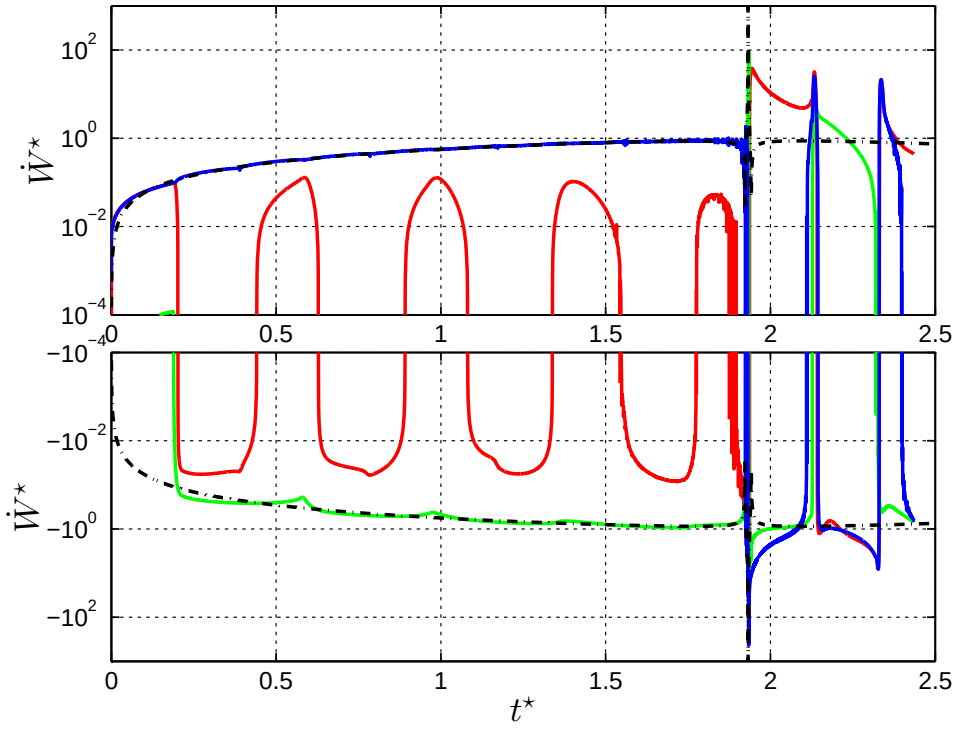

Figure 3.9: Energy balance for collapsing cylindrical cavity in a compressible fluid for $S^\star = 31$, $p_\infty = 95$ kPa, $p_o = 0.095$ kPa showing the time rate of change of kinetic energy in the fluid (blue), rate of work done at inner ($r = R$) and outer ($r = S$) surfaces (green), and rate of volume change work in the fluid (red). The analytic solution for an incompressible fluid (black) is shown for comparison. Time is normalized by $t_o = R_o\sqrt{\rho/\Delta P}$. Energy rates are normalized by $\dot{W}_o = E_o/t_o$ where E_o is the energy per unit length initially stored in the bubble, $E_o = \pi R_o^2 \Delta P$.

the compression wave reaches the cavity at $r = R$, it reflects again, once more becoming an expansion wave. For $S^\star = 31$, this cycle repeats 4 times before the collapse at $t^\star = 1.85$.

These results agree largely with the analytic incompressible formulation once the expansion wave reaches the outer boundary, starting its motion. One interpretation of this is that following that point in time ($t^\star > 0.2$), the collapsing behavior of the cavity has propagated through the entire domain, influencing the maximum amount of fluid. The entire volume is then in motion and the fluid begins to act in

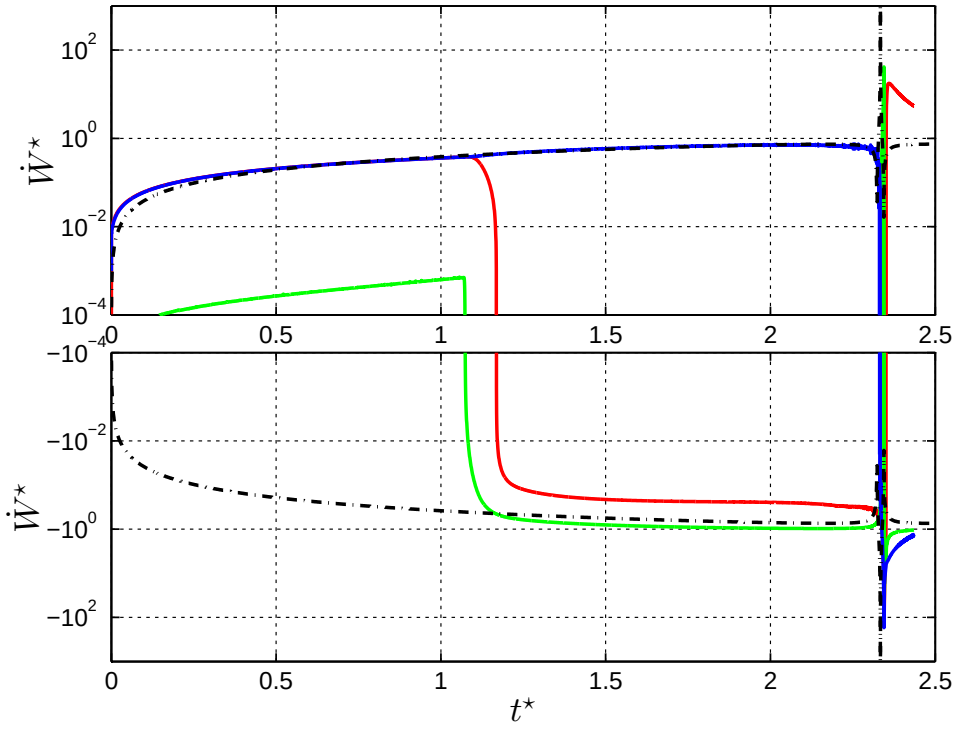

Figure 3.10: Energy balance for collapsing cylindrical cavity in a compressible fluid for $S^\star = 171$, $p_\infty = 95$ kPa, $p_o = 0.095$ kPa showing the time rate of change of kinetic energy in the fluid (blue), rate of work done at inner ($r = R$) and outer ($r = S$) surfaces (green), and rate of volume change work in the fluid (red). The analytic solution for an incompressible fluid with $S^\star = S^\star_{crit} = 171$ (black) is shown for comparison. Time is normalized by $t_o = R_o\sqrt{\rho/\Delta P}$. Energy rates are normalized by $\dot{W}_o = E_o/t_o$ where E_o is the energy per unit length initially stored in the bubble, $E_o = \pi R_o^2 \Delta P$.

a way that approaches an incompressible volume of fluid. The differences between the analytic incompressible solution and the results given by Gemini are relatively small. The velocity fields agree well, as do the pressures with the exception of the weak shock traveling back and forth through the fluid. As a result, the outcome of the energy balance for the Gemini results is largely the same as predicted by the analytic incompressible solution, except for the volume change work done by the shock.

Figures 3.10 and 3.11 show the results of the energy balance for two cases that

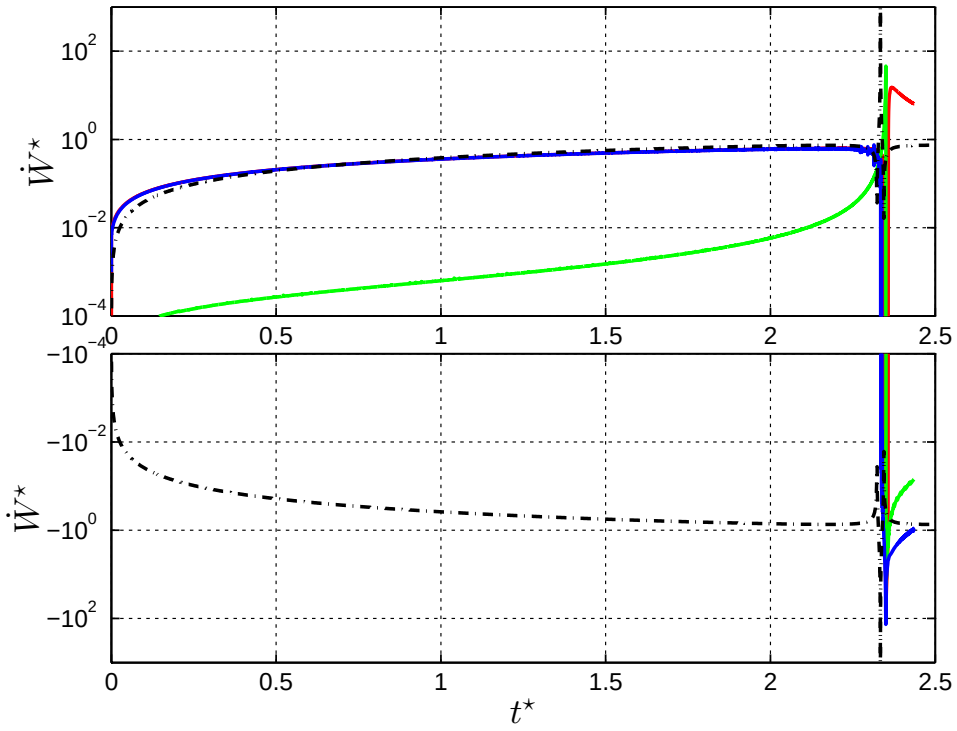

Figure 3.11: Energy balance for collapsing cylindrical cavity in a compressible fluid for $S^\star = 401$, $p_\infty = 95$ kPa, $p_o = 0.095$ kPa showing the time rate of change of kinetic energy in the fluid (blue), rate of work done at inner ($r = R$) and outer ($r = S$) surfaces (green), and rate of volume change work in the fluid (red). The analytic solution for an incompressible fluid (black) is shown for comparison. Time is normalized by $t_o = R_o\sqrt{\rho/\Delta P}$. Energy rates are normalized by $\dot{W}_o = E_o/t_o$ where E_o is the energy per unit length initially stored in the bubble, $E_o = \pi R_o^2 \Delta P$.

yield the same cavity radius history. Figure 3.10 shows results for $S^\star = 171$. This is near the critical value of $S^\star$ for $p_\infty = 95$ kPa, meaning the expansion wave has just enough time to reach the outer boundary and reflect, returning to the cavity wall at the collapse time. These results are largely similar to those for $S^\star = 31$ but on a larger time scale. Here, the surface work term, initially dominated by the work done by the moving boundary at $r = R$, has time to become an order of magnitude larger, reaching 1×10^{-3} before the expansion wave is incident upon the outer boundary, causing motion there. From this point, as before, the expansion wave becomes a compression wave traveling back toward $r = R$. The motion of the fluid is balanced by work done at the outer surface as it moves inward. The volume change done by the compression wave remains significant, $\sim$10% of the magnitude of the surface work term. As a result, the magnitude of the rate of work is slightly higher than predicted by the incompressible analytic solution, implying a higher than predicted inward velocity at the far-field boundary.

Figure 3.11 shows energy balance results for $S^\star = 401$. Results of the incompressible form are shown for the critical value, $S^\star_{crit} = 171$. In this case, the expansion wave leaves the cavity wall at $t = 0$ and never returns nor encounters the outer boundary. The velocity field in the fluid is generated solely by the expansion wave. In late time, the velocity of the cavity wall ($\dot{R}$) becomes large enough that the surface work term becomes significant. However, due to the relatively small area of the cavity surface, especially in late time, it never reaches more than about 10% of the magnitude of the volume change work and kinetic energy terms.

The key difference between these two cases and the incompressible analytic formulation lies in the volume and surface work terms. The incompressible formulation mandates that the volume work be zero, requiring the surface work to be finite and negative. However, when allowing compressibility, until the expansion wave reaches the outer boundary, the volume work term is finite and the surface work is a small positive quantity. For cases where the wave never reaches the outer boundary (e.g. $S^\star = 401$), it is the volume work term that balances the change in

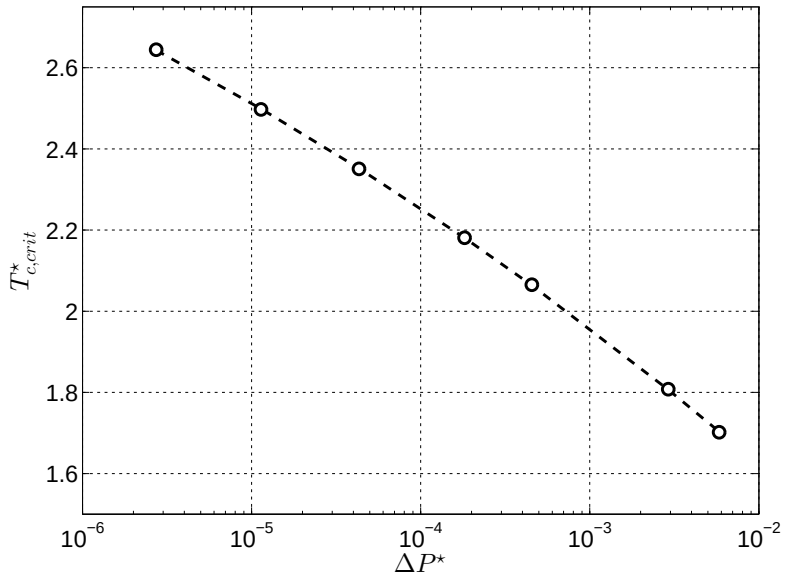

Figure 3.12: Scaled domain-limited collapse times, $T^\star_{c,crit}$, vs. initial pressure difference (circles) compared to power-law fit (dashed line). Collapse time is scaled by $R_o\sqrt{\rho/\Delta P}$. Driving pressure difference is scaled by ρc^2.

kinetic energy. Once the wave reaches the outer boundary, as seen in Figures 3.9 and 3.10, the incompressible formulation for the energy balance does a good job predicting the trends of the compressible case.

3.3.4 Scaling Compressibility-Limited Collapse Time

Observing Figure 3.6, we see that the maximum collapse time for a cylindrical cavity, $T^\star_{c,crit}$, has a dependence on ΔP, even though the collapse time T_c is already scaled by $T_o = R_o\sqrt{\rho/\Delta P}$. This extra dependence on ΔP, shown in Figure 3.12, appears to follow a power law of the form

$$T^\star_{c,crit} = \kappa_1 \left(\Delta P^\star\right)^{\kappa_2} + \kappa_3 \tag{3.23}$$

where κ_1, κ_2, and κ_3 are dimensionless fit parameters, and $\Delta P^\star$ is the pressure difference non-dimensionalized by the fluid density, ρ, and sound speed, c,

$$\Delta P^\star = \frac{\Delta P}{\rho c^2}. \tag{3.24}$$

Table 3.1: Coefficients fitting power-law model, Equation 3.23 to data given by Gemini.

Coefficient	Value	95% Confidence Interval
κ_1	-3.51	(-3.66, -3.35)
κ_2	0.0588	(0.0537, 0.0639)
κ_3	4.29	(4.11, 4.47)

The result of Equation 3.23 is a pre-factor for the collapse time analogous to the 0.915 typically quoted for the Rayleigh-Plesset equation. A least-squares fit of the data in Figure 3.12 to Equation 3.23 gives the coefficients shown in Table 3.1.

Figure 3.13 shows the results of this power law fit applied to data for pressures between 25 kPa and 6400 kPa. The location of the far-field boundary, $S^\star$, is scaled by the critical value, given by Equation 3.13. Critical values for $S^\star$ and $T_c^\star$ are matched within 1%. Of note here is that, while these values are predicted well, the curves themselves are no longer self-similar prior to $\bar{S} = 1$.

The power law given in Equation 3.23 appears to be a very good fit to the data presented. An important limitation, however, is the behavior as $\Delta P^\star$ goes to zero. In reality, when the driving pressure difference is zero, the result is a static cavity with infinite collapse time. The power-law model, however, predicts a finite collapse time, given by κ_3. This implies that there is some lower bound to the applicability of this fit that is not captured here.

3.4 Conclusions

The governing equation for an infinitely long cylindrical bubble in an incompressible fluid contains a logarithmic dependence on the amount of fluid available for the collapse motion, $S^\star$. Frequently, $S^\star$ is approximated as a constant in the range of 15 to 30, as first suggested by Birkhoff and Zarantanello [3, 6, 42].

In this chapter, cylindrical cavity dynamics were studied using an inviscid com-

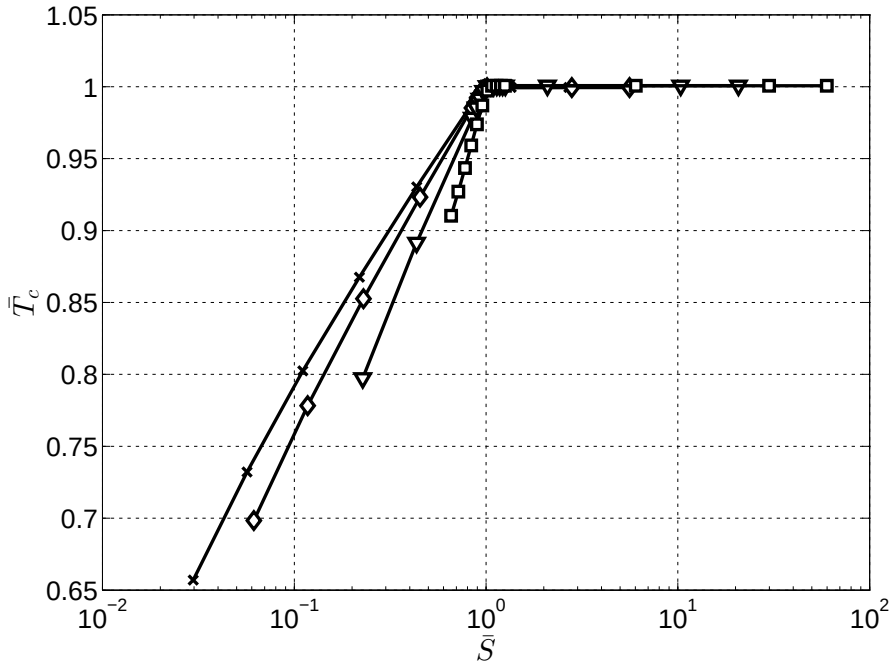

Figure 3.13: Cylindrical cavity collapse time, $\bar{T}_c$ versus domain size, $\bar{S}$ for various values of p_∞. All cases have a constant initial pressure ratio, $p_\infty/p_o = 1000$. Ambient pressures are 25 kPa (crosses), 95 kPa (circles), 1000 kPa (triangles) and 6400 kPa (squares). Cavity collapse times are scaled by the critical collapse times predicted by a power-law fit, Equation 3.23. Far-field boundary location is scaled by the distance an acoustic wave would travel in half of the predicted collapse time, Equation 3.13.

pressible hydrocode and compared to the results of the incompressible formulation assuming purely radial flow. Compressibility was shown to be a controlling factor in the dynamics of the cavity collapse, both as a means of limiting the amount of fluid mass accelerated by the collapse motion and as a source of damping. For a sufficiently large fluid domain, the collapse behavior becomes independent of $S^\star$ in the compressible calculation, while the incompressible formulation predicts a monotonically-increasing collapse time. Using the results of this study, a compressibility-limited collapse time can be predicted as a function of the ambient pressure, providing a rational limit for the effective domain size often used in slender body approximation models.

Chapter 4

Supercavitating Dart Experiments

4.1 Introduction

One real-world application where transient air and vapor cavities are important lies in the defense community. The U.S. Department of Defense has spent years developing technology to combat beach- and surf-zone mines. One such technology is Venom, a program focused on the capability to neutralize shallow-water mines, allowing for amphibious assault on beachheads. Venom is an air-delivered round which is dispersed in large clusters over a wide area, each individual projectile carrying a chemical payload. These projectiles, an example of which is shown in Figure 4.1, enter shallow water vertically at high velocities before impacting either the sea bed or a target mine. The chemical payload, diethylenetriamine (DETA), neutralizes the target's explosive charge. However, this reaction can be quenched by the intrusion of water. As a result, the collapse dynamics of the water entry cavity and the resulting pressure loads on the target are a topic of interest.

4.2 Experimental Set Up

A series of experiments was performed with the goal of recording the cavities and associated pressure fields created by these supercavitating projectiles during water entry. The projectile in question has a nominal nose radius of 3 mm, a shank radius of 6 mm, a length of 165 mm and a mass of 55 g.

The projectiles were fired vertically using a gas gun into a roughly 1 m deep by 1.2 m square water tank, shown in Figure 4.2. An instrumentation platform consisting of a target plate and a rake was placed inside this tank. The target

Figure 4.1: Pre-test photograph of supercavitating projectile for Test A3, $r_p = 3$ mm.

plate was constructed from 6 mm stainless steel with a 10 cm diameter orifice in the center, allowing the projectile to pass. A thin steel membrane was attached to the orifice to mimic a contiguous plate. Behind the orifice, a ballistic backstop (a layered structure of rubber, steel, and Lexan) was positioned to capture the dart.

The hydroballistics tank was lit with a bank of flash strobes at the front right-hand corner. The strobes were triggered with the data and video acquisition systems. The strobes were divided into two groups with separate delays to allow for adjustment of the total flash pulse duration. Typical total pulse duration was 30 ms, as shown in Figure 4.3.

Seven test cases were planned, as outlined in Table 4.1. The shank radius, mass, center of gravity, and overall length were held at their nominal value for all cases. Test A3 is considered nominal for the projectiles in question. Test cases with nose radii of double and half the nominal value were included to study their effect on cavity formation and collapse. Similarly, the effect of projectile velocity was considered by including tests at 50% and 150% of the nominal velocity.

Typical non-dimensional parameters are shown in Table 4.2. Both Reynolds number and Weber number are of the order $1{\times}10^6$, implying viscosity and sur-

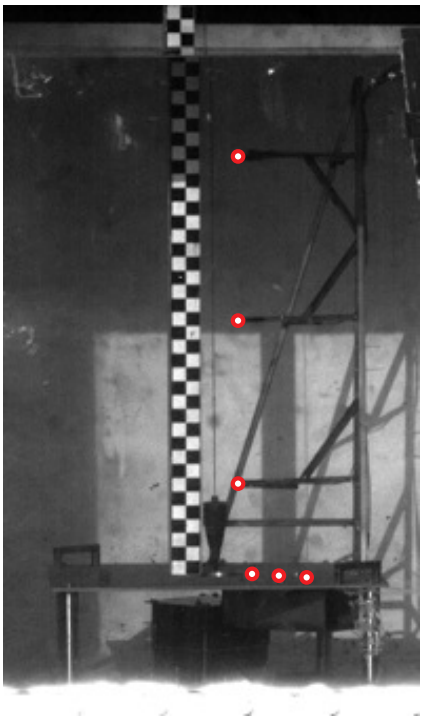

Figure 4.2: Pre-test photograph showing water tank, instrumented rake and plate, and fiducial marker. Transducer locations are marked with circles.

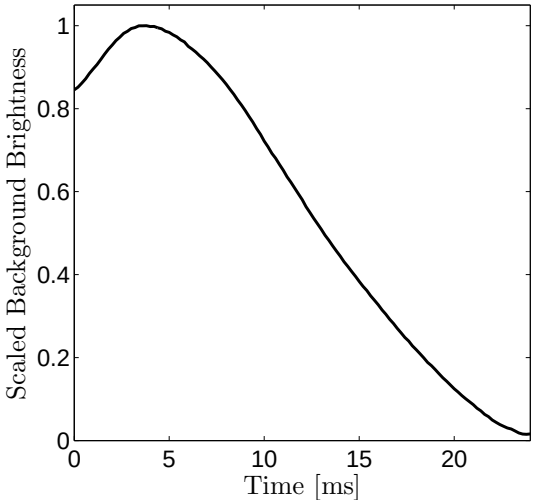

Figure 4.3: Scaled background brightness for Test A6. Brightness was averaged over a 50x50 px window in a region unobstructed by the cavity or fixtures and unaffected by shadows.

Table 4.1: Supercavitating projectile experimental parameters. Froude number is given by $Fr = v_o^2/gr_p$

Test	Target Vel. [m/s]	Reported Vel. [m/s]	Nose Radius [mm]	Fr [$\times 10^6$]	Outcome
A1	450	434	3.0	6.4	Success
A2	450	-	3.0	6.9	Failure
A3	300	276	3.0	2.6	Success
A4	300	-	3.0	3.1	Not Performed
A5	300	-	1.5	6.2	Failure
A6	300	252	6.0	1.1	Success
A7	150	194	3.0	1.3	Success

Table 4.2: Non-dimensional parameters for nominal projectile geometry and velocity.

Parameter	Expression	Value
Reynolds Number	$Re = \rho v_o r_p/\mu$	0.90×10^6
Froude Number	$Fr = v_o^2/gr_p$	3.0×10^6
Cavitation Number	$Ca = \Delta P/\frac{1}{2}\rho v_o^2$	2.1×10^{-3}
Weber Number	$We = \rho v_o^2 r_p/\sigma$	3.8×10^6

face tension are dominated by inertial forces, respectively. Additionally, the large Froude number implies that inertia dominates gravitational effects. Other researchers find cavity behavior correlates with Froude number. Here, as will be demonstrated, we observe cavity collapse behavior that appears to be independent of Froude number. This leave cavitation number, here on the order or 2×10^{-3}.

Of the seven planed tests, six were performed. Test A4 was omitted due to time constraints. Of the remaining six, Tests A2 and A5 were unsuccessful. In Test A2, the sabot catcher between the gas gun nozzle and the tank interfered with the dart, causing it to enter the water with a large angle of attack. In Test A5, the vapor

cavity generated was not wide enough for the shank of the projectile behind the nose. As a result, the cavity walls reattached to the dart, causing an irregular cavity and a sharply curved trajectory. Test A7 was successfully performed. However, a velocity of 150 m/s was below the lower bound of the calibration curve for the gas gun. As a consequence, a "best guess" was used for the input pressure in the driver section of the gas gun. This yielded a projectile entry velocity that exceeded the target value, reported at 194 m/s.

4.2.1 Data Acquisition and Analysis

Video was acquired with a digital high-speed camera (Vision Research Phantom v7) sampling at 5 kHz with a resolution of 560 by 600 pixels. This gives a spatial resolution of 2.2 mm/px for the provided field of view. Prior to each test, a calibration image, such as that shown in Figure 4.2, was taken with a fiducial marker to allow for accurate spatial data to be gathered from the video.

A total of six piezoelectric transducers (PCB Piezotronics ICP, models 113A21 and 113A26) were placed in the tank to record pressures. Three were placed vertically on a rake structure in the water column along the axis of penetration, shown in Figure 4.2. These transducers recorded pressures in the vicinity of (and occasionally inside) the cavity during expansion and contraction. Three more pressure transducers were spaced radially from the estimated impact point. The measurement ranges and locations for all six transducers is given in Table 4.3.

All transducers were sampled at 2 MHz. The pressure data were passed through a Bessel filter with a cutoff frequency of 200 kHz. No further filtering was applied in post-processing the results. The transducers have a discharge time constant greater than one second, meaning that their DC response is insignificant over the tens of milliseconds to be considered here. The transducers reported gage pressure. All plots shown use data that has been corrected by accounting for ambient atmospheric and hydrostatic pressure, which was calculated by measuring each transducer's location in the calibration image taken before each test.

Table 4.3: Pressure transducer nominal locations and pressure ranges. Locations are measured with respect to the center of the upper surface of the instrumented plate. Transducers report pressures with respect to ambient.

Transducer		Pressure Range [kPa]	Radial Location [cm]	Axial Height [cm]
Rake	Top	3450	6.35	76.2
	Middle	1380	6.35	45.7
	Bottom	1380	6.35	15.2
Plate	Inner	3450	7.62	0.0
	Middle	1380	15.2	0.0
	Outer	1380	22.9	0.0

4.3 Image Processing

The images captured with the high-speed video camera were processed manually with two separate procedures to generate two data sets, each with its own strengths and shortcomings. Automatic edge detection routines were considered initially, however spatially and temporally non-uniform lighting, as well as scattering caused by the internal splashes, made robust automation more labor-intensive than manual methods for this relatively small data set.

In the first image quantification process, demonstrated in Figure 4.4, video frames were analyzed in sequence to extract projected cavity profiles by manually tracing the apparent cavity outline at each point in time. These cavity profiles were then used to calculate an estimated cavity volume by integrating along the cavity length, assuming axisymmetry. This method gives good spatial consistency, as the images are processed one-by-one, yielding a smooth shape at each fixed time. However, the resulting temporal consistency at a fixed depth is found wanting. This is due to the fact that the cavity profile extracted from one image has no bearing on the profile extracted from the next. As a result, particularly when

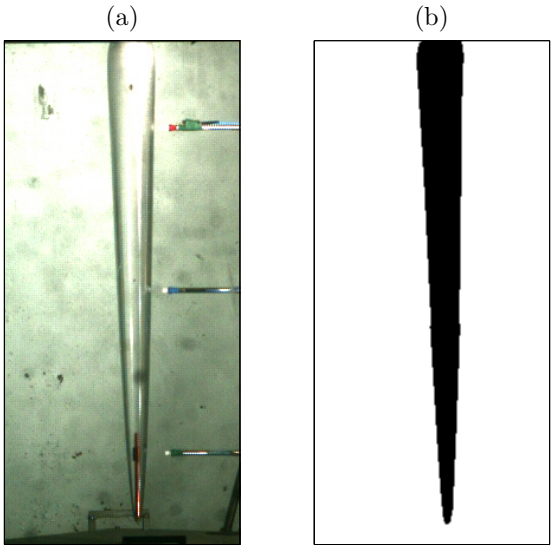

Figure 4.4: Example of cavity digitization results for fixed-time method. In (a), a cropped single frame from the high-speed camera is shown for Test A3 3.65 ms after water entry. The resulting cavity profile is shown in (b).

the local cavity radius is changing slowly (e.g. near its maximum), the temporal uncertainty in digitization can cause artificial oscillations in the radius history for a fixed depth.

To remedy this shortcoming, the images were processed again with a second technique. A visual depiction of this method is shown in Figure 4.5. Using this procedure, a new set of images was formed by concatenating single pixel slices at a fixed depth over the entire time record. The resulting images, an example of which is shown in Figure 4.5b, provide a complete picture of the cavity evolution over time at a fixed depth. This method facilitates the accurate extraction of cavity radius histories at fixed depths, in particular near the maximum radius. This method is not as appropriate for generating cavity profiles at fixed instants in time as, unlike in the previous method, the radius at one depth at a given time has no bearing on the radius at an adjacent point. As a result, apparent cavity profiles at fixed instants can be somewhat disjointed.

In light of this, each data set is used where it is strongest. When considering

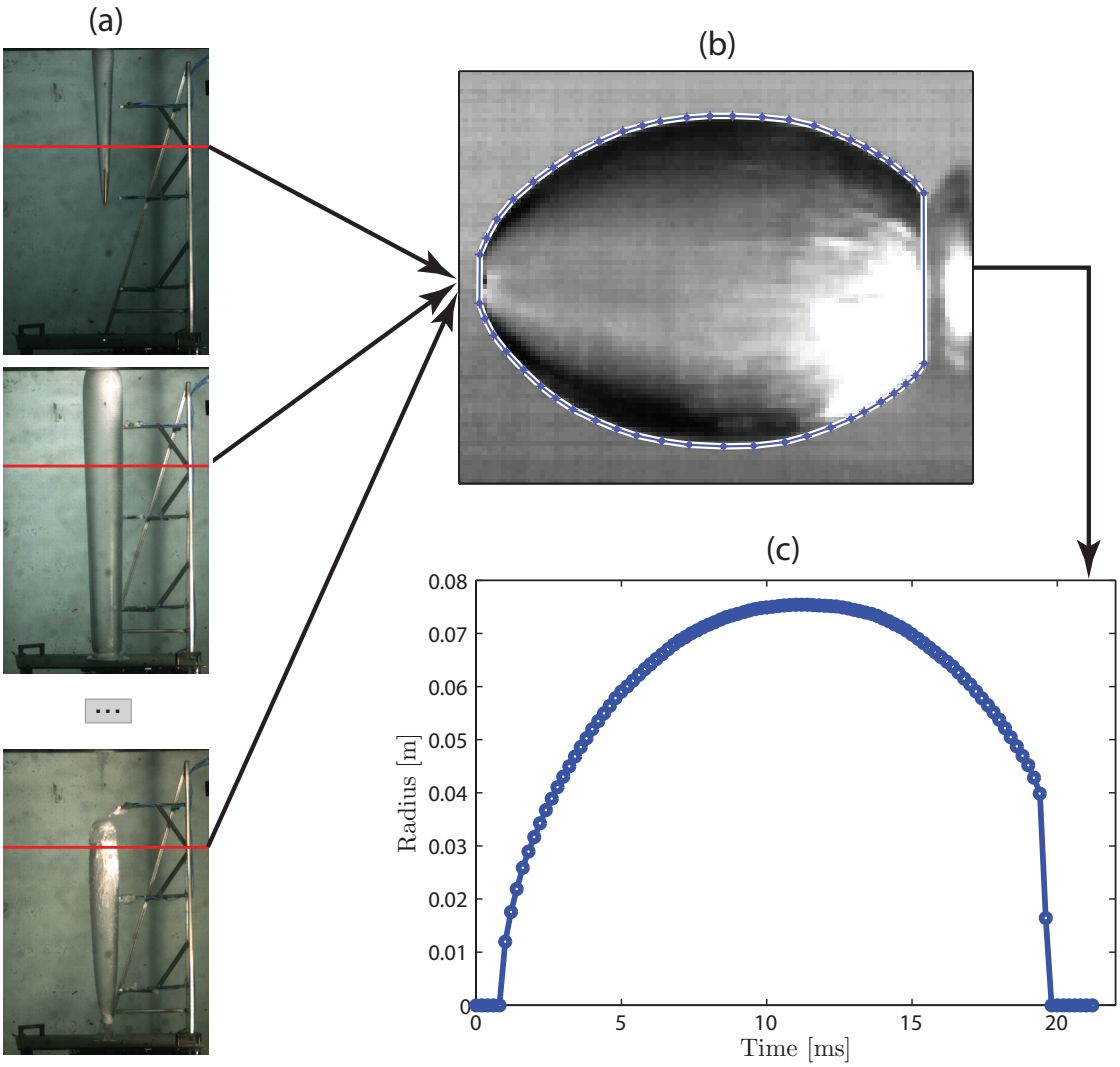

Figure 4.5: Cavity digitization procedure to obtain cavity radius histories at fixed depths. In (a), a single pixel slice (marked here in red) is taken from each frame from the high-speed video camera and concatenated to form the image in (b). The images are converted to grayscale and the exposure of each is adjusted to account for variation in lighting over the course of the test. Each image like the one in (b) is then manually outlined with a polygon, such as the one shown. The points selected are then used to interpolate over each point in time, obtaining the cavity radius history shown in (c).

gross features of the phenomenon or cavity volume histories, the first, fixed-time data set is strongest. When considering local cavity radius histories, the second, fixed-depth data set is utilized.

4.4 General Features

There are broad similarities across all four test cases. Figure 4.6 shows the pressure history for the rake transducers for Test A1. The previously-discussed estimated cavity volume is plotted to give a sense for the general temporal evolution of the cavity. In addition, cavity profiles are displayed as inset figures for several specific times. While this figure illustrates the results of a specific test, it demonstrates the general features common to all cases explored. Detailed differences noted between the individual cases will be discussed in later sections.

Following the impact of the dart with the water surface, all transducers show an acoustic pulse due to the shock wave created at the impact point. The arrival time of the shock wave is shown in Table 4.4 for the example case alongside the expected arrival time. The speed of sound for water at 15°C is estimated to be 1464 m/s. All measured times are within 2.5% of estimated values. Reflections of this initial shock wave are seen at all transducers as the acoustic wave reflects off surfaces of the tank. A few of these reflections are highlighted in Figure 4.7. The magnitudes of these shock waves and reflections cannot be truly quantified because they are above the frequency response of the data acquisition system and, therefore, filtered.

As the dart travels downward, a cavity is created and envelops the projectile as the fluid separates at the nose. The cavity walls are, for the most part, smooth during formation. As the nose of the dart passes each of the rake transducers, a pressure peak is observed that results from the stagnation pressure at the tip of the dart (see Figure 4.7a). These peaks last much longer (∼1 ms) than those created by the initial shock wave (∼0.02 ms). As the dart approaches the target plate,

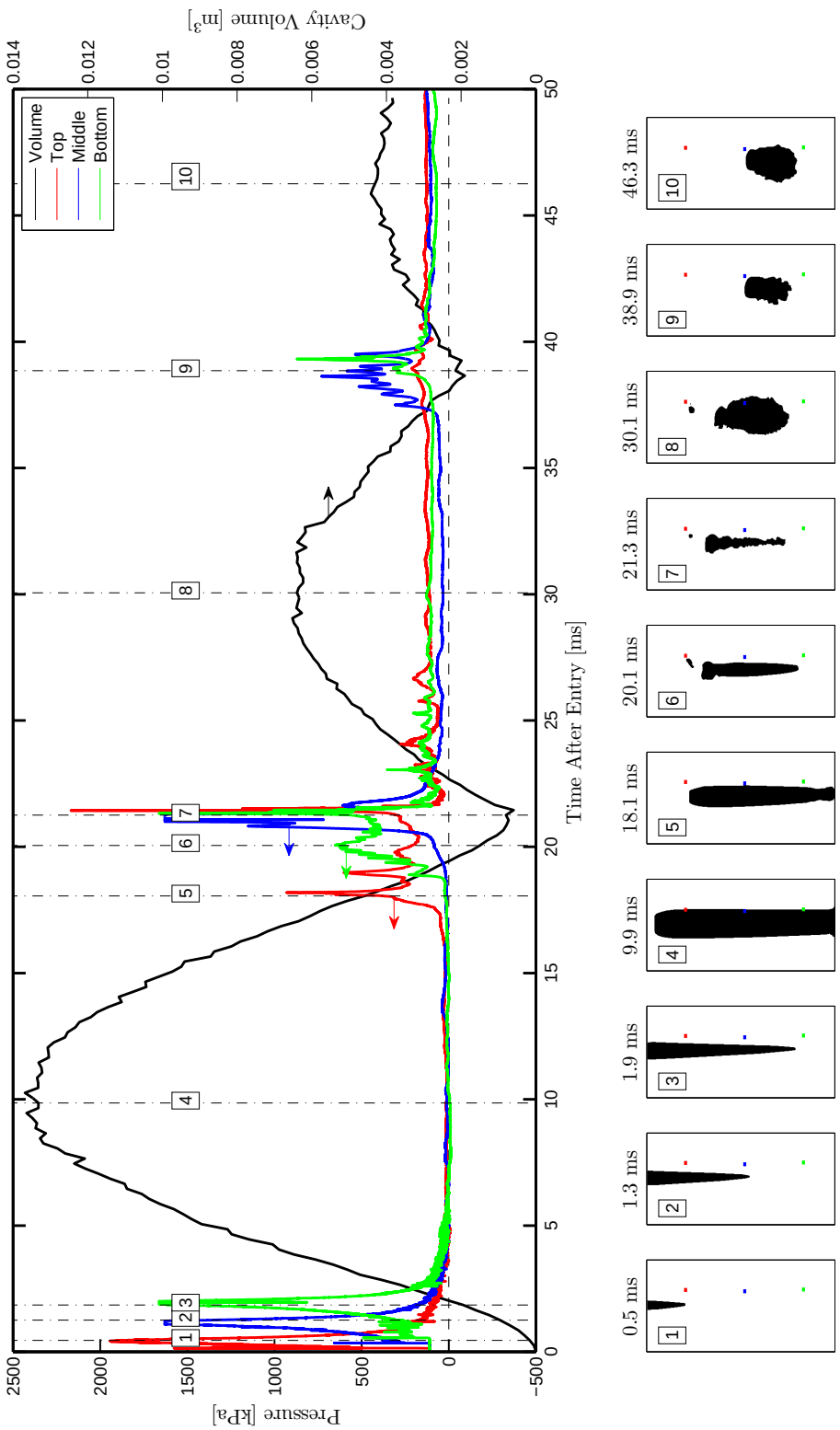

Figure 4.6: Pressure history along axis of penetration and cavity volume history for A1. Times for inset figures are marked with vertical lines. Colored dots in each inset image correspond to the location of the pressure history of the same color.

Table 4.4: Shock wave measured and expected arrival times for Test A1.

Transducer	Distance [m]	Measured Time [ms]	Estimated Time [ms]
Rake Top	0.212	0.149	0.145
Rake Middle	0.512	0.349	0.350
Rake Bottom	0.815	0.555	0.557
Plate Inner	0.968	0.670	0.661
Plate Middle	0.977	0.677	0.667
Plate Outer	0.992	0.688	0.678

pressure there undergoes a similar increase, as shown in Figure 4.7b. The pressure peaks as the nose approaches the target plate, and then decreases until the dart impacts the ballistic backstop, at which point another short pressure pulse ($\sim$0.02 ms) is measured at the inner plate transducer. Above the target plate, the pressure continues to decrease, and drops below the initial ambient hydrostatic pressure, to a minimum approaching the vapor pressure of the water, corresponding to the transducer entering the cavity.

After the projectile impacts the ballistic backstop, spray is observed to disturb the walls of the cavity in the vicinity of the target plate. As a result, the cavity walls are observed to become dimpled and irregular in this region. At the free surface, the splash at the impact point closes due to the suction generated by the negative pressure in the cavity. During this closure, spray disturbs the walls of the cavity near the free surface. This results from liquid drops being entrained within the cavity during closure event, as well as the formation a strong re-entrant jet at the free surface. The closure ultimately creates a seal at the water surface, as can be seen in Figure 4.8. The top of the cavity then detaches from the free surface and begins to move downward, as shown in Figure 4.9. Here, the re-entrant jet created by the splash closure and surface seal is observed. The cavity walls continue to

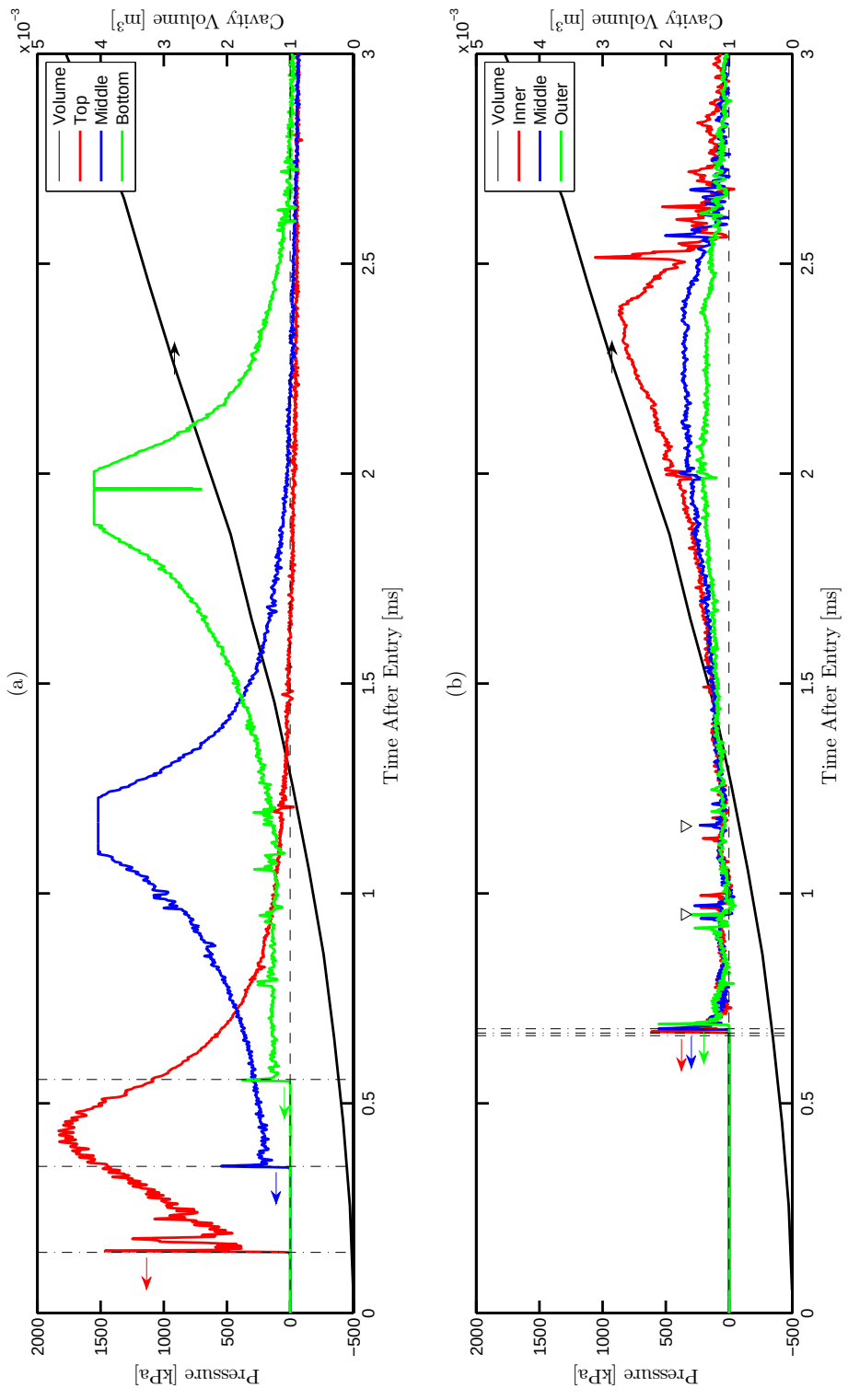

Figure 4.7: Transient pressure record 3 ms after entry for Test A1 (a) rake transducers and (b) plate transducers. Expected shock wave arrival times are indicated with dotted lines. Select reflections off tank walls are marked with triangles.

move outward such that maximum volume occurs after surface seal, as can be seen in Inset 4 of Figure 4.6.

Following surface seal, the apex of the cavity moves downward, initially with a velocity that is approximately uniform across all cases. It later accelerates downward, often shedding a small bubble from its top in the process. From here, the cavity collapses completely. The mode of collapse seems to be determined by what happens during the shedding event. For cases where the upper surface of the cavity is wide, the apex gradually accelerates, eventually meeting the bottom surface of the cavity near the middle of the water volume. For cases with a narrower apex, collapse seems to be primarily radial, leading to a shedding event that is immediately followed by the rapid acceleration of the apex, causing the upper surface to impact the target plate before the cavity detaches there.

As is the case for bubble collapse in general, a high pressure is created as the cavity reaches its minimum volume. In some cases, it then rebounds, reaching a secondary maximum volume, this time with a much rougher, dimpled surface. Following the first collapse, the interior of the cavity appears to be a mixture of air, water droplets, and water vapor. This collapse and rebound cycle continues, each time with a smaller maximum volume, until the vapor returns to a liquid state and the cavity dissipates.

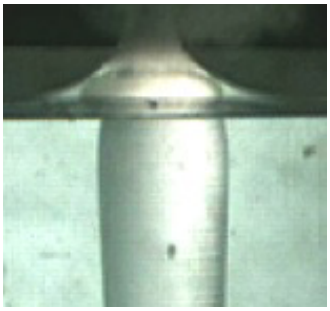

Figure 4.8: Splash closure creating surface seal 3.7 ms after water entry during Test A3.

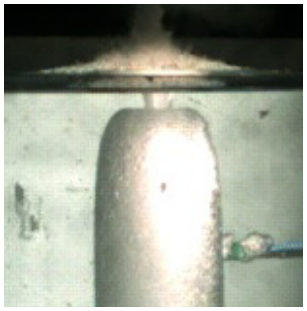

Figure 4.9: Cavity retracting from the free surface 6.5 ms after water entry during Test A3.

4.5 Specific Features

4.5.1 Test A1: r_p = 3 mm, v_o = 434 m/s

Test A1 was conducted using a dart with the nominal geometry (r_p = 3 mm). The planned entry velocity was 50% higher than the nominal value, at 450 m/s. The reported entry velocity was 434 m/s. The pressure history and cavity profiles are shown in Figure 4.6. This case was unique in that the dart was somewhat unstable following entry, likely a result of a slightly oblique impact. This caused its tail to oscillate within the cavity, impacting the cavity wall several times. This is evidenced by spray and streaking that can be seen in video footage, as shown in Figure 4.11. However, because a cavitating disk is hydrodynamically stable and the magnitude of the angular oscillations was never more than about 5°, this did not have a discernible effect on the trajectory of the projectile or the symmetry of the cavity. This effect may have led to an artificially high drag coefficient, as will be demonstrated in Section 4.6.

The primary differentiating features in this case are in the collapse. The pressure history and cavity volume are plotted for the final 4 ms of the first collapse event in Figure 4.10. The inset figures show a nearly frame-by-frame version of the collapse. Following surface seal, the apex of the cavity detaches from the free surface and begins to move downward. Prior to this, the rake pressure transducers were enveloped within the cavity. During retraction from the free surface, the cavity detaches from the top rake transducer, shedding a small bubble that remains in the vicinity of the transducer. Oscillations of this bubble cause the pressure oscillations occurring between 18 and 22 ms, marked in Figure 4.6. This was verified by comparing the primary frequency of the pressure signal to the visually-observed frequency of the small bubble. These peaks are artifacts of the experimental procedure and should not be considered features of the phenomenon itself.

As the apex of the cavity begins to move downward, the bottom surface of the

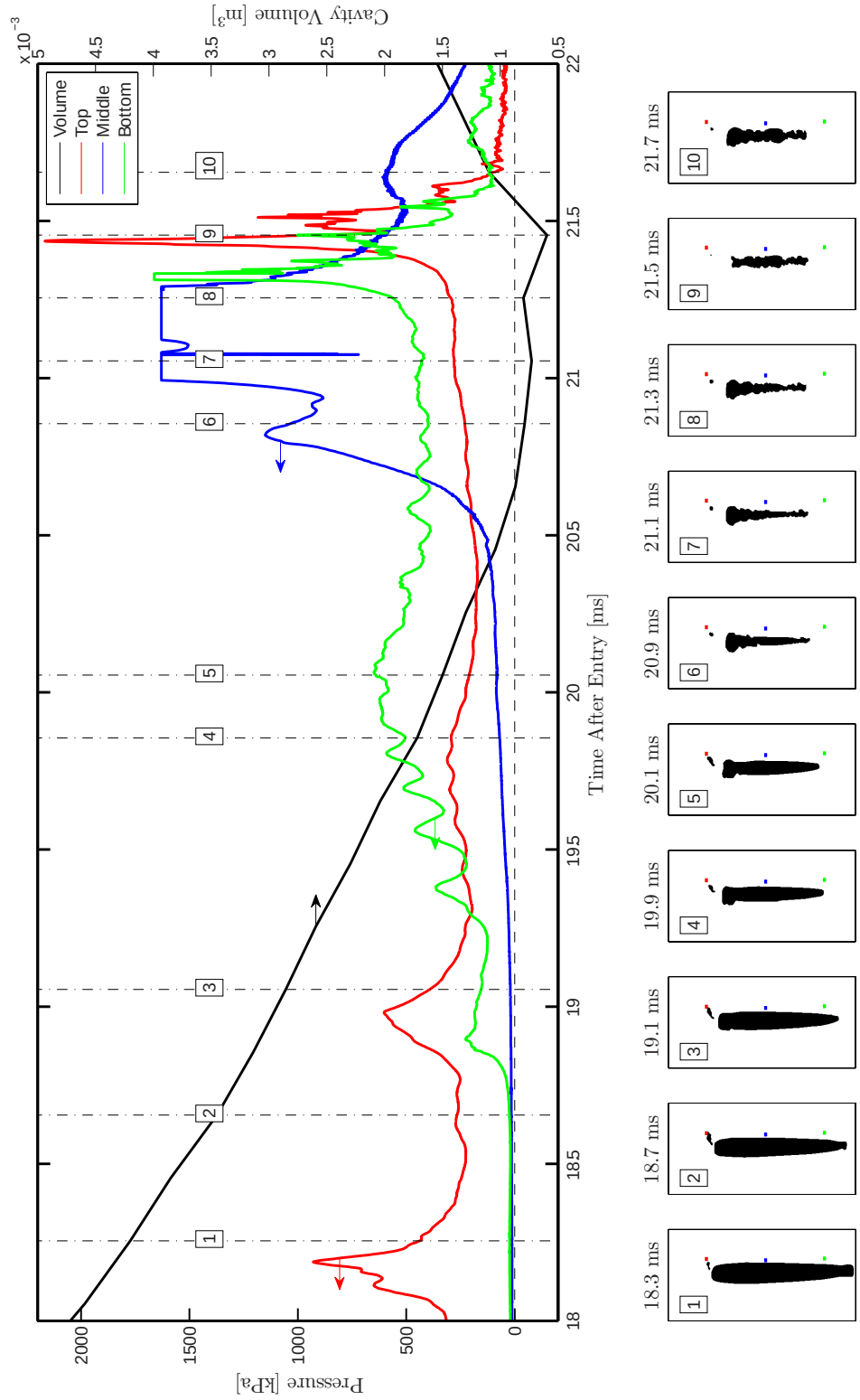

Figure 4.10: Pressure history along axis of penetration and cavity volume history during collapse for Test A1. Colored dots in each inset image correspond to the location of the pressure history of the same color.

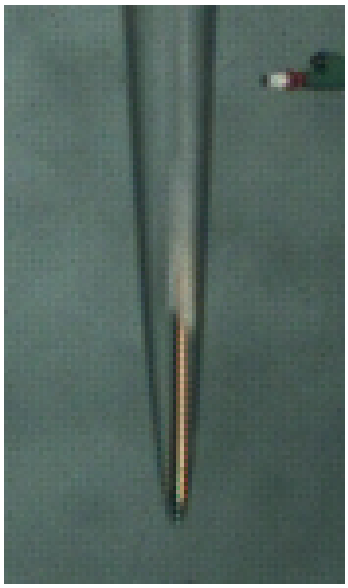

Figure 4.11: Dart impacting cavity wall 1.4 ms after water entry during Test A1.

cavity detaches from the plate and accelerates upward, reaching a velocity of 120 m/s. The apex moves at a slower rate than the bottom surface of the bubble, moving downward at approximately 63 m/s. As the bottom surface of the bubble moves past the bottom rake transducer, it creates a high pressure, as observed at Inset 5 of Figure 4.10. This peak is relatively long and gradual, beginning from around 19 ms and lasting though the point of the collapse at 21 ms with a peak pressure of about 550 kPa.

At Inset 6 in Figure 4.10, the sides of the cavity start to collapse inward, creating a high pressure of 1030 kPa. At total collapse, the cavity reaches its minimum volume and creates large pressures that cause all three rake transducers to clip. The pressure in the vicinity of the middle rake transducer causes it to clip for 0.5 ms while the other two rake transducers clip for $\sim$0.02 ms.

The cavity then rebounds, reaching a secondary maximum volume before collapsing and rebounding again, as shown in Figure 4.6. In these secondary cycles, the cavity more closely resembles a spherical bubble.

4.5.2 Test A3: r_p = 3 mm, v_o = 276 m/s

Test A3 used the nominal configuration for the projectile in question, with a tip radius of 3 mm and a nominal entry velocity was 300 m/s. The reported entry velocity was 276 m/s. The pressure record for rake transducers is shown with selected cavity profiles in Figure 4.12. Up until the point of collapse, this test fits well with the previously-described general phenomenon.

After detaching from the free surface, the apex of the cavity moves downward, as described previously. Unlike the previous case, however, the cavity remains attached to the target plate during this time. As a result, instead of the behavior seen previously in Test A1, where the upper and lower surfaces meet near mid-height, the apex of the cavity in this case collapses downward in a "zipper-like" fashion, leaving a helical, spray-inhabited wake behind, as can be seen in Figures 4.12 and 4.13. This result is similar to that of Shi and Itoh, who saw similar behavior in the cavity generated by a .22LR rifle round fired into a water tank [33]. This collapse starts approximately 14.6 ms after dart entry (Inset 5 of Figure 4.13) as the sides of the cavity collapse radially just below the apex, shedding a small toroidal bubble. Following this shedding event, the apex accelerates downward, creating high pressures, as can be seen at Insets 6 and 8 in Figure 4.13. Before it reaches the bottom plate, the sides of the cavity collapse inward completely, leading the cavity to reach its minimum volume and creating a large pressure in the vicinity of the bottom transducer, which clips for approximately 0.25 ms. The spiral-shaped cavity wake rebounds briefly before rapidly dissipating at approximately 24 ms, causing a sharp decrease in apparent volume, as can be seen in Figure 4.12.

4.5.3 Test A6: r_p = 6 mm, v_o = 252 m/s

Test A6 used a dart with a cavitator that was twice the nominal radius, at 6 mm. The planned entry velocity was 300 m/s. The reported entry velocity was 252 m/s. The pressure history for rake transducers is shown with apparent cavity profiles in

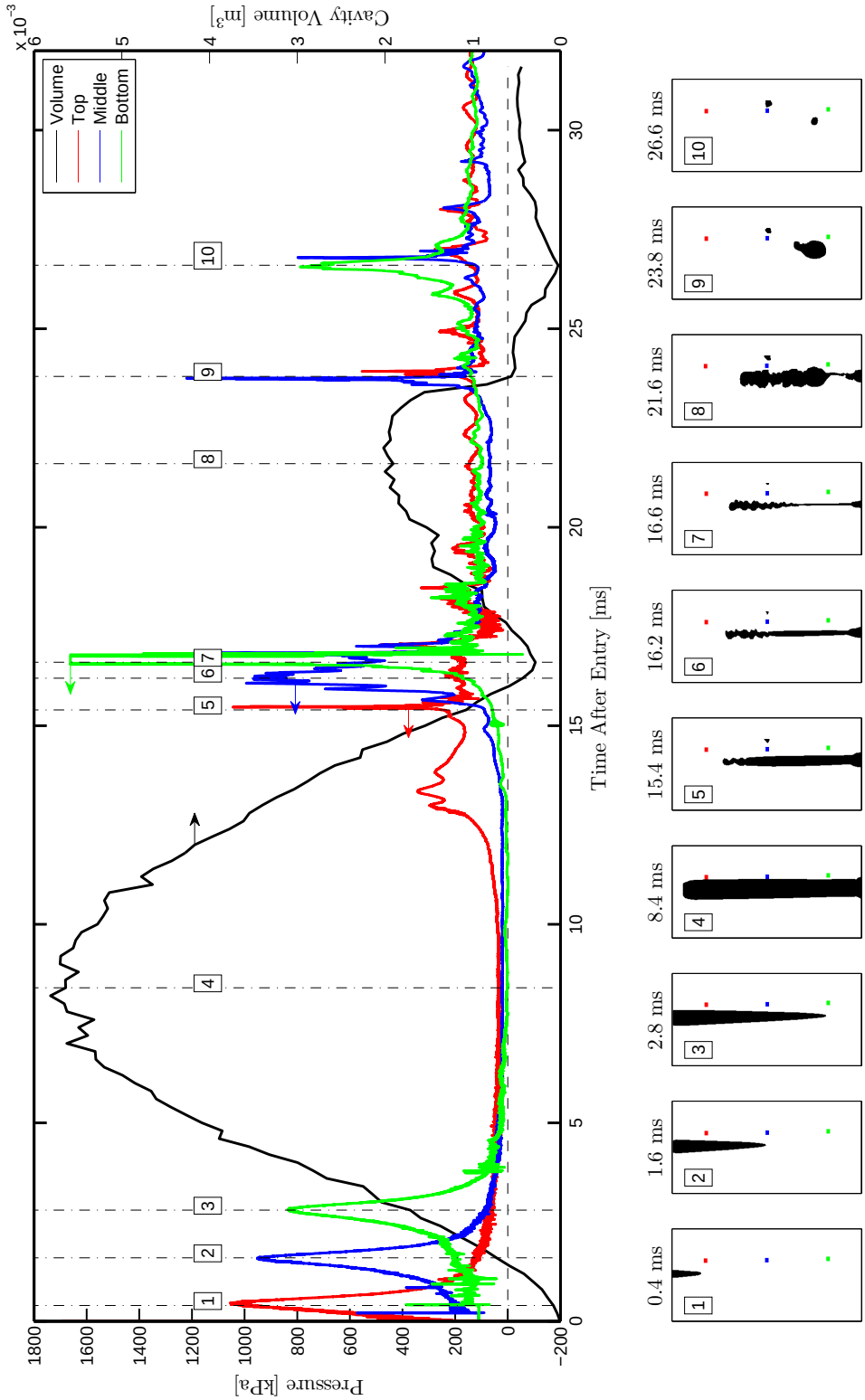

Figure 4.12: Pressure history along axis of penetration and cavity volume history for Test A3. Colored dots in each inset image correspond to the location of the pressure history of the same color.

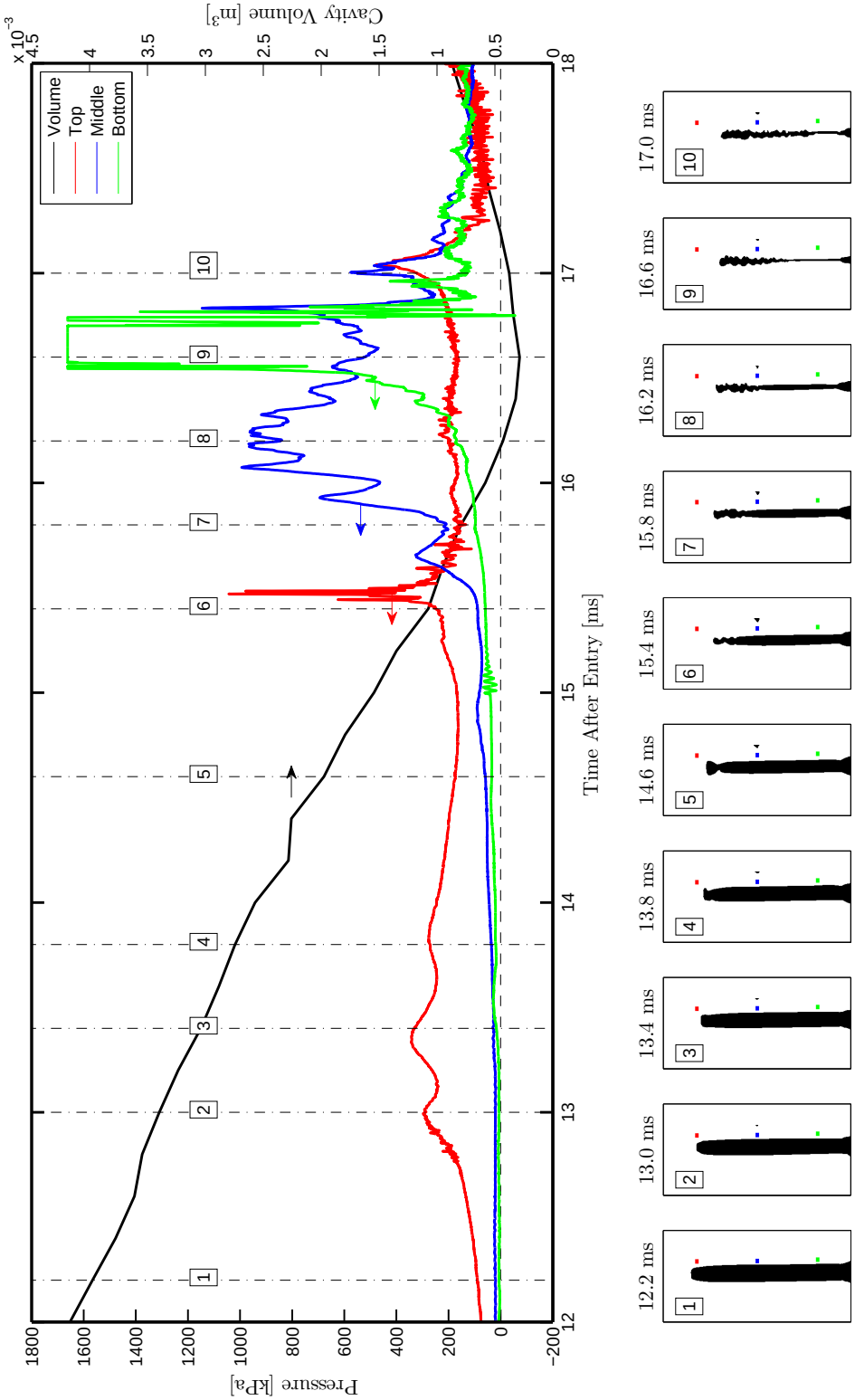

Figure 4.13: Pressure history along axis of penetration and cavity volume history during collapse for test A3. Colored dots in each inset image correspond to the location of the pressure history of the same color.

Figure 4.14.

This test varies from the general morphology in the details of the cavity collapse. After surface seal, the bottom surface of the cavity detaches from the target plate and moves upward faster than the apex moves downward, as was the case for Test A1.

As the bottom surface of the cavity passes the bottom rake transducer, it causes a high pressure there, which increases gradually from 19.0 until 19.7 ms, when it rapidly peaks, causing the transducer to clip for 0.01 ms. As the cavity detaches from the top rake transducer at approximately 20.2 ms, it sheds a bubble that remains and oscillates in the vicinity of the transducer, causing the pressure oscillations seen there between 20.7 and 21.6 ms, as shown in Figure 4.15. As was the case for Test A1, this is an artifact of the experiment itself and should not be considered a feature of the cavity collapse phenomenon.

At 22 ms, the side walls of the cavity begin to collapse, causing a peak pressure of 800 kPa before decreasing just prior to total collapse. Total collapse occurs at 22.6 ms, as the cavity reaches its minimum volume. This causes a high pressure in the region of collapse, causing the middle rake pressure transducer to clip for 0.35 ms. The pressure in the vicinity of the top and bottom transducers peaks at approximately 1000 kPa shortly after this collapse.

Following collapse, the cavity rebounds, reaching a secondary maximum at 33.6 ms before collapsing again. Unlike Test A3, this volume does not dissipate rapidly during the second collapse. It is hypothesized that this is a result of greater air content in the cavity due to the larger cavitator radius, as this leads to a larger opening at the free surface, allowing more air to be entrained in the cavity prior to surface seal.

4.5.4 Test A7: $r_p = 3$ mm, $v_o = 194$ m/s

Test A7 used a projectile with the nominal tip radius of 3 mm at a low entry velocity. The planned initial velocity was 150 m/s, but uncertainty in gas gun

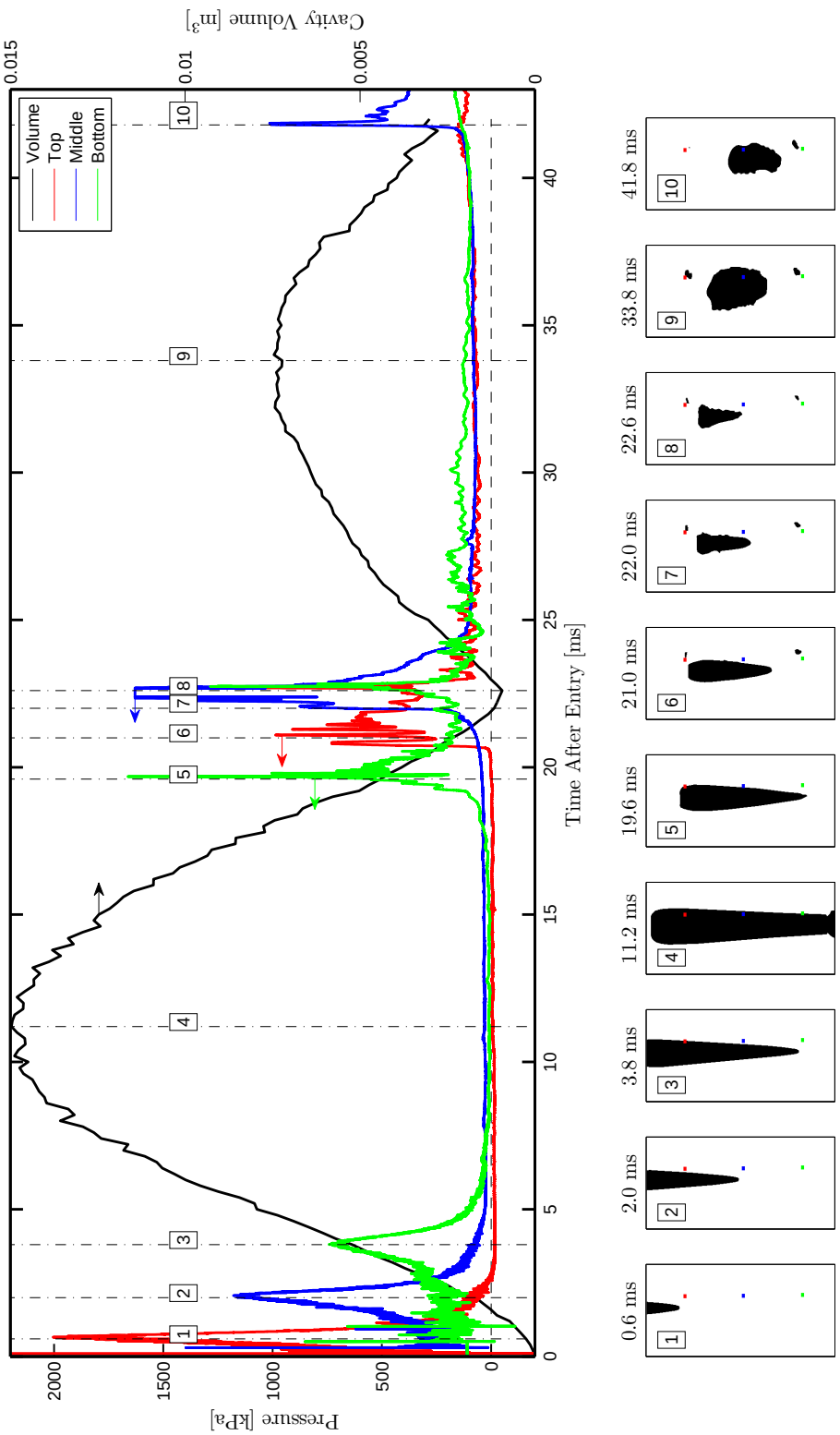

Figure 4.14: Pressure history along axis of penetration and cavity volume history for Test A6. Colored dots in each inset image correspond to the location of the pressure history of the same color.

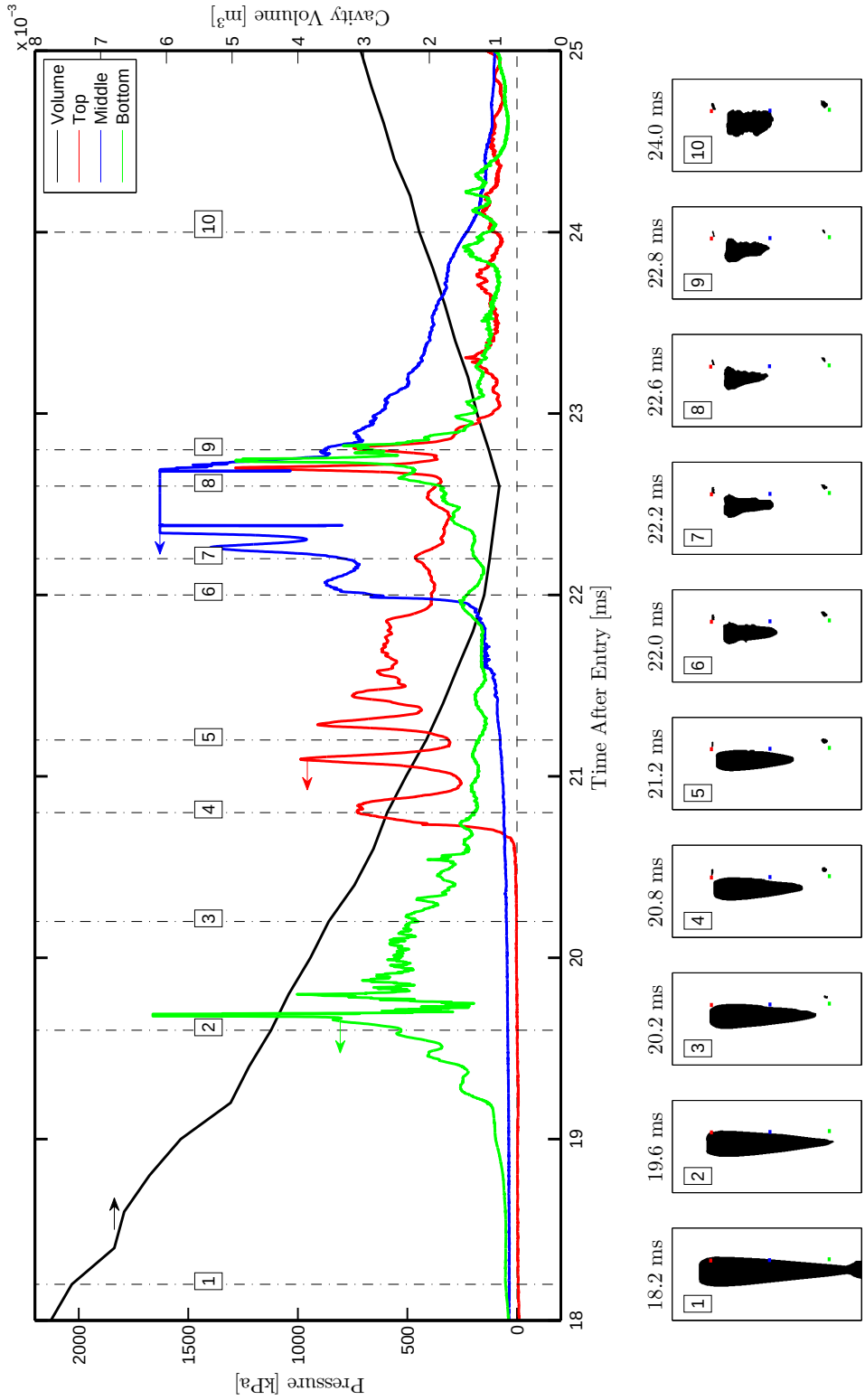

Figure 4.15: Pressure history along axis of penetration and cavity volume history during collapse for Test A6. Colored dots in each inset image correspond to the location of the pressure history of the same color.

calibration led to a higher than planned initial velocity, reported at 194 m/s. The pressure history for this test is shown in Figure 4.16.

This case had the lowest initial velocity, resulting in the smallest cavity. The cavity does not present a total collapse at a fixed height in the water, as was observed in other cases. Surface seal is nearly complete before the dart reaches the plate, as can be seen in Inset 3 in Figure 4.16. As the upper surface of the cavity moves downward, the sides collapse inward locally near the top, shedding a small bubble and causing the peak pressure highlighted at Inset 7 of Figure 4.16. After this shedding event, the apex of the cavity moves rapidly downward toward the plate, leaving a spiral-shaped wake like that seen in Test A3.

This case lacks the total collapse observed in previous cases that is caused by the retraction of the ends of the cavity. The local collapse overpressure is much less as a result, on the order of the stagnation overpressure seen when the dart passes. There is no significant rebound in this case. The spiral-shaped wake left as the cavity collapses downward oscillates briefly before dissipating.

This case had a similar initial Froude number as the previous test (1.3×10^6 versus 1.1×10^6). However, we observe a fundamentally different collapse mode, implying that beyond a certain range, cavity behavior becomes insensitive to *Fr*.

4.6 Dart Trajectories

Having accurate knowledge of a projectile's trajectory is of the utmost importance when studying the cavity it creates at high velocities, as the reduction in velocity along the trajectory is the source of energy for the work required to expand the cavity. This requires accurate values for the initial velocity, v_o, and drag coefficient, C_D. Variance in these two parameters can have great effect on gross features of the cavity phenomenon, as any errors are compounded by the integration used to calculate the trajectory. Errors in either affect both the timing (e.g. when the cavity forms at various depths) and how much energy is deposited into the fluid

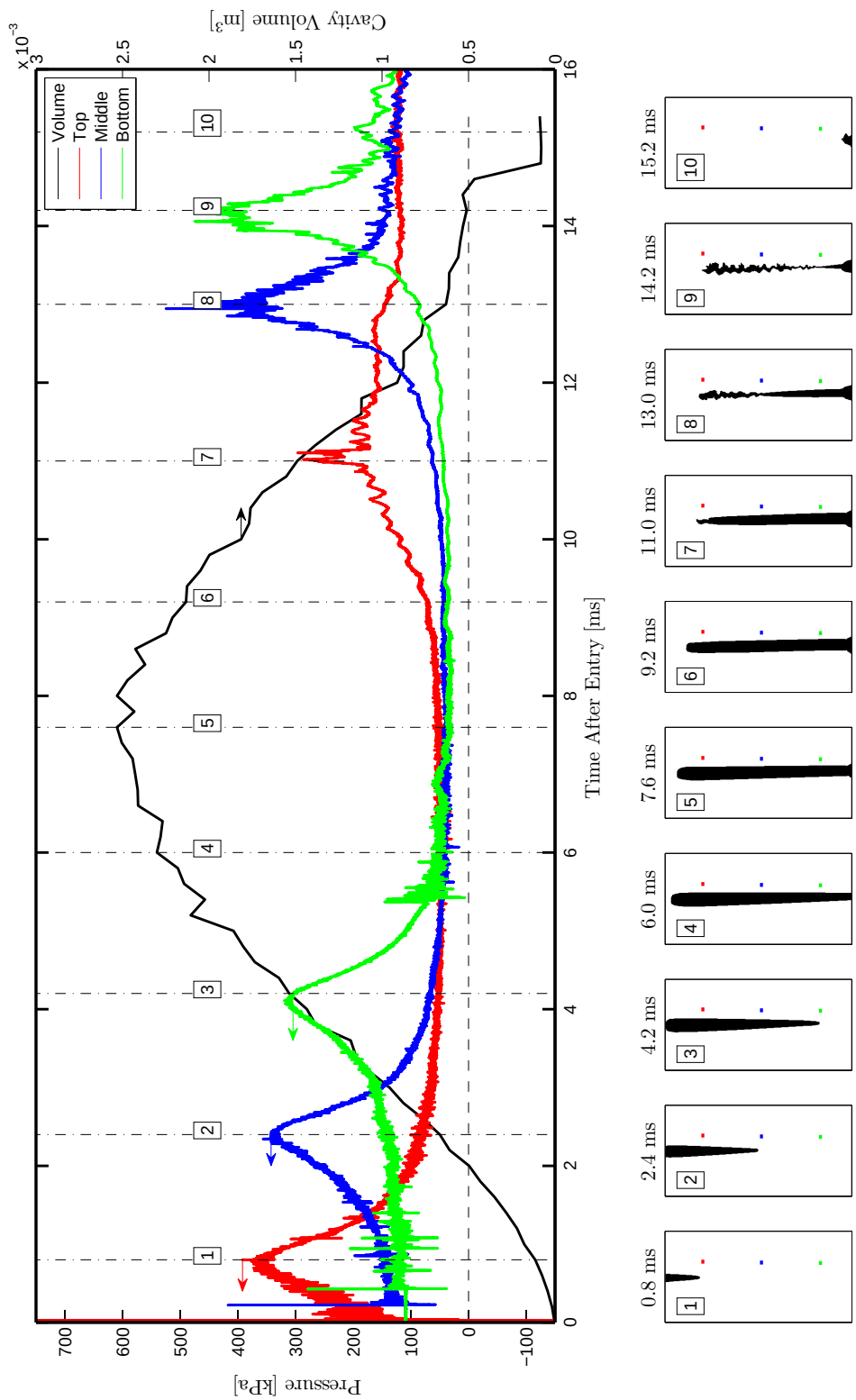

Figure 4.16: Pressure history along axis of penetration and cavity volume history for Test A7. Colored dots in each inset image correspond to the location of the pressure history of the same color.

(i.e. the cavity maximum radius at a given depth).

Experimental trajectories were extracted from the high-speed video footage by tracking the location of the tip of the dart as it moved through the fluid volume. Estimates of the initial velocity were reported via radar (shown in Table 4.1). Values for C_D and v_o were calculated using these two inputs.

For a body entering water, the ODE governing its motion is

$$m_p \ddot{z} = m_p g - \frac{1}{2}\rho \dot{z}^2 C_D A_p, \tag{4.1}$$

where z is penetration depth, dots denote derivatives with respect to time, m_p and A_p are the projectile's mass and frontal area, respectively, ρ is the fluid density, and g is acceleration due to gravity. For each case, Equation 4.1 was solved numerically for a range of initial velocities (bracketing the value reported by radar) while altering the value of C_D until errors in the calculated trajectories were minimized. For our purposes, C_D is assumed to be a constant for a given test.

The resulting values are shown in Table 4.5. The calculated initial velocities differ slightly relative to the values reported by radar (shown in Table 4.1), with the greatest adjustment being made to Test A6 (+26 m/s). It is hypothesized that, in that case, the radar may have inadvertently measured the velocity of a fragment of the sabot instead of the projectile. The drag coefficients are consistent across the four cases, showing variations of ±7% from the mean. Test A1 has the highest drag coefficient, which is likely a consequence of the tail repeatedly impacting the cavity wall, as seen in Figure 4.11.

The computed trajectories for all four cases are shown in Figure 4.17 with the experimentally-observed trajectories. The resulting RMS error relative to the experimentally-observed trajectories is small, on the order of 1 pixel, which is within the uncertainty of the location of the dart tip in a given image.

At low cavitation number (Ca), the drag coefficient of a blunt supercavitator is usually taken as [35]

$$C_D = C_{Do}\left(1 + Ca\right), \tag{4.2}$$

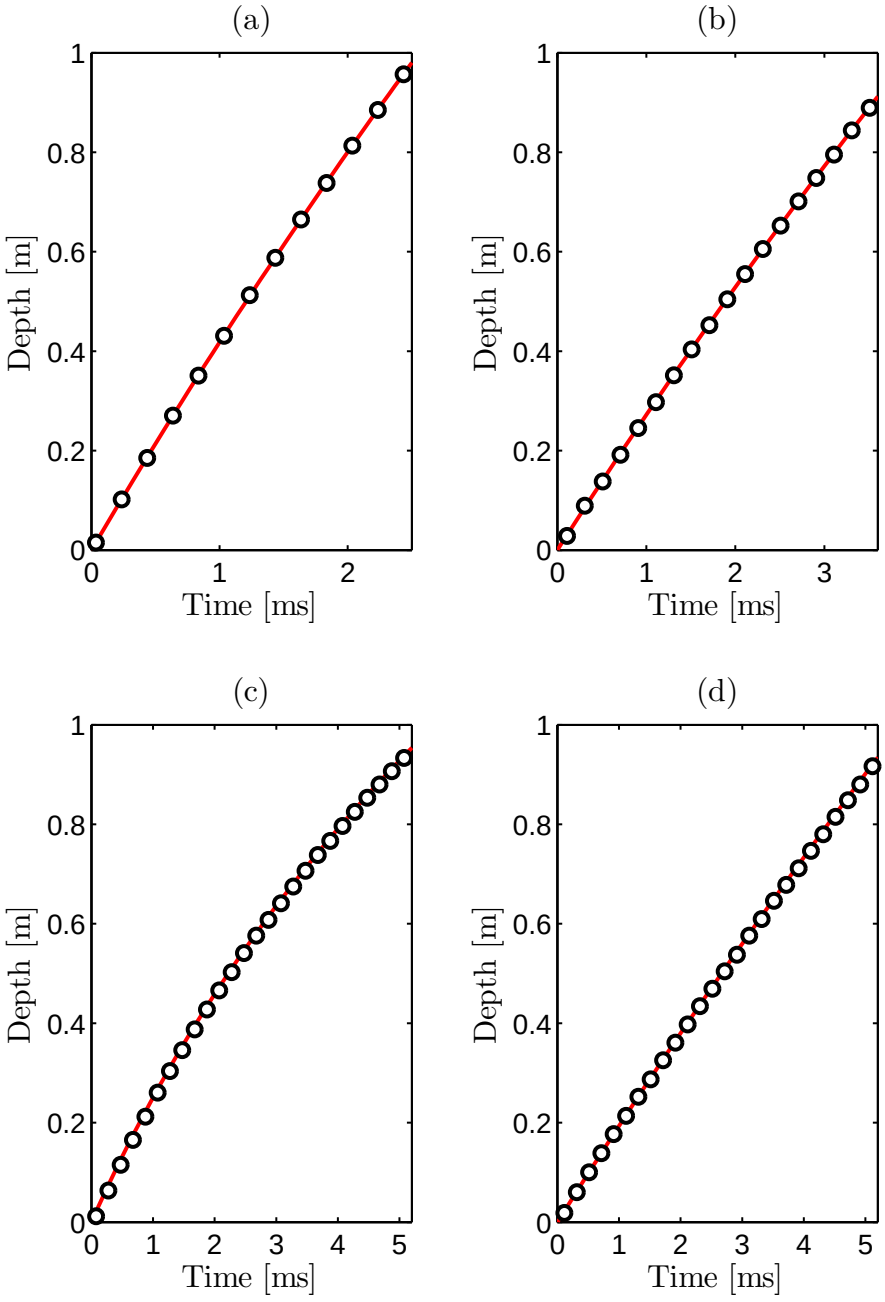

Figure 4.17: Calculated dart trajectories (lines) as compared with experimentally observed trajectories (circles) for Tests (a) A1, (b) A3, (c) A6, (d) A7. Initial conditions, calculated drag coefficients, and RMS errors are presented in Table 4.5.

Table 4.5: Calculated dart trajectory parameters and error from ODE fit.

Test	Initial Vel. [m/s]	Drag Coeff.	RMS Error [mm]	RMS Error [px]
A1	438	0.864	0.840	0.382
A3	280	0.839	1.49	0.677
A6	278	0.796	0.951	0.432
A7	197	0.754	2.43	1.10

where C_{Do} is the free-streamline ($Ca = 0$) value. For the current work, Ca is on the order of 0.002. C_{Do} is usually taken as 0.80, which agrees well with these calculated values.

4.7 Cavity Volume Scaling

As a first attempt at understanding the observed cavity collapse phenomenon, the volume history data taken from the high speed video of the four cases were compared. As a rudimentary means of understanding temporal trends, the volume data for each case was normalized by its maximum value, V_{max}. The time was scaled by the time it took each cavity to collapse to a minimum from its maximum value, T_c. The results are shown in Figure 4.18. During cavity formation and collapse, the agreement between all cases is reasonable. All cases reach their maximum value at $t^\star \sim 1$ and collapse at $t^\star \sim 2$. Following the initial collapse, however, agreement between the cases diminishes.

The effect of projectile velocity can be seen in the expansion phase of all four cases. Tests A3 and A6, with entry velocities near 300 m/s, grow at similar rates, with Test A1 ($v_o = 434$ m/s) and A7 ($v_o = 194$ m/s) expanding faster and slower, respectively.

Rayleigh's model for a spherical bubble collapse was used as a more significant

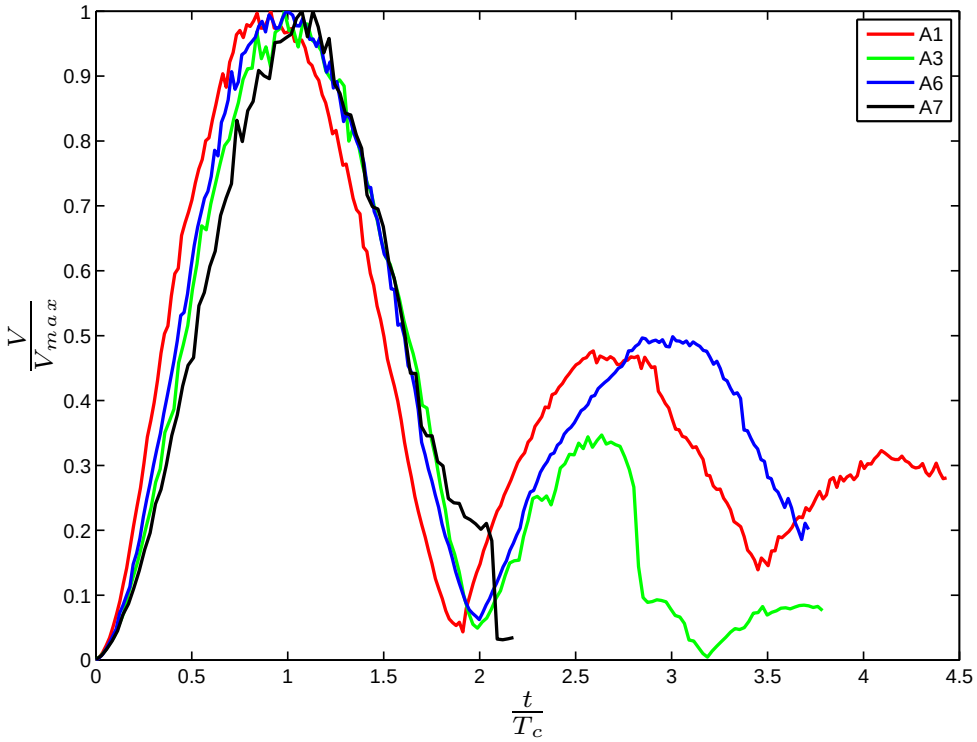

Figure 4.18: Normalized cavity volume histories. Volume is scaled by the maximum cavity volume. Time is scaled by the amount of time between the maximum value and the first collapse.

attempt at normalizing the data. The energy contained in a bubble, E_b, is

$$E_b = V_{max} \left(p_\infty - p_i \right), \tag{4.3}$$

where V_{max} is the maximum cavity volume, p_∞ is the ambient fluid pressure, and p_i is the pressure of the vapor and gas in the cavity, in this case assumed to be the vapor pressure of water at 15°C. The sole source of energy for cavity formation is the kinetic energy lost by the projectile as it passes through the water,

$$E_k = \frac{1}{2} m_p \left(v_o^2 - v_f^2 \right), \tag{4.4}$$

where m_p is the projectile mass, v_o is the initial velocity, and v_f is the velocity of the projectile as it impacts the target plate. Equating Equations 4.3 and 4.4, the expected maximum volume of the cavity is

$$V_{max} = \frac{1}{2} m_p \frac{v_o^2 - v_f^2}{p_\infty - p_i}. \tag{4.5}$$

For a spherical bubble, Rayleigh's model gives a collapse time

$$T_c = 0.915 R_o \sqrt{\frac{\rho}{p_\infty - p_i}}, \tag{4.6}$$

where R_o is the maximum radius. Here, an equivalent value of R_o is calculated by finding the radius of a spherical cavity with the same volume as the maximum observed volume:

$$R_o = \left(\frac{3}{4\pi} V_{max} \right)^{\frac{1}{3}}. \tag{4.7}$$

The results of this scaling are shown in Figure 4.19. We see that Tests A1 and A6 work well under the assumptions made. They effectively collapse onto one another for the initial growth and collapse. Their maximum volume is approximately 92% of the predicted value. The discrepancy can be attributed to other energy losses (such as that to due dart impacts with the cavity wall), error in estimating the cavity volume, and time delay effects (i.e. the local cavity radius maxima are not simultaneous across the entire depth). The collapse time predicted using

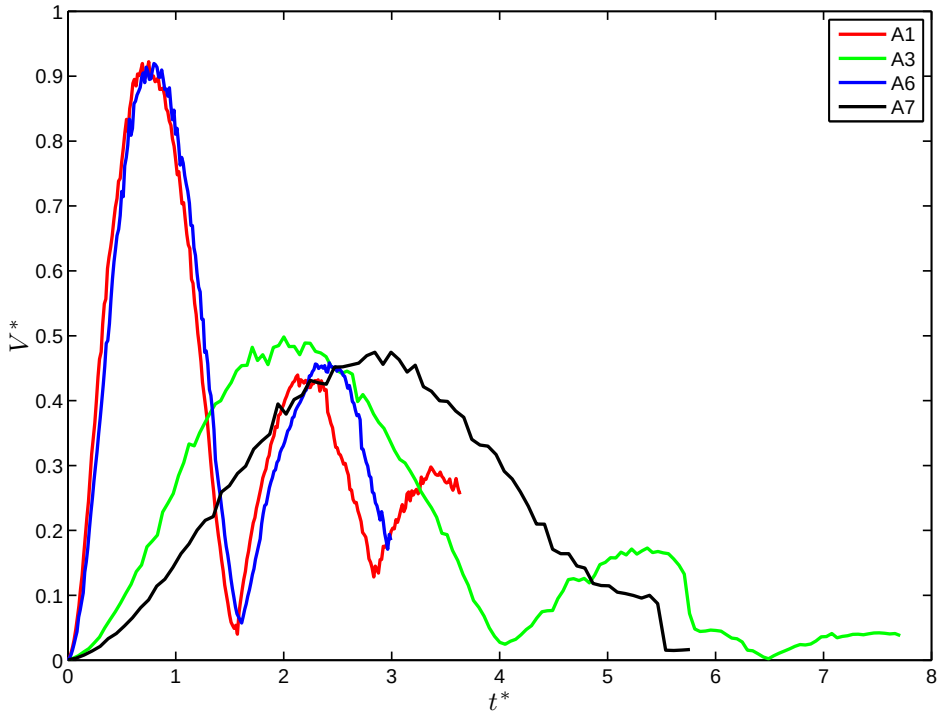

Figure 4.19: Normalized cavity volume histories using Rayleigh's model. Volume is scaled by the maximum value given by an energy balance, $V_{max} = \frac{1}{2} m \frac{v_o^2 - v_f^2}{p_\infty - p_v}$. Time is scaled by the collapse time of an equivalent spherical bubble, $T_c = 0.915 R_o \sqrt{\frac{\rho}{p_\infty - p_v}}$, where R_o is the radius of a sphere with the same maximum volume as was observed experimentally.

equivalent spherical bubble is longer than that seen for these two cases, but is within reason.

The results of scaling for Tests A3 and A7 are not as satisfactory. Their maximum volume is approximately 50% of that predicted by kinetic energy losses. Additionally, the observed collapse time is between two and three times the predicted value. The cause is hypothesized to lie in the differences in the collapse mode. These two tests collapse radially, in a zipper-like fashion, whereas A1 and A6 collapse in the center of the fluid, in a manner more akin to that of a spherical

bubble. In Test A7 in particular, the cavity was collapsing at the apex before the projectile impacted the target plate, meaning there was a large time delay between maximum radii across the entire depth. This is likely the reason that the gross behavior of Tests A1 and A6 seems to scale well with a spherical bubble approximation while A3 and A7 do not.

4.8 Two-Dimensional Modeling

While the previous scaling attempts have provided some insight into the physics behind the behavior of these cavities, they are rudimentary at best. Further understanding can be accomplished by adapting previously-developed physics-based models to the experimental data at hand.

A Rayleigh-like governing equation for the dynamics of an infinitely long cylindrical bubble growing and collapsing in an incompressible fluid can be obtained simply from the Euler equation in cylindrical coordinates. Ignoring azimuthal and axial components this is,

$$\frac{\partial \varphi}{\partial t} + \frac{1}{2}u_r^2 + \frac{p}{\rho} = 0, \tag{4.8}$$

where φ is the velocity potential, and u_r is the radial fluid velocity. Using a kinematic boundary condition at the bubble wall and continuity, these two quantities are given by

$$u_r = \frac{R\dot{R}}{r} \tag{4.9}$$

and

$$\varphi = R\dot{R}\log r. \tag{4.10}$$

Substituting into Equation 4.8 and integrating from the bubble wall, R, where the pressure is p_i, to some far point, S, where the pressure is p_∞, gives

$$\frac{d(R\dot{R})}{dt}\log\frac{R}{S} + \frac{1}{2}\dot{R}^2\left(1 - \frac{R^2}{S^2}\right) + \frac{p_i - p_\infty}{\rho} = 0. \tag{4.11}$$

The logarithmic term in the previous equation presents innate difficulties not present in the Rayleigh equation for a spherical bubble. As the fluid grows large ($S \to \infty$), the only solution is an unmoving cavity wall.

4.8.1 The Lee Model

Lee et al. produced a model to predict the cavities generated by the high-speed water entry of spheres, as discussed in Section 2.2.3 [3]. In dealing with the location of the far-field boundary, S, they followed the precedent of Birkhoff and Zarantanello by setting the ratio of S/R to a constant between 15 and 30 [6].

Figures 4.20 and 4.21 show the results of the Lee model for Test A6. Near the free surface and the target plate, local three-dimensional effects dominate cavity behavior. Errors there are large because this invalidates the fundamental assumption that fluid layers are decoupled. However, the values for maximum radius agree well with experiment through the middle of the volume. This indicates that the energy balance method employed by Lee et al. (as well as other similar models) is an appropriate approach. The time-dependent behavior of the cavities, however, is not as good. The model predicts the early portion of the growth phase well, but ultimately reaches the maximum radius slower than observed experimentally. This same effect is seen in the collapse phase, where the cavity wall velocity is under-predicted, and collapse is predicted to take longer than is observed. These two compound to give a poor estimate of collapse time. The *ad hoc* values used for S control the speed at which the cavity grows and collapses. Choosing these values more wisely allows for an improved model.

4.8.2 The Bergmann Model

Lohse et al. have used the governing equation given by Equation 4.11 to derive a model to predict the dynamics of cavities generated by dropping steel spheres into a fluidic sand bed [14]. Bergmann et al. continued this work, exploring the cavities

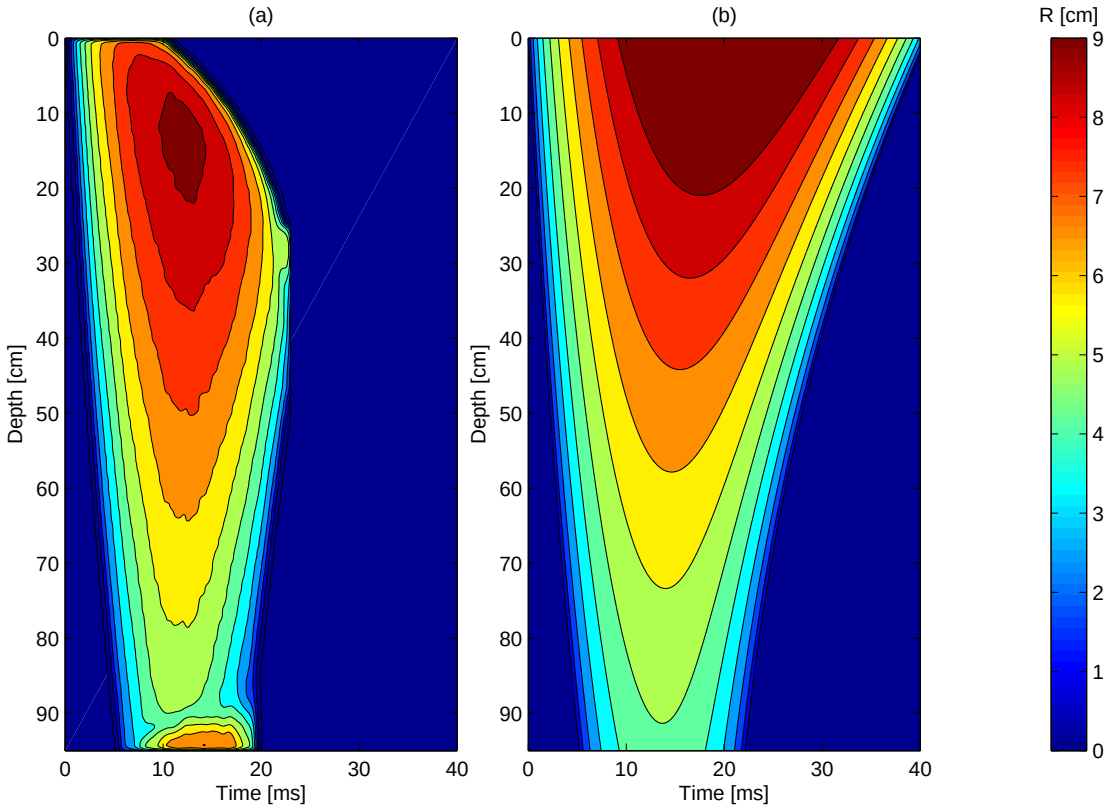

Figure 4.20: Cavity radius contours for Test A6 as a function of time and depth for (a) experimental data, (b) Lee Model using $S/R = 30$.

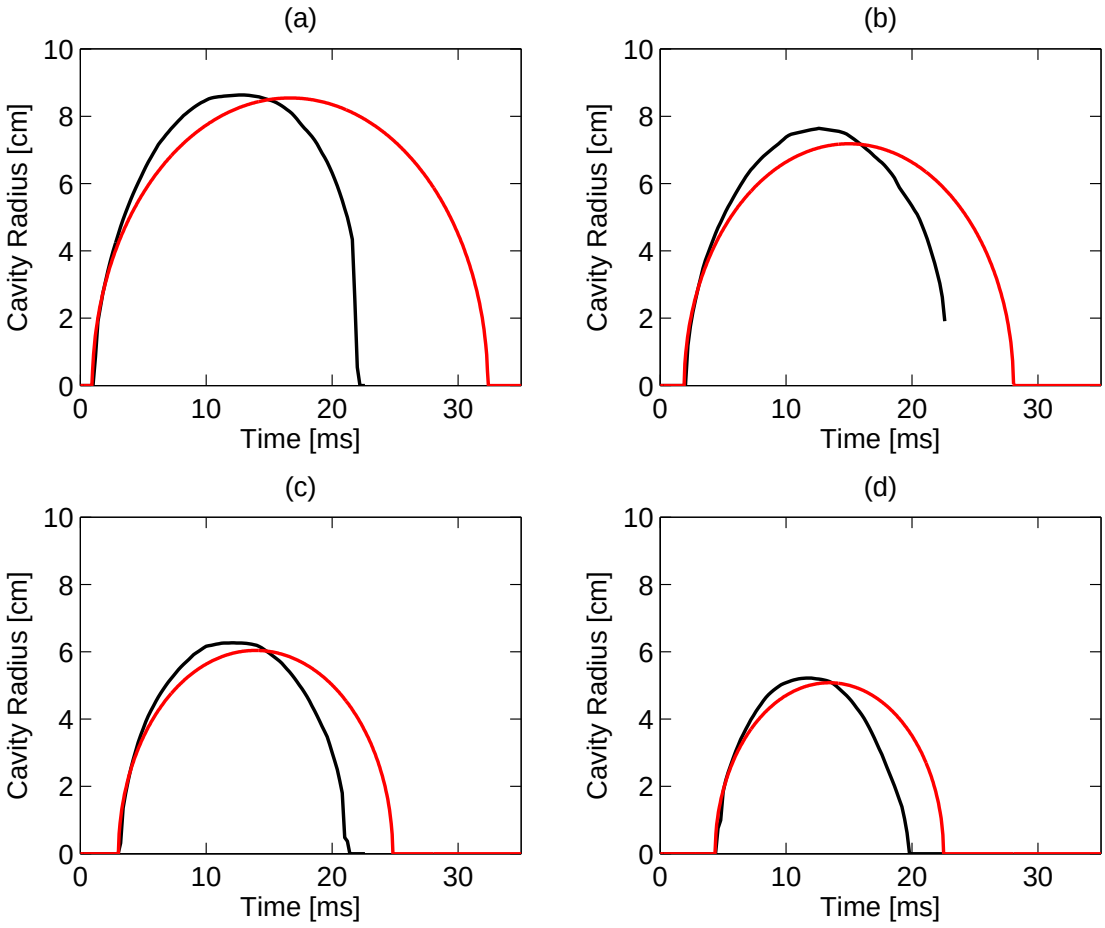

Figure 4.21: Cavity radius histories for Test A6 experimental data (black), and Lee model using $S/R = 30$ (red) at depths of (a) 25 cm, (b) 45 cm, (c) 65 cm and (d) 85 cm.

generated by disks impacting a free surface, as discussed in-depth in Section 2.2.4 [2].

Given Equation 4.11, Bergmann et al. split the dynamics into three regimes: expansion, contraction, and collapse. Expansion is the period of time between the arrival of the disk at a given depth (t_r) and the cavity reaching its maximum radius at that depth (t_m). Contraction is the period between the maximum radius and when the cavity has returned to the radius of the disk (t_x). Collapse is the period in which the cavity collapses from the radius of the disk to zero (t_c).

Dividing the phenomenon into three regimes allows simplifications to be made in each. In the expansion and contraction phases, $\dot{R}$ is assumed to be small enough to be neglected, allowing $\log(R/S)$ to be approximated as a constant,

$$\beta = -\log \frac{R_{max}}{S}, \tag{4.12}$$

where R_{max} is the maximum radius at a given depth. In the collapse phase, the cavity radius approaches zero, causing the logarithmic term to diverge. As a consequence, its pre-factor must be zero, implying that

$$\frac{d(R\dot{R})}{dt} = 0. \tag{4.13}$$

Using these two assumptions, Equation 4.11 can be solved for the three regimes to give

$$R(z,t) = \begin{cases} \sqrt{R_{max}^2 - \frac{\Delta P}{\rho \beta_e}(t-t_m)^2} & \text{for } t_r < t \leq t_m, \\ \sqrt{R_{max}^2 - \frac{\Delta P}{\rho \beta_c}(t-t_m)^2} & \text{for } t_m < t \leq t_x, \\ \sqrt{2v(z)R_o\alpha_c(t_c - t)} & \text{for } t_x < t \leq t_c, \end{cases} \tag{4.14}$$

where ΔP is the driving pressure difference ($\rho g z$ in the case of Bergmann et al.), R_o is the initial cavity radius (taken here to be the cavitator radius, r_p), and α_c is a constant that relates the projectile velocity at t_r, $v(z)$, to the velocity of the cavity wall at t_x.

Of note here is that β is allowed to take different values in the expansion and contraction phases, implying two values of S. This is an improvement over the previous models, where a single, fixed value for S was used across all cases.

4.8.3 Adaptation of the Bergmann Model

The following adaptation of Bergmann's model is presented with an important caveat. Their analysis focused on disks entering the water with Froude numbers of less than 500, while the current work deals with projectiles with Froude numbers in the range of $1{\times}10^6$ and higher. As a result, some values of β used in the following sections are extrapolated. Additionally, the focus in their work was on the dynamics of the cavity only at the pinch point. In this case, we apply the model across the entire cavity length. Warnings aside, the results bear exploration.

Some minor adjustments were made in order to apply the model presented in Equation 4.14 to the previously-shown experimental data. The first is a matter of the driving pressure. The data presented by Bergmann et al. was for relatively low Froude numbers, meaning the cavity pressure was close to ambient atmospheric pressure. For the experiments at hand, the Froude number is several orders of magnitude higher. As a result, the pressure in the cavity is significantly lower than ambient, approaching the vapor pressure of water. So, the pressure difference is given by

$$\Delta P = p_\infty - p_i + \rho g z, \tag{4.15}$$

where p_i is the pressure inside the cavity, in this case 1.7 kPa (the vapor pressure of water at 15°C).

A second consequence of the high Froude number is the relative cavity size. In the data shown by Bergmann et al., the maximum cavity radius was typically on the order of two to three times the disk radius. Here, the cavity radius exceeds ten times the dart tip radius in some cases. As a result, the third regime, in which the cavity collapses from the disk radius to zero, is very short. Going forward, it

is neglected, giving

$$R(z,t) = \begin{cases} \sqrt{R_{max}^2 - \frac{\Delta P}{\rho \beta_e}(t - t_m)^2} & \text{for } t_r < t \leq t_m, \\ \sqrt{R_{max}^2 - \frac{\Delta P}{\rho \beta_c}(t - t_m)^2} & \text{for } t_m < t \leq t_c. \end{cases} \tag{4.16}$$

More information is required in order to use the model described by Equation 4.16. First and foremost, the maximum radius of the cavity as a function of depth needs to be calculated. In this instance, an energy balance is applied, equating the kinetic energy lost by the projectile to the work done against the hydrostatic pressure by the expanding cavity, assuming purely radial motion. The energy lost by a projectile moving through a fluid is

$$\frac{dE_k}{dz} = \frac{1}{2}\rho \left[v(z)\right]^2 C_D A_p, \tag{4.17}$$

where $v(z)$ is the velocity of the projectile as a function of depth, A_p is the frontal area, and C_D is the drag coefficient, assumed to be a constant. In this case, $v(z)$ was calculated using the initial conditions given in Table 4.5. This energy loss is used by the expanding cavity to do work against the pressure difference, given by

$$\frac{dE_b}{dz} = \pi \Delta P R_{max}^2(z), \tag{4.18}$$

where ΔP is given by Equation 4.15. Combining Equations 4.17 and 4.18, an expression for the maximum radius as a function of depth is given as

$$R_{max}(z) = \sqrt{\frac{\rho \left[v(z)\right]^2 C_D A_p}{2\pi \Delta P}}. \tag{4.19}$$

Additionally, the time the cavity reaches its maximum at a given depth needs to be calculated in order to demarcate the expansion and contraction phases of the model. This can be obtained with the first half of Equation 4.16, where it is known that at time t_r, the cavity radius is the same as the radius of the nose of the projectile, r_p. Solving for t_m yields

$$t_m = t_r + \sqrt{\frac{\left(R_{max}^2 - r_p^2\right)\rho \beta_e}{\Delta P}}. \tag{4.20}$$

Calculating β_e and β_c

The final pieces of information needed to complete this model are values for β_e and β_c, which correlate to the amount of fluid influenced by the motion of the cavity. The values calculated for Bergmann et al. were for effectively-infinite domains — their cavity is unaffected by the domain size and is limited instead by the axially-coupled flow in the vicinity of the cavity wall. As the Froude number is increased, however, one can expect that the cavities will tend closer to a quasi-one-dimensional geometry of a cylindrical bubble, and hence may anticipate this effect to be diminished. Additionally, for the current work there is the possibility that the finite size of the tank or compressibility effects may act as a constraint to limit the bubble collapse time, offering alternative mechanisms to be explored. As a result, we consider two potential values of β: those extrapolated from the data of Bergmann et al. to estimate values for the axially-coupled case and those determined by the amount of fluid present (i.e. the size of the experimental tank).

At the conclusion of their work, Bergmann and Lohse present plots of β as a function of Froude number. This data is reproduced in Figure 4.22. The data show an approximately linear trend of β with the logarithm of Froude number for values greater than 100. Extrapolation yields estimated values for β. Given some evidence of insensitivity to Froude number, this may be imprudent, but for the purposes of this work, it serves to facilitate discussion of volume-limited cavity dynamics. Figure 4.23 shows values for β_e and β_c calculated via extrapolation as a function of depth for model results for the four experimental tests.

The alternative is to calculate β using some physical parameter of the experiment. To gage the effects of confinement due to a small tank, values of β corresponding to the hydraulic radius of the tank were calculated. Figure 4.23 shows curves of β using this assumption. Note here that

$$\beta_{rh} = -\log \frac{R_{max}(z)}{R_h}, \tag{4.21}$$

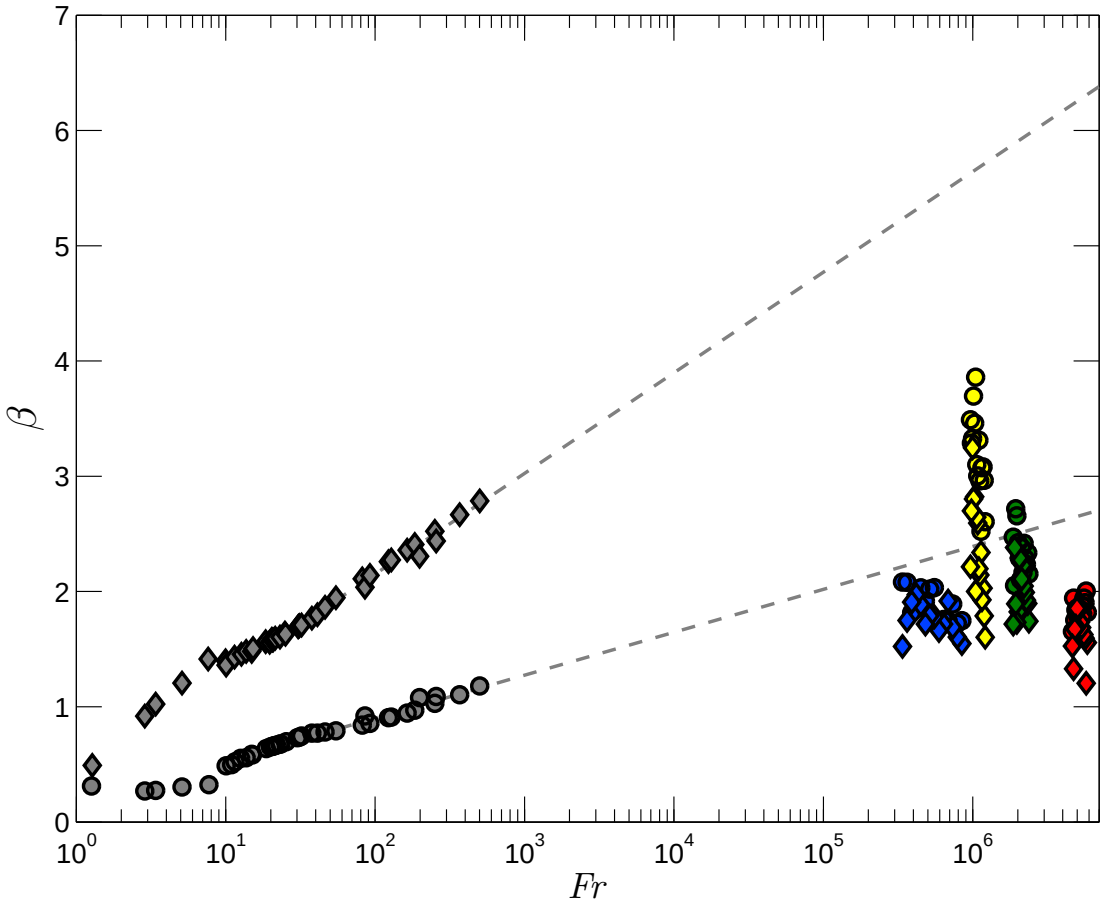

Figure 4.22: Values for β_e (circles) and β_c (diamonds). Data reproduced from [2] are shown with solid symbols. Extrapolation of this data for Froude number greater than 500 is shown with dashed lines. Values fit to experimental data are shown with colored symbols: Test A1 is red, Test A3 is green, Test A6 is blue, Test A7 is yellow.

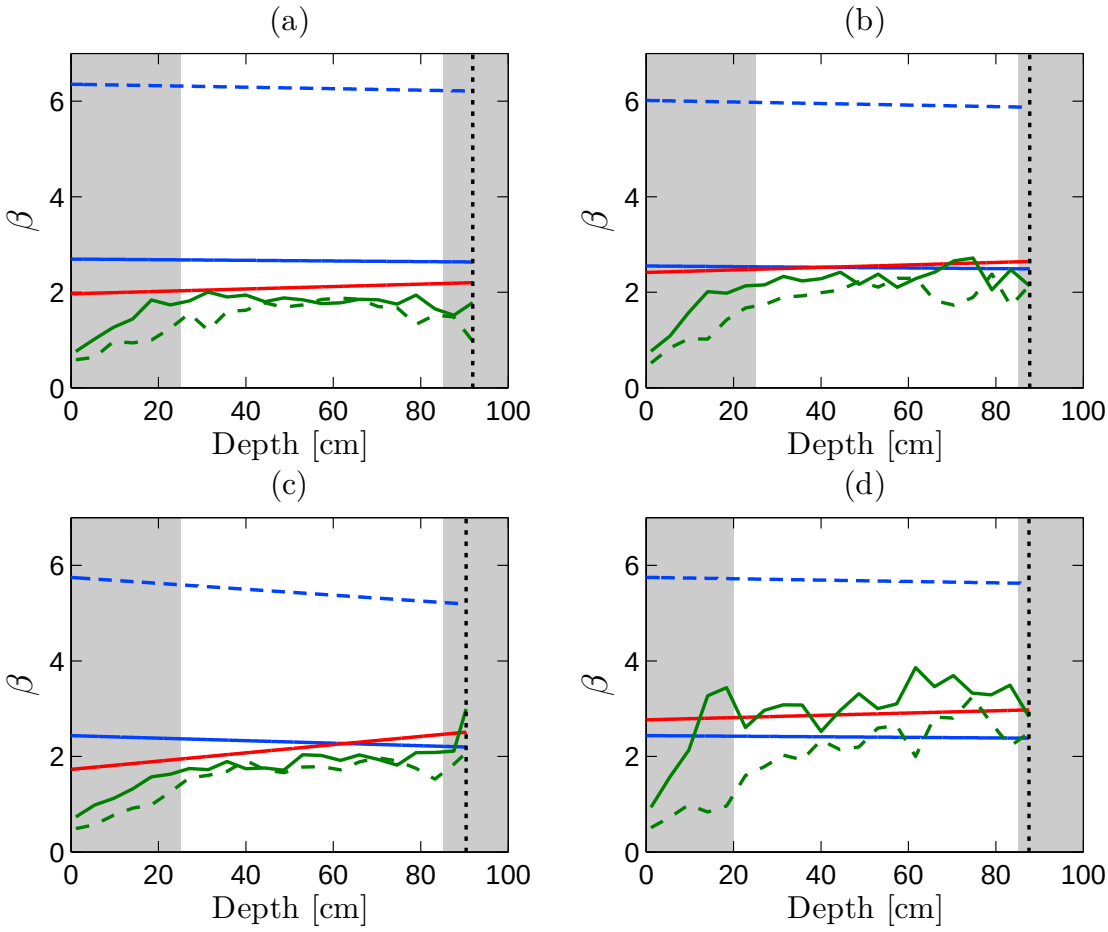

Figure 4.23: Values of β extrapolated from data by Bergmann et al. [2] (blue) and from calculated via experimental hydraulic diameter, β_{rh} (red) for (a) Test A1, (b) Test A3, (c) Test A6 and (d) Test A7. Values of β_e are shown with solid lines. β_c is shown with dashed lines. For our model, the minimum value of β and β_{rh} will be used in the expansion and collapse phases. Values fit to experimental data (green) are shown for comparison. Experimental tank bottom is marked with a vertical dotted line. Regions where the cavity behavior appears to be influenced by local three-dimensional effects are gray.

where R_h is the hydraulic radius, given by

$$R_h = \frac{2A_t}{P_t}, \tag{4.22}$$

where A_t is the area of the tank and P_t is the perimeter. In this case, the tank was approximately 120 cm square, giving a hydraulic radius of 60 cm.

Smaller values of β correspond to a smaller amount of fluid influenced. When the value of β calculated via the hydraulic radius is smaller than the extrapolated values, the behavior of the cavity is either acoustically-limited or limited by the size of the tank. When the opposite is true, the cavity is behaving as if it were in an infinite fluid. In light of this, when evaluating the adapted model, the smaller of the two values is used. As a result, for the experimental work presented, the model nearly always takes β as the value given by the hydraulic radius, as seen in Figure 4.23. The work presented by Bergmann et al. [2] had values of β_{rh} on the order of 3 for their highest Froude number tests. This is larger than their greatest value of β, suggesting that their cavities were not influenced by the size of their tank.

Values for β can also be estimated from the experimental data. A least-squares fit of Equation 4.16 is shown with model results in Figure 4.26 through Figure 4.32. The resulting values for β are shown with values from Bergmann et al. [2] in Figure 4.22 and compared to calculated values in Figure 4.23. Regions where local three-dimensional effects (e.g. surface seal) appear to affect the cavity behavior are gray in Figure 4.23 and excluded from Figure 4.22. The only input to the least-squares fit are the radius-time histories (including values for R_{max} and t_m) from the fixed-space data set. The values for β_e and β_c are similar to those calculated via the hydraulic radius. This implies that the size of the tank may have played a role in determining the cavity dynamics. Additionally, the results of this fit show symmetry in the growth and collapse phases ($\beta_e \sim \beta_c$), which is not predicted by the trends of the data from Bergmann et al. [2] shown in Figure 4.22.

4.8.4 Comparison of Model to Experimental Data

Using only the initial conditions given in Table 4.5, maximum cavity radii as a function of depth can be calculated. This quantity is compared with the experimentally-observed values in Figure 4.24. In this case, the cavity pressure was assumed to be 1.7 kPa, the vapor pressure of water at 15°C.

For all cases, the error is large near the free surface. Here the splash crated by water entry domes over and seals the cavity, modifying behavior in this region. At the bottom surface, the target plate introduces further local three-dimensional effects, as the cavity forms a small "foot" near the impact site, increasing errors in this area. These regions will be excluded from further discussion.

Despite the discrepancy at the upper and lower boundaries of the tank, the maximum radius of the cavity is predicted quite well at intermediate depths. Here, Test A1 shows the greatest error, over-predicting consistently by approximately 6%. This is likely due to energy lost to the cavity impact observed in this case, shown in Figure 4.11. Test A3 agrees well nearer the free surface, with errors of about 1%. Approaching the bottom, this error grows to 4%. Test A6 shows error ranging from near zero to 5%. Test A7 shows the best agreement with experiment, with errors below 1% away from the free surface and target plate.

Figures 4.25 through 4.32 show the experimental data compared to results of Equation 4.16. All figures show results for the baseline model using values estimated via extrapolation of data from Bergmann et al. [2] compared to results of the adapted model, where the effect of hydraulic radius on β is considered.

Figures 4.25 and 4.26 show model results compared to experiment for Test A1. During the growth phase, both models are nearly identical, with errors of approximately 5%. In the collapse phase, however, considering the effect of hydraulic radius improves the results, predicting collapse time within 7%. This agreement would be improved by a better prediction of the maximum cavity radius.

Figures 4.27 and 4.28 show the results for Test A3. Both versions of the model

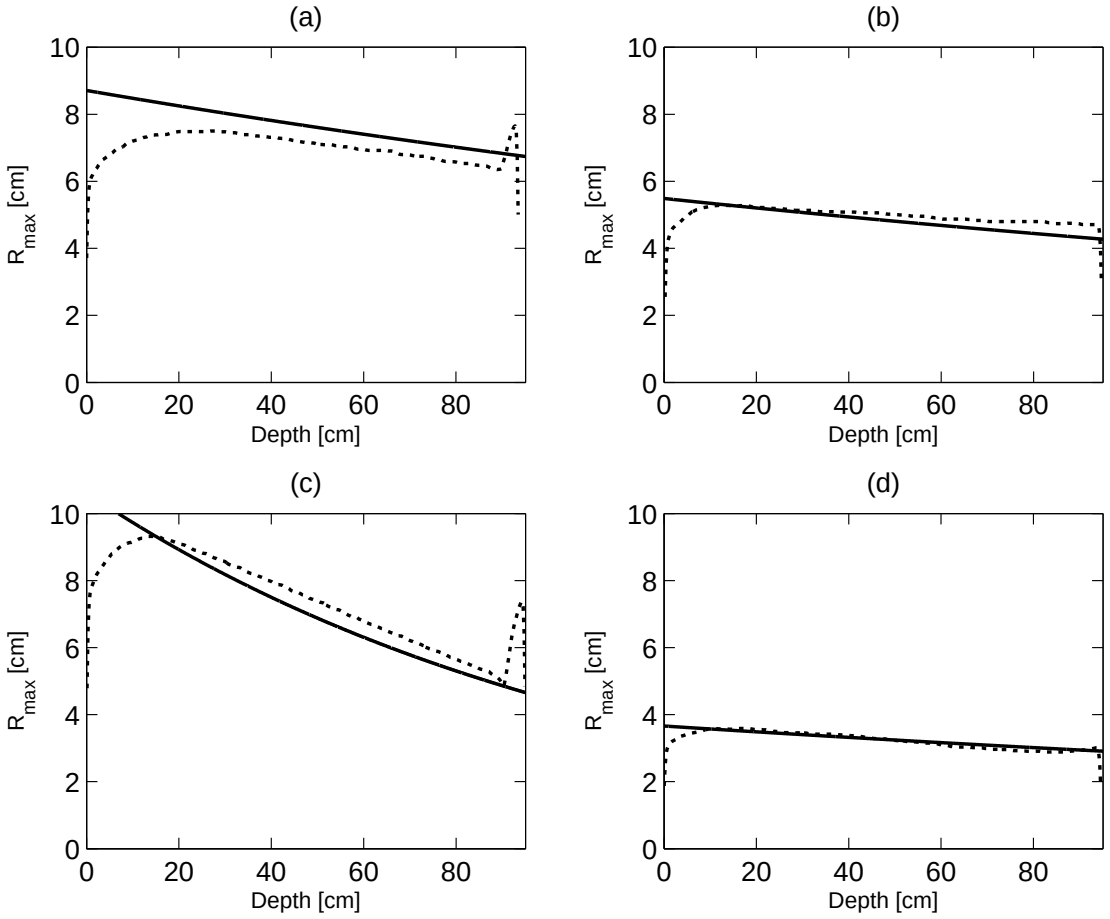

Figure 4.24: Maximum cavity radius calculated with Equation 4.19 (solid lines) compared with experimentally-observed values (dotted lines) for (a) Test A1, (b) Test A3, (c) Test A6, and (d) Test A7.

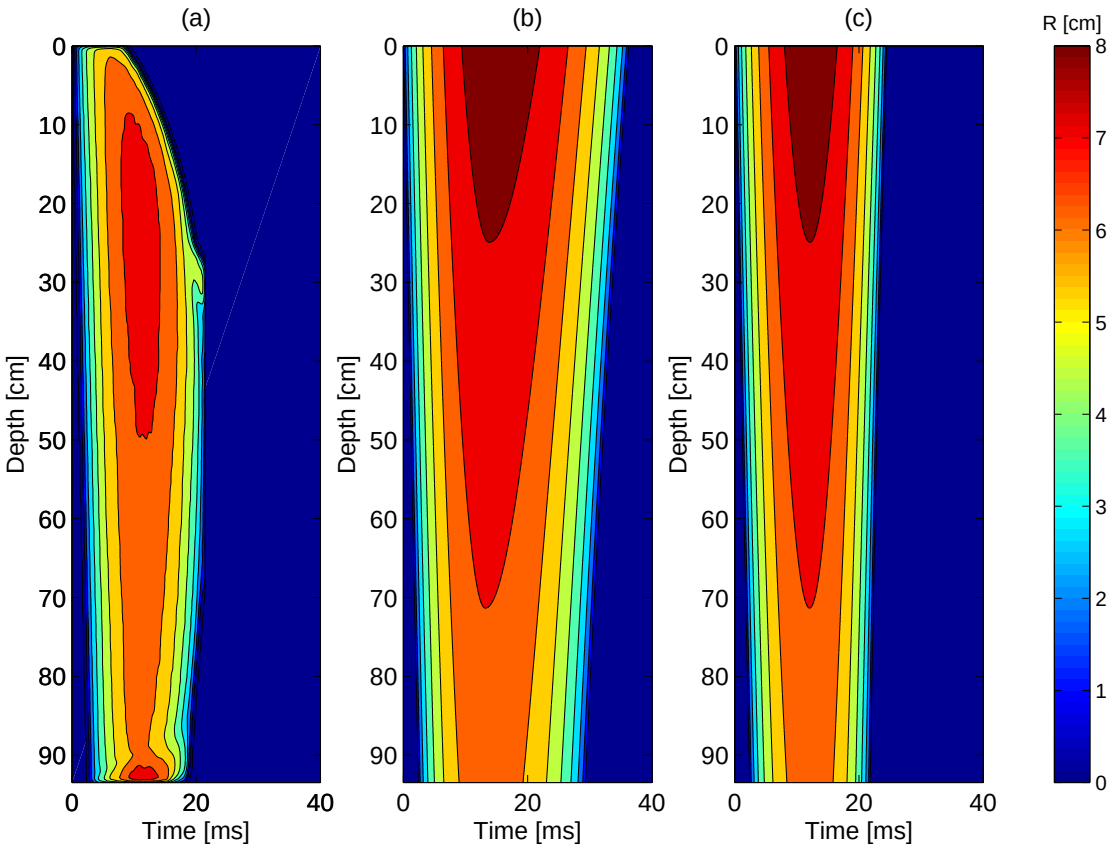

Figure 4.25: Cavity radius contours for Test A1 as a function of time and depth for (a) experimental data, (b) model using extrapolated values for β_e and β_c, and (c) model using tank hydraulic radius to set β.

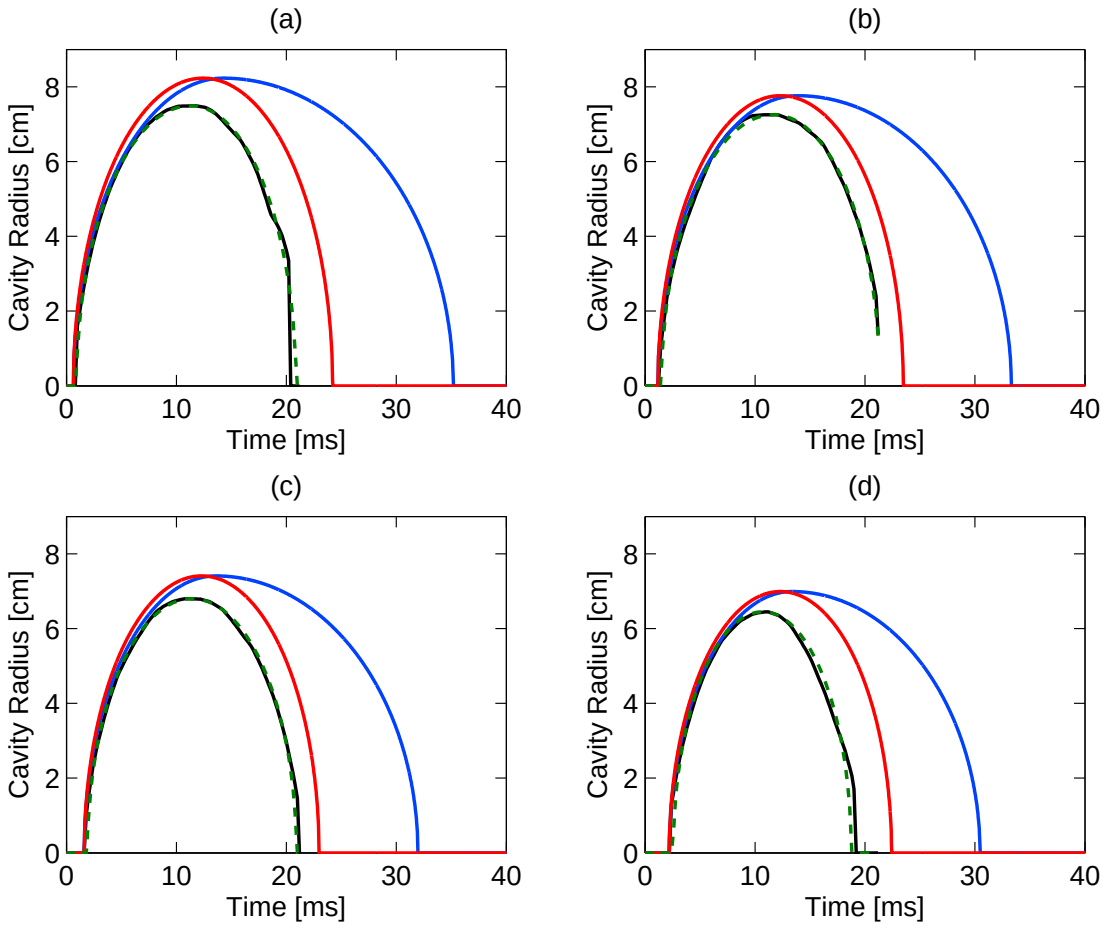

Figure 4.26: Cavity radius histories for Test A1. Experimental data is shown in black. The model using extrapolated values for β_e and β_c is shown in blue. The model using tank hydraulic radius to set β is shown in red. Least-squared fit of experimental data to Equation 4.16 is shown in green. Slices are taken at depths of (a) 25 cm, (b) 45 cm, (c) 65 cm, and (d) 85 cm.

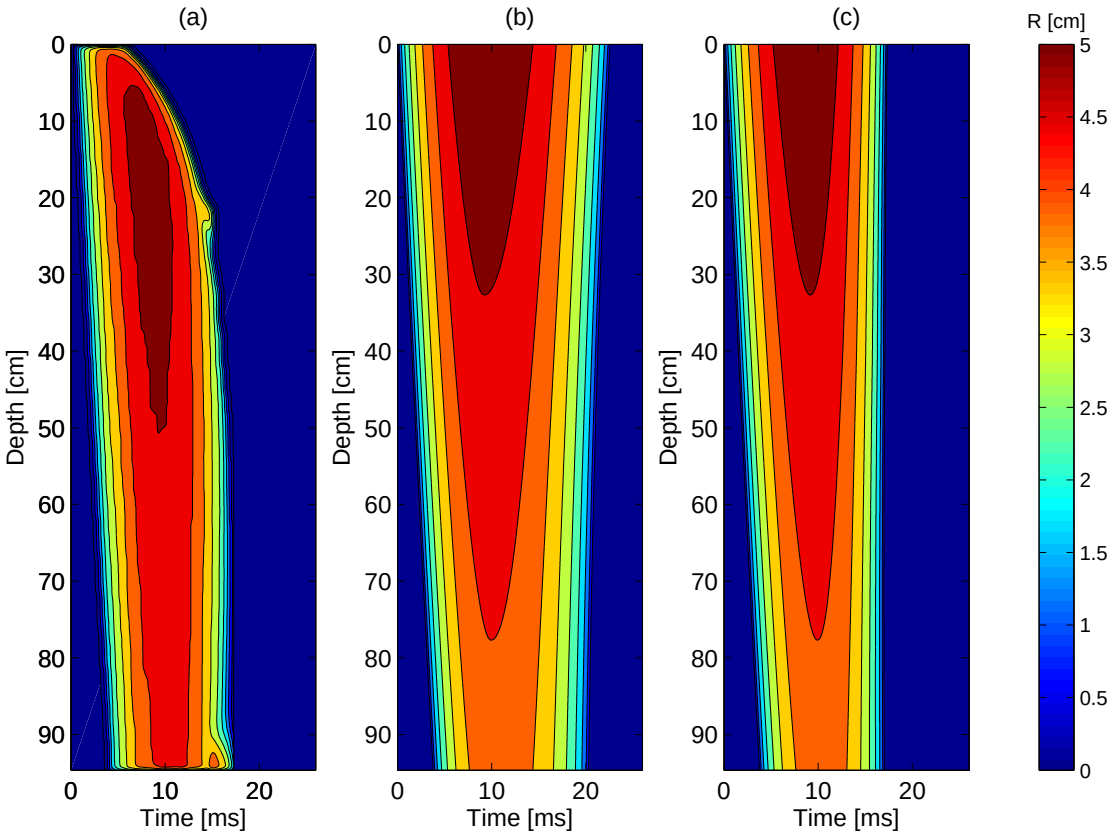

Figure 4.27: Cavity radius contours for Test A3 as a function of time and depth for (a) experimental data, (b) model using extrapolated values for β_e and β_c, and (c) model using tank hydraulic radius to set β.

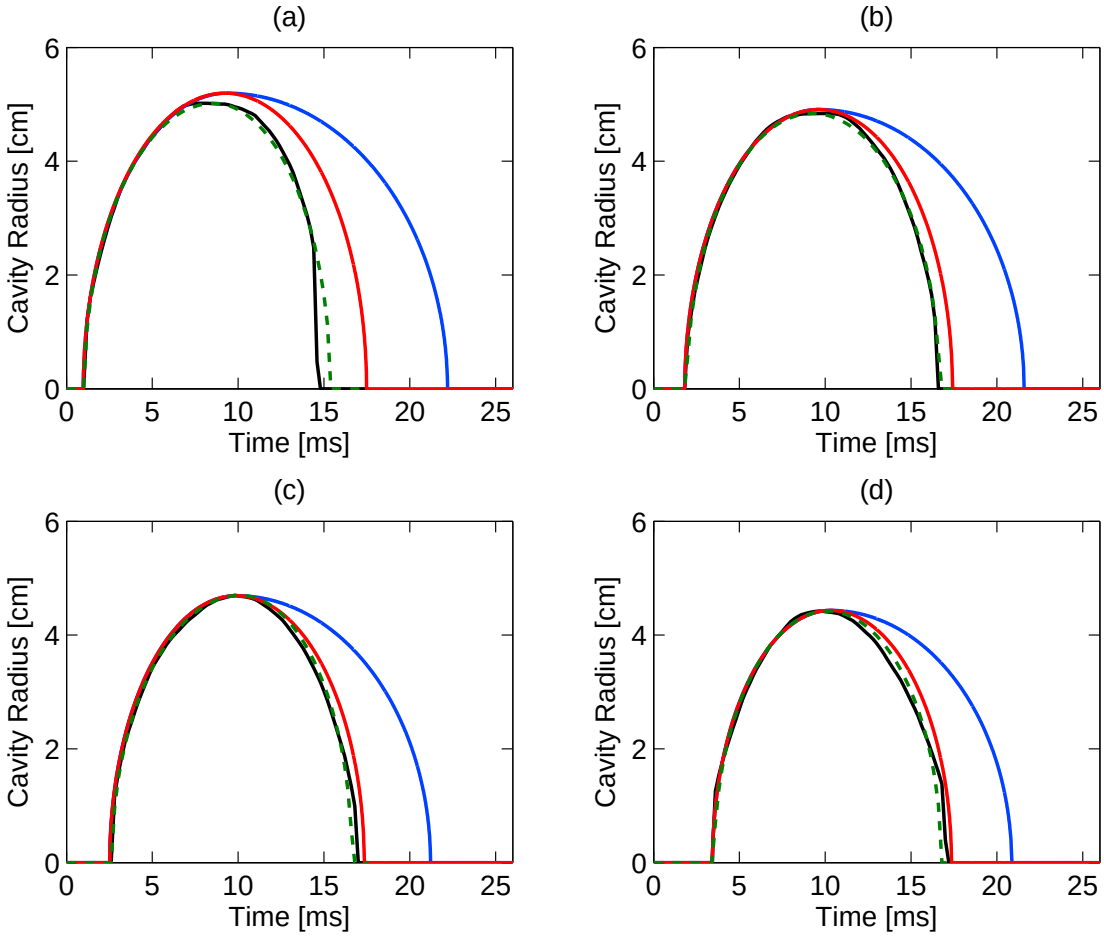

Figure 4.28: Cavity radius histories for Test A3. Experimental data is shown in black. The model using extrapolated values for β_e and β_c is shown in blue. The model using tank hydraulic radius to set β is shown in red. Least-squared fit of experimental data to Equation 4.16 is shown in green. Slices are taken at depths of (a) 25 cm, (b) 45 cm, (c) 65 cm, and (d) 85 cm.

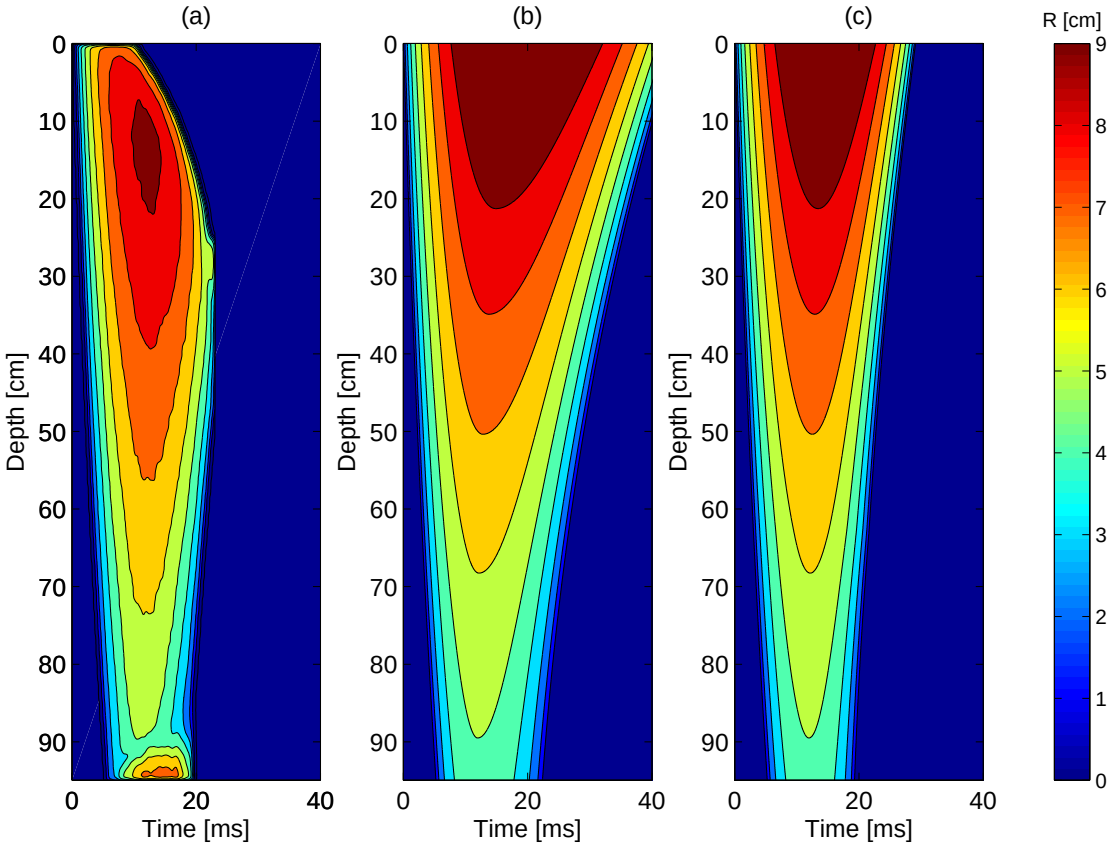

Figure 4.29: Cavity radius contours for Test A6 as a function of time and depth for (a) experimental data, (b) model using extrapolated values for β_e and β_c, and (c) model using tank hydraulic radius to set β.

predict the growth phase well, because they share similar values for β_e, as shown in Figure 4.23. Again, our adjustment including the effect of hydraulic radius outperforms the baseline model in predicting the collapse time, with errors ranging from 10% at a depth of 25 cm, to as small as 3% at a depth of 45 cm.

Figures 4.29 and 4.30 show the results of both models for Test A6 compared to experimental values. Again, as both versions of the model take similar values for β_e through most of the depth, they show similar good agreement with experiment in predicting the growth phase. Away from the free surface, our model better matches the collapse phase, predicting the collapse time within 2%.

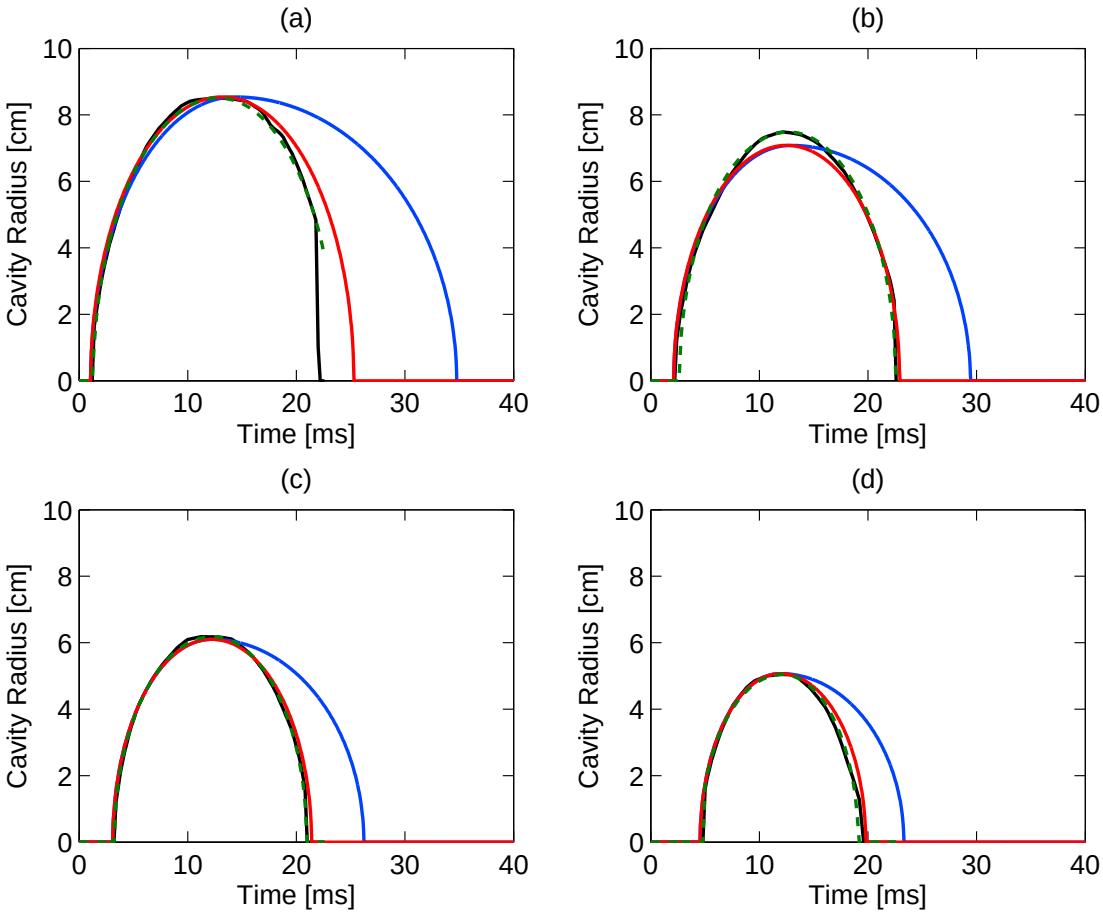

Figure 4.30: Cavity radius histories for Test A6. Experimental data is shown in black. The model using extrapolated values for β_e and β_c is shown in blue. The model using tank hydraulic radius to set β is shown in red. Least-squared fit of experimental data to Equation 4.16 is shown in green. Slices are taken at depths of (a) 25 cm, (b) 45 cm, (c) 65 cm, and (d) 85 cm.

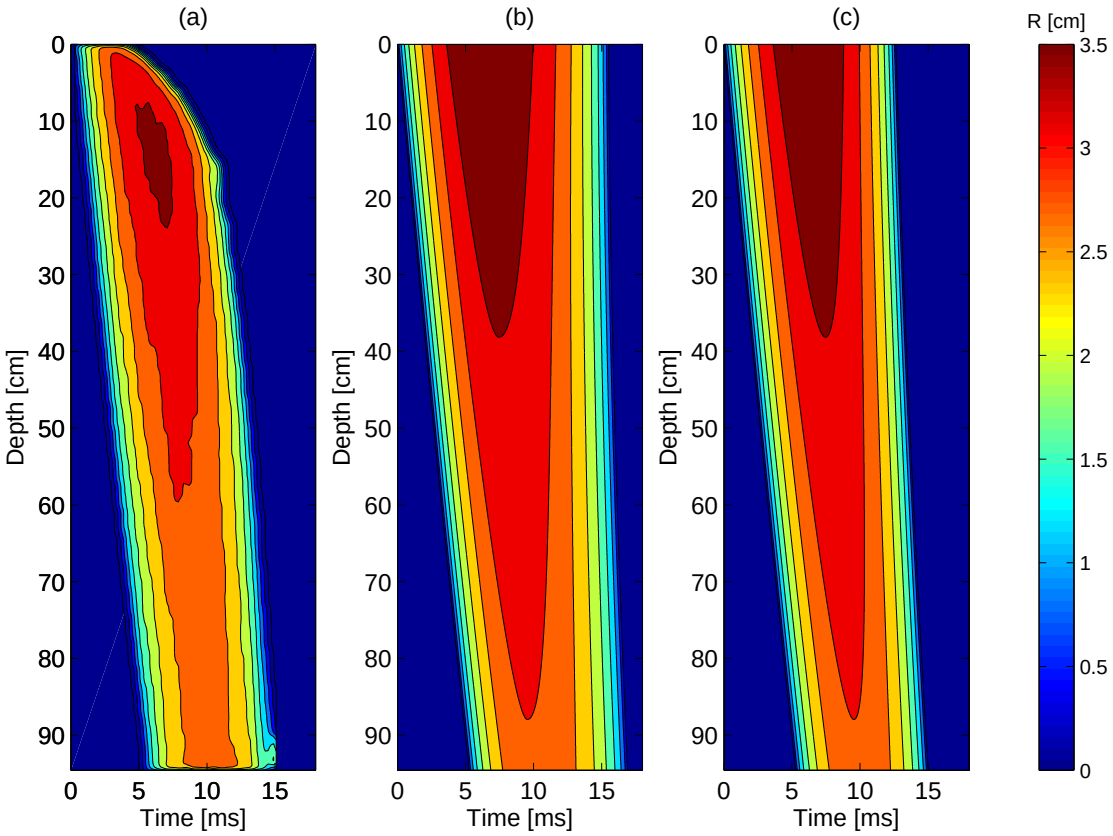

Figure 4.31: Cavity radius contours for Test A7 as a function of time and depth for (a) experimental data, (b) model using extrapolated values for β_e and β_c, and (c) model using tank hydraulic radius to set β.

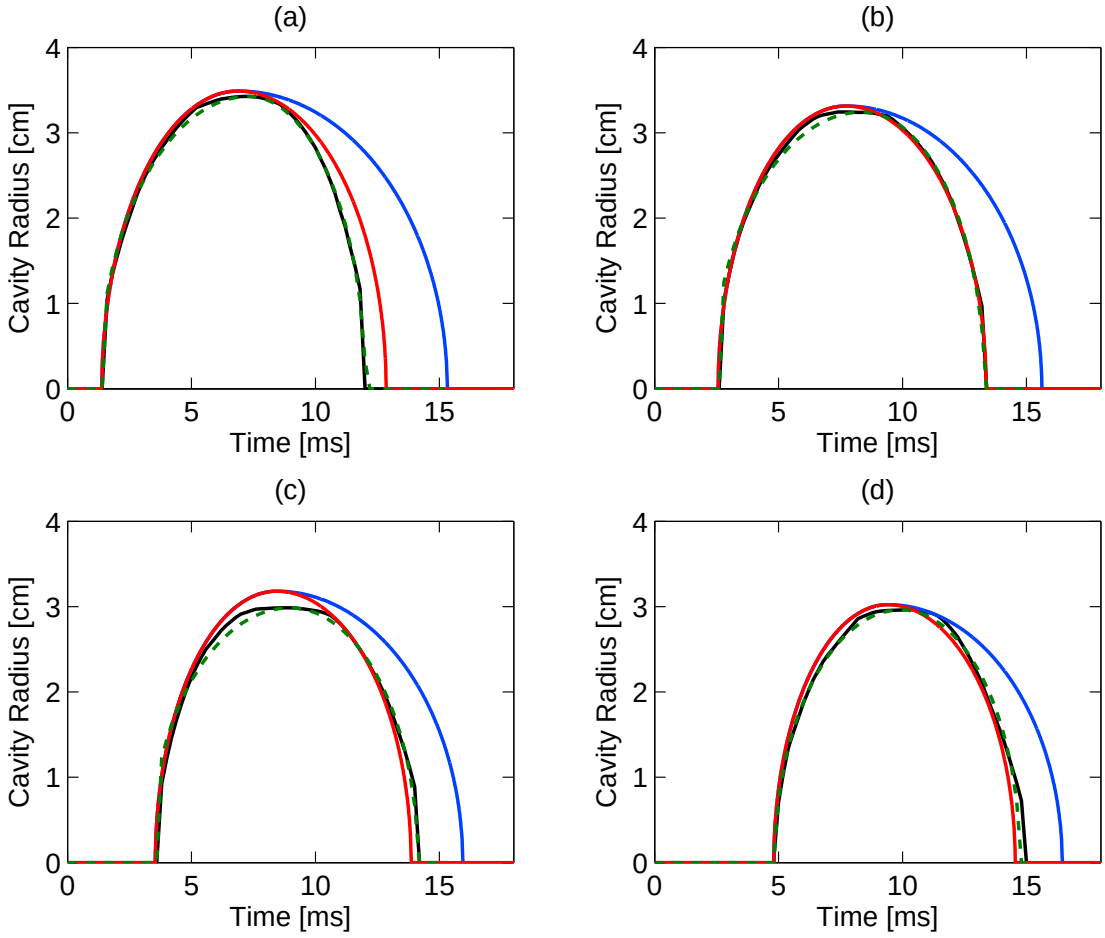

Figure 4.32: Cavity radius histories for Test A7. Experimental data is shown in black. The model using extrapolated values for β_e and β_c is shown in blue. The model using tank hydraulic radius to set β is shown in red. Least-squared fit of experimental data to Equation 4.16 is shown in green. Slices are taken at depths of (a) 25 cm, (b) 45 cm, (c) 65 cm, and (d) 85 cm.

Figures 4.31 and 4.32 show model predictions for Test A7. Because both versions of the model again have the same values for β_e, they agree well with experiment during the expansion phase away from the free surface. The extrapolated values for β_c, however, lead to an over-prediction of local collapse time by about 20%. Using the hydraulic radius value, β_{rh}, for the contraction phase leads to agreement within a few percent of the experimental value of local collapse time.

Verifying Cavity Pressure

The errors in calculating values for R_{max} propagate through the model, degrading results for some cases (e.g. Test A1). Inspecting Equation 4.19, one unknown is the cavity pressure, p_i, which controls the driving pressure, ΔP.

Using the experimentally-observed maximum cavity radii, approximate values of p_i can be calculated by solving Equation 4.19 for ΔP, yielding

$$\Delta P = \frac{\rho \left[v(z)\right]^2 C_D A_p}{2\pi R_{max}^2}, \tag{4.23}$$

where $\Delta P = P_{atm} + \rho g z - p_i$.

Figure 4.33 shows these calculated values compared with the vapor pressure of 1.7 kPa for water at 15°C. As expected, cases with good agreement for R_{max} show good agreement for ΔP. Additional data points shown on Figures 4.33a,c are estimated mean cavity pressures taken from transducers when they were visibly entrained by the cavity. No transducers entered the cavity for Tests A3 and A7. These two tests show some agreement with our assumed value of 1.7 kPa. Without measured cavity pressures, little else can be said about these two cases.

The calculated absolute cavity pressures for Test A1 are below zero. This is in disagreement with the measured mean cavity pressures, which are in the vicinity of our assumed value of the vapor pressure. This suggests that it is some other factor (e.g. impact with the cavity wall, as demonstrated in Figure 4.11) that is the primary cause of the over-prediction of the maximum radius in this case.

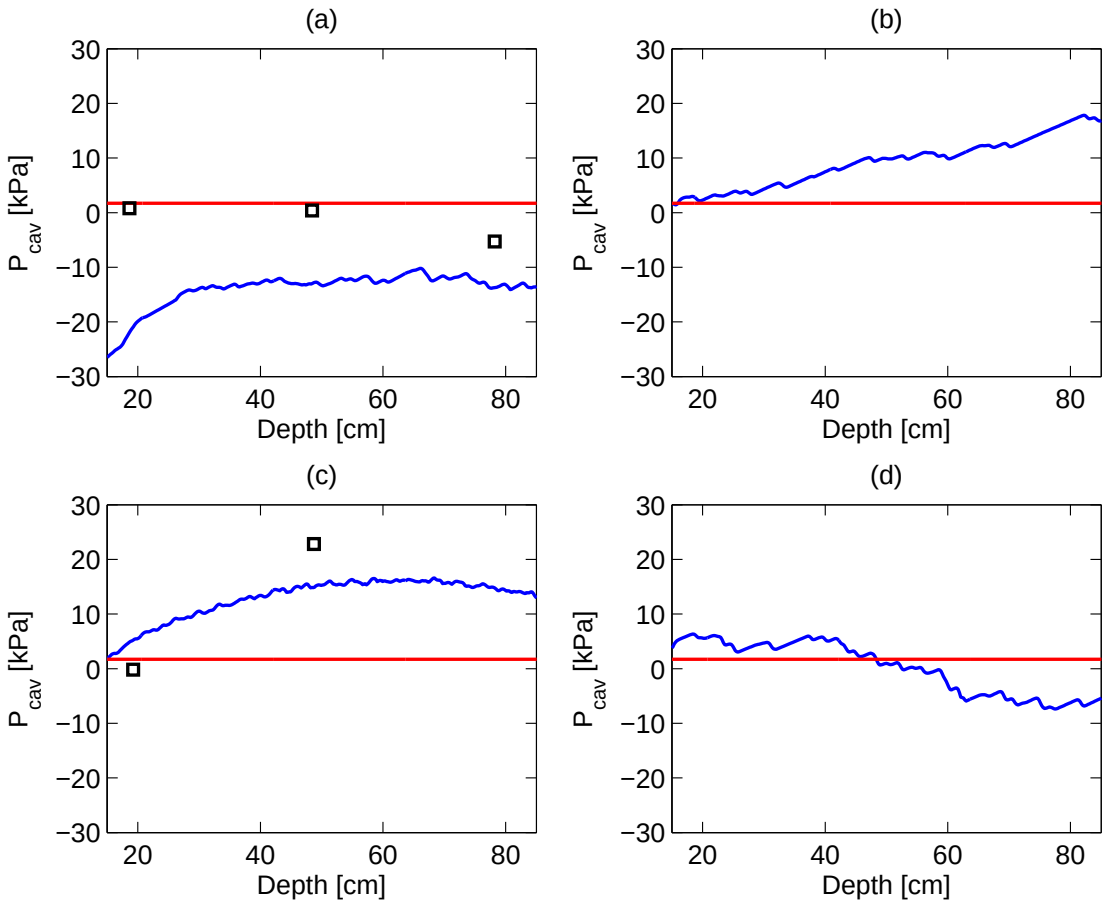

Figure 4.33: Experimentally inferred cavity pressures (blue) compared with vapor pressure of water at 15 °C for (a) Test A1, (b) Test A3, (c) Test A6, and (d) Test A7. Mean measured cavity pressures are marked with squares where experimental data is available.

The values measured and calculated for Test A6 suggest that this case might be better modeled using a non-uniform cavity pressure, as the pressure appears to increase with depth. It is hypothesized that, due to the large dart tip diameter, a significant amount of air was entrained in the cavity, increasing the cavity pressure in late time as the air is compressed.

Table 4.6: Comparison of gross cavity behavior between models for the expansion phase of all cases. Volume is measured between 25 and 85 cm depth. The quantity T_m is the time that the cavity reaches its maximum volume, V_{max}. Errors for these quantities are measured in percent relative to the observed value.

T_m – Time to Maximum Volume

	A1		A3		A6		A7	
	[ms]	[%]	[ms]	[%]	[ms]	[%]	[ms]	[%]
Experiment	12.0	—	9.7	—	12.6	—	7.7	—
Model	12.3	2.7	9.7	0.2	12.5	-1.0	8.1	5.0
Bergmann	13.9	15.5	9.8	1.6	13.1	3.8	8.3	7.6
Lee	15.4	28.1	11.0	13.4	15.0	19.2	9.0	16.6

V_{max} – Cavity Maximum Volume

	A1		A3		A6		A7	
	[m^3]	[%]	[m^3]	[%]	[m^3]	[%]	[m^3]	[%]
Experiment	9.31e-03	—	4.62e-03	—	9.64e-03	—	1.84e-03	—
Model	11.0e-03	18.6	4.41e-03	-4.6	8.87e-03	-8.0	1.98e-03	7.6
Bergmann	11.0e-03	18.5	4.42e-03	-4.5	8.85e-03	-8.2	1.99e-03	8.2
Lee	11.0e-03	18.5	4.42e-03	-4.5	8.82e-03	-8.5	1.99e-03	8.2

Gross Cavity Behavior

Total cavity volume histories can be used to gage the overall performance of the models versus the observed data. Figure 4.34 shows a comparison of the model results for the four test cases presented. Results of this comparison are presented in Tables 4.6 and 4.7. Table 4.6 shows predicted and observed values for the maximum volume and the time at which it occurs, V_{max} and T_m. Table 4.7 offers a similar comparison for the collapse time, T_c, as well as RMS errors for the growth and initial collapse of the cavities, V_{rms}.

It is important to note here that these volume histories neglect regions where the cavity is experiencing boundary effects. This allows us to consider the model

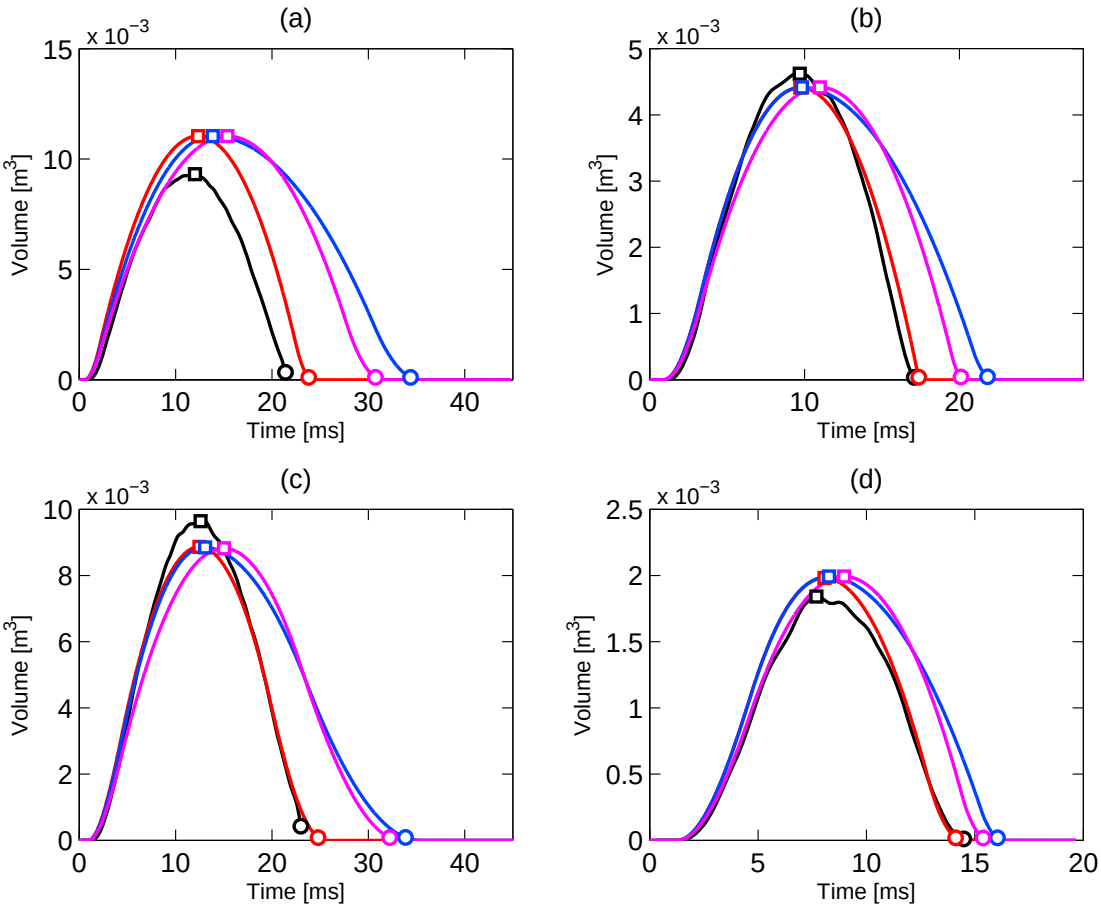

Figure 4.34: Overall volume histories for experiment (black) compared to model results using hydraulic radius to set β (red), model results using extrapolation to set β (blue) and results of model from Lee et al. [3] (magenta) for (a) Test A1, (b) Test A3, (c) Test A6, and (d) Test A7. Values for T_m and T_c are marked with squares and circles, respectively. Volumes for both are measured for depths between 25 and 85 cm.

Table 4.7: Comparison of gross cavity behavior between models for all cases. Volume is measured between 25 and 85 cm depth. The cavity volume reaches its first minimum at T_c. Errors is measured in percent relative to the observed value. The RMS error in volume, V_{rms}, is measured for the initial growth and collapse of the cavity. The normalized value is reported as a percentage of the observed maximum value.

T_c – Time to First Cavity Collapse

	A1		A3		A6		A7	
	[ms]	[%]	[ms]	[%]	[ms]	[%]	[ms]	[%]
Experiment	21.4	—	17.1	—	23.0	—	14.5	—
Model	23.8	11.2	17.4	1.7	24.8	7.9	14.1	-2.4
Bergmann	34.4	60.6	21.8	27.7	33.9	47.2	16.0	10.7
Lee	30.9	43.6	20.1	17.7	32.2	40.1	15.4	6.1

V_{rms} – Cavity Volume RMS Error

	A1		A3		A6		A7	
	[m^3]	[%]	[m^3]	[%]	[m^3]	[%]	[m^3]	[%]
Model	1.45e-03	15.5	1.46e-04	3.3	2.93e-04	3.0	6.56e-05	3.6
Bergmann	3.67e-03	39.4	7.19e-04	15.6	1.65e-03	17.1	2.03e-04	11.0
Lee	4.08e-03	43.9	2.32e-03	50.1	1.06e-03	11.0	1.20e-03	65.2

performance in the where the flow is primarily radial. In this case, this means that the volume is measured in the center region of the fluid, away from both the free and bottom surfaces. The data shown here uses the portion of the cavity between 25 and 85 cm depth.

The results for the maximum volume, V_{max}, show errors for all models in the range of 3 to 15%. There is little variation between models, less than 1% of the total volume. This is not surprising as all three models considered use the same energy balance principle to calculate the maximum cavity radius at a given depth. The slight variations are caused by the disagreements in the calculation of the time to maximum cavity volume, T_m.

When calculating the value of T_m, both the current adaptation and the baseline Bergmann model offer improvements over the Lee model with errors in the range of 0 to 5%, as compared to 2 to 30%. Our adaptation and the baseline Bergmann model offer similar results here because they are using similar, if not exactly identical, values for β_e, as was shown previously in Figure 4.23.

Our adaptation deviates from the other two chiefly in its selection of β_c. The results shown in Table 4.7 show the improvement gained from using a value of β based on the hydraulic radius of the tank. Our predicted collapse time shows errors between 2 and 11%, while the other two models have errors ranging from 6 to 60%.

The RMS errors shown in Table 4.7 demonstrate the overall improvement in accuracy yielded by considering finite-volume effects. Tests A3, A6, and A7 have RMS errors of approximately 3%, as compared to 10 to 47%, reflecting better agreement for both cavity radii and overall timing. Test A1 does not fare as well. However, as discussed previously, video evidence suggests that the tail dragged against the cavity walls, which would cause kinetic energy loss without increasing cavity radius.

4.9 Model Trends

4.9.1 Effect of Projectile Parameters

Given that the model agrees reasonably well with the available experimental data, it can be used to further explore the parameter space. To this end, the model was evaluated for initial velocities ranging from 50 to 450 m/s, with cavitator radii between 1 mm and 10 mm, for projectile masses of 27.5 g, 55 g, and 110 g. The drag coefficient for the projectile was assumed to be 0.80 for all cases [35]. The water depth was set to 100 cm. The hydraulic radius was set to 60 cm in agreement the available experimental data.

Four quantities were calculated for each model configuration. The first two are cavity pinch depth (z_p) and pinch time (T_p). This is the time and location at which the cavity first collapses locally. It is the minimum value of the local collapse time, t_c, given by

$$t_c = t_r + \sqrt{\frac{\rho}{\Delta P}\left[R_{max}^2\left(\beta_e + \beta_c\right) - r_p^2\beta_e\right]}, \tag{4.24}$$

where t_r is the time the projectile reaches a given depth, and R_{max} is the maximum radius at that depth. Figures 4.35 and 4.36 show the cavity pinch time and pinch depth, respectively, for all three masses. Blue contours represent cases where the cavity pinched off at the free surface ($z_p = 0$ m). Red contours represent cases where the cavity pinched at the bottom surface ($z_p = 1$ m). All three values for projectile mass show a gradual transition from pinching off at the free surface to pinching off at the bottom with increasing velocity for a given cavitator radius. At the upper end of this range of radii, masses of 27.5 g and 55 g display a fan behavior where the transition from pinching at the top to pinching at the bottom broadens. This transition is demonstrated in Figure 4.37 for a projectile mass of 55 g. For larger cavitator radii, the projectile is dramatically decelerated, causing extremely tapered cavities that pinch off shortly after the projectile passes (i.e. $T_p \sim t_r(z_p)$).

For radius-mass combinations where this fan is especially pronounced (for ex-

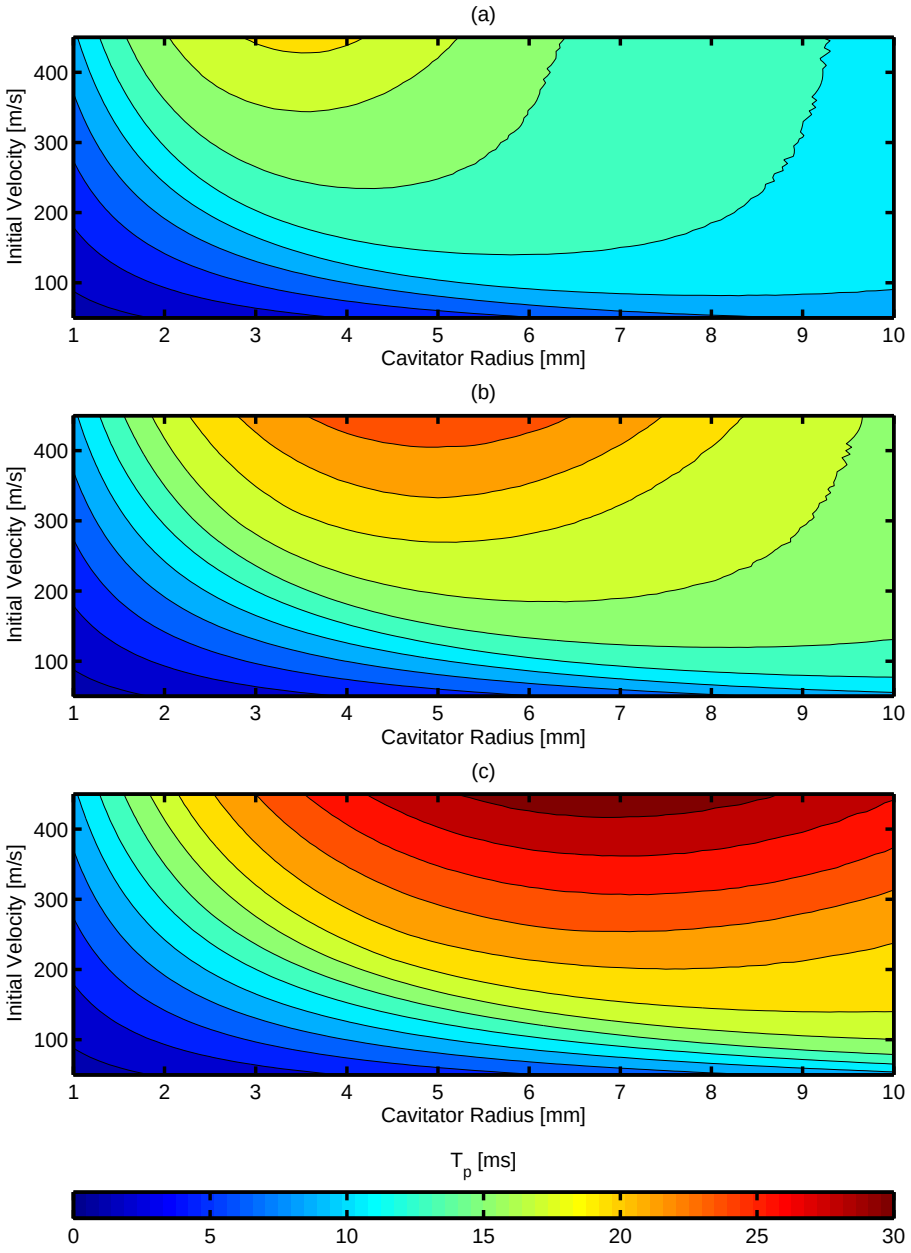

Figure 4.35: Contours of cavity pinch time as a function of cavitator radius and projectile initial velocity for projectile mass of (a) 27.5 g, (b) 55 g, and (c) 110 g. The fluid hydraulic radius is 60 cm and depth is 100 cm. Time is measured relative to the projectile's impact at the free surface.

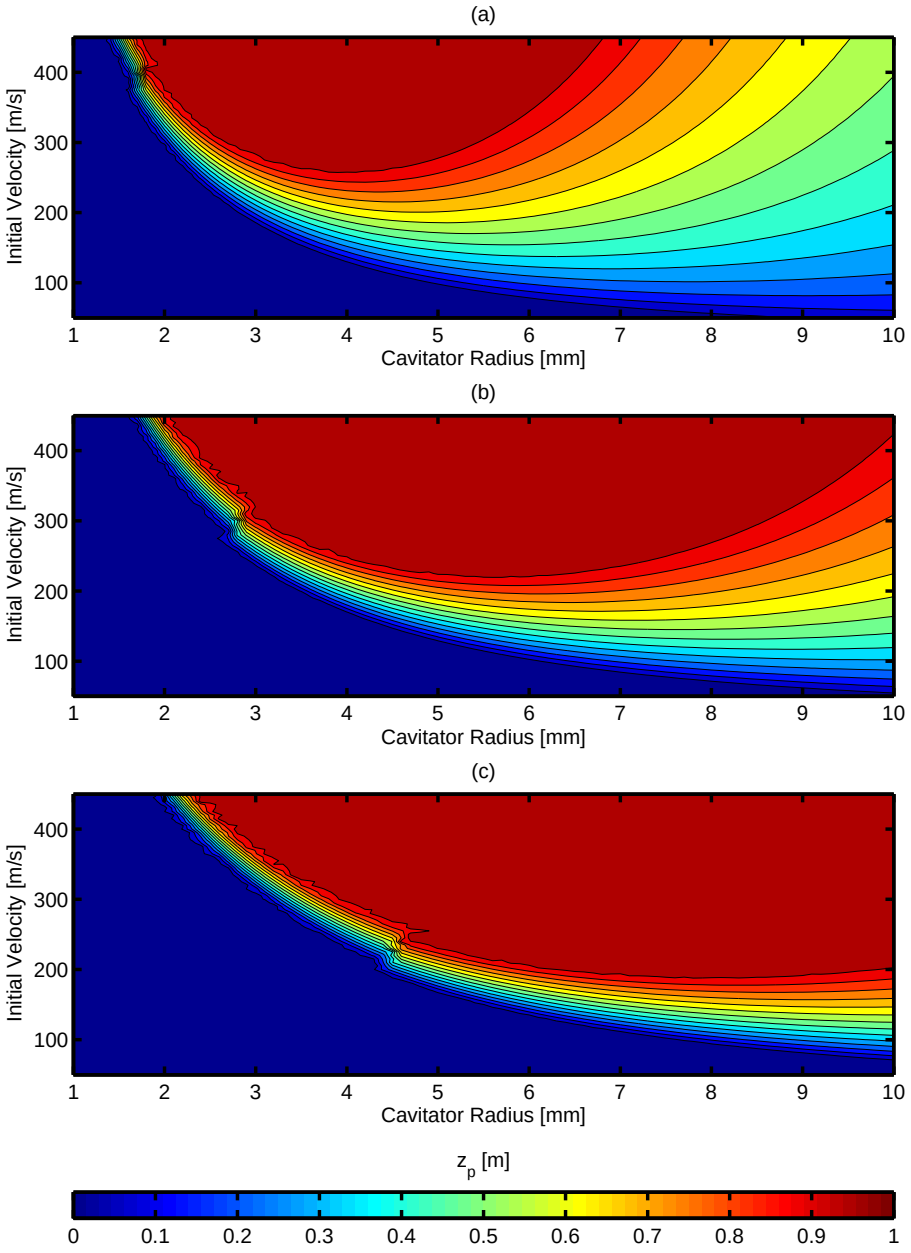

Figure 4.36: Contours of cavity pinch depth as a function of cavitator radius and projectile initial velocity for projectile mass of (a) 27.5 g, (b) 55 g, and (c) 110 g. The fluid hydraulic radius is 60 cm and depth is 100 cm. Depth is measured relative to the free surface.

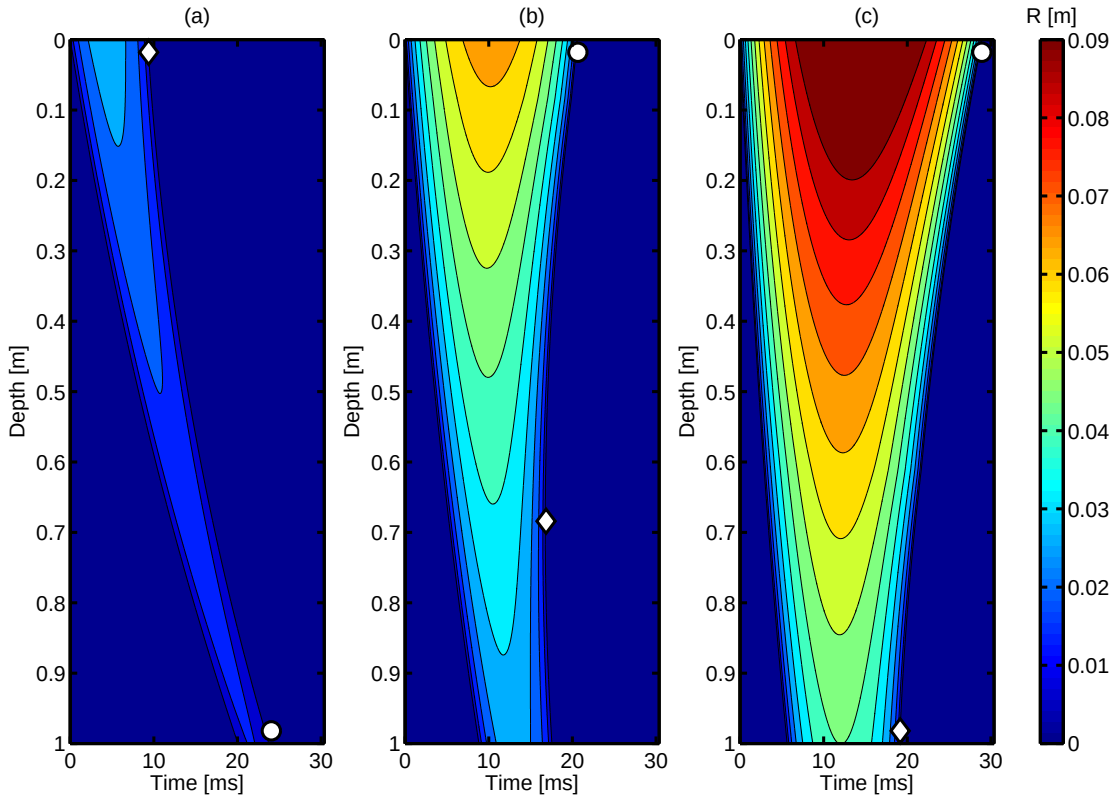

Figure 4.37: Model results for projectile mass, $m_p = 55$ g, and cavitator radius $r_p = 6$ mm with initial velocity V_o of (a) 75 m/s, (b) 175 m/s, and (c) 275 m/s. The fluid hydraulic radius is 60 cm and depth is 100 cm. Cavity pinch time (T_p) and depth (z_p) is marked with a diamond. Cavity collapse time (T_c) and depth (z_c) is marked with a circle.

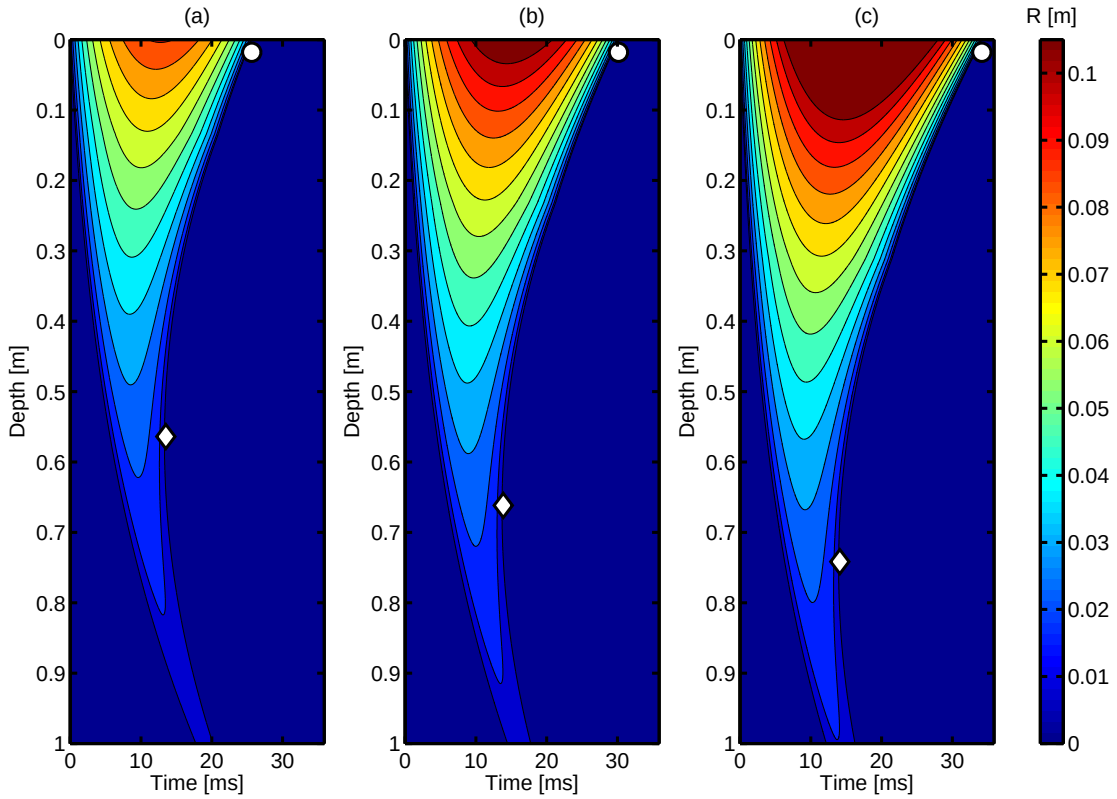

Figure 4.38: Model results for projectile mass, $m_p = 27.5$ g, and cavitator radius $r_p = 6$ mm with initial velocity V_o of (a) 200 m/s, (b) 250 m/s, and (c) 300 m/s. The fluid hydraulic radius is 60 cm and depth is 100 cm. Cavity pinch time (T_p) and depth (z_p) is marked with a diamond. Cavity collapse time (T_c) and depth (z_c) is marked with a circle.

ample a radius of 6 mm and a mass of 27.5 g) cavity pinch time is only weakly dependent on initial velocity, as demonstrated in Figure 4.38. In this region, increases in velocity have a minimal effect on pinch time, increasing from 13.5 ms to 14.1 ms for the 100 m/s change in initial velocity shown. The effect, instead, is primarily on pinch depth, which increases from 56 cm to 74 cm for a 100 m/s change in velocity.

Contours of cavity collapse time and collapse depth are shown in Figures 4.39 and 4.40. The cavity collapse time, T_c, is the time that the overall cavity volume returns to zero. It is the maximum value of the local collapse time, t_c, given by Equation 4.24. The collapse depth, z_c, is the location where the cavity is last open. All three values for m_p display a sharp transition from cavities that collapse at the at the free surface ($z_c = 0$ m) to cavities that collapse at the bottom surface ($z_c = 1$ m). That is to say, this model does not predict cavities that collapse in the middle of the volume, as was observed experimentally. The only exception is when the cavity collapses at the last place the projectile cavitated. This is the transition seen in the lower right corner of Figure 4.40a. The implementation of the model assumes that the projectile no longer cavitates when the maximum cavity radius predicted is less than the cavitator radius at a given depth. As a result, in some cases, the projectile creates a cavity that retracts from the free surface and collapses at the depth that the projectile last cavitated.

An interesting feature of the curves of collapse time is the saddle point for large radii and low velocity, seen most prominently in Figure 4.39a. To the left of the saddle point, for a fixed cavitator radius, the cavity collapse time is not monotonically increasing with velocity. Instead, there is a decrease followed by an increase. This trend is displayed in Figure 4.37. At low velocity (Figure 4.37a), the model shows a cavity with projectile-following behavior, where the cavity is slender and closes shortly after the projectile passes. Near the minimum collapse time for a given radius, such as that shown in Figure 4.37b, the cavity is more tapered, with a larger radius near the free surface. As a result, the cavity collapses

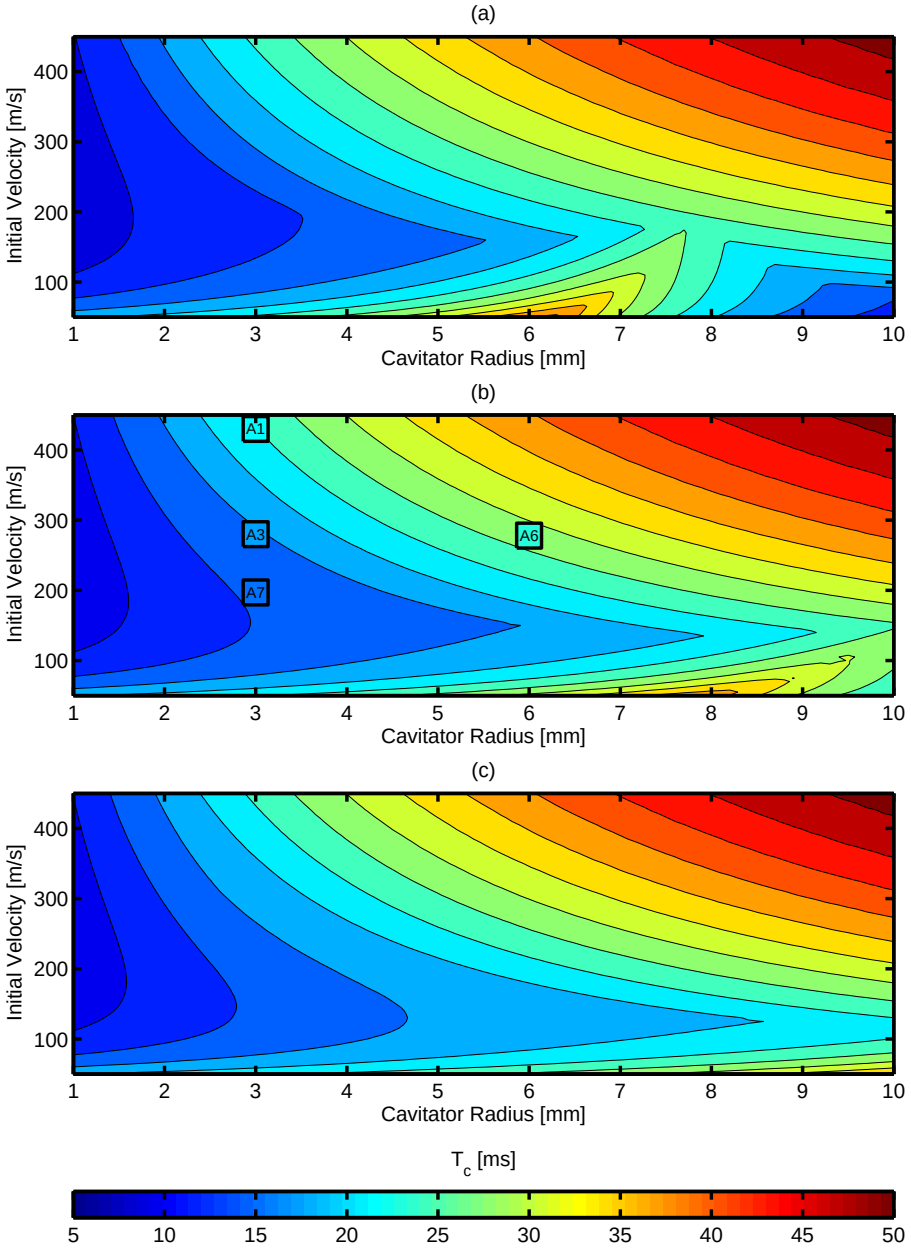

Figure 4.39: Contours of cavity collapse time as a function of cavitator radius and projectile initial velocity for projectile mass of (a) 27.5 g, (b) 55 g, and (c) 110 g. The fluid hydraulic radius is 60 cm and depth is 100 cm. Time is measured relative to the projectile's impact at the free surface. Squares representing experimental data are shown color-matched to contour data.

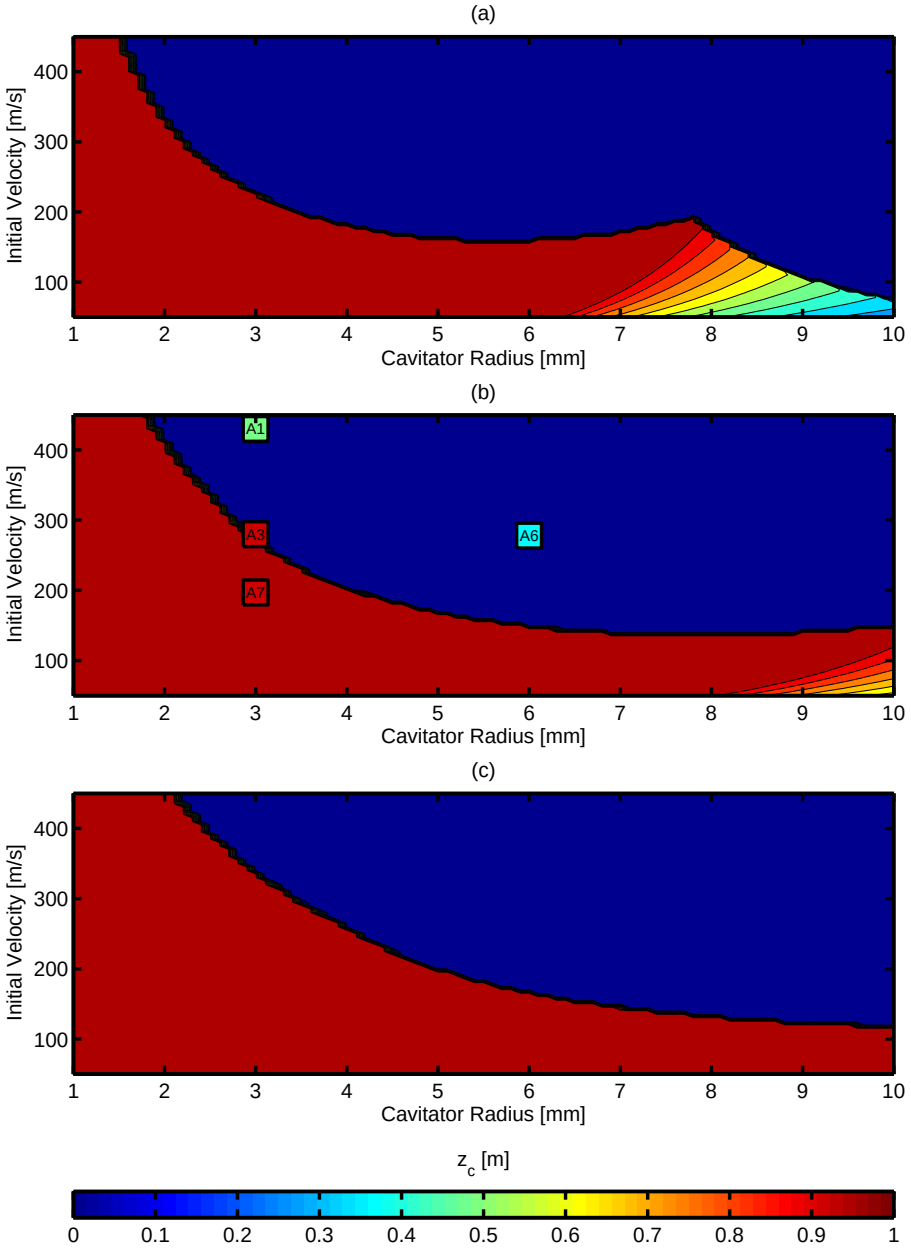

Figure 4.40: Contours of cavity collapse depth as a function of cavitator radius and projectile initial velocity for projectile mass of (a) 27.5 g, (b) 55 g, and (c) 110 g. The fluid hydraulic radius is 60 cm and depth is 100 cm. Depth is measured relative to the free surface. Squares representing experimental data are shown color-matched to contour data.

Table 4.8: Cavity collapse time (T_c) and collapse depth (z_c) for test data compared to model results.

Test	T_c [ms]		z_c [m]	
	Test	Model	Test	Model
A1	21.4	25.2	0.48	0.00
A3	17.3	17.2	0.92	0.99
A6	23.0	29.1	0.36	0.00
A7	15.1	15.0	0.92	1.00

nearly simultaneously along much of its length, leading to a short collapse time. At higher velocities, the cavity's taper is more pronounced, with a broad upper surface that is open long after the bottom has collapse, as demonstrated in Figure 4.37c. To the right of the saddle point, at low velocities, the projectile stops cavitating at some intermediate point in the volume, leading to a shorter collapse time and a collapse depth somewhere in the middle of the volume, as seen in Figure 4.40a.

Figures 4.39 and 4.40 also show markings denoting the cavity collapse time and depth, respectively, from the four test cases presented. A comparison of model results to test data is shown in Table 4.8. The squares are color-matched to contours of model results. Similar quantities are not as useful when considering the pinch time and depth because surface seal present experimentally causes the cavity to close at the free surface first in every case.

The model does a good job predicting collapse time for Tests A3 and A7, with error less than 5%. These are the two cases that collapse in a primarily radial "zipper-like" fashion, as is demonstrated in Figure 4.41. Error for Tests A1 and A6 is larger, on the order of 15 to 25%. These two cases collapsed in a primarily axial fashion, as seen in Figure 4.41, implying that three-dimensionality, in the form of axial motion of the cavity apex, played a role in determining cavity collapse time.

Test A3 appears to be very close to the curve dividing collapse at the free

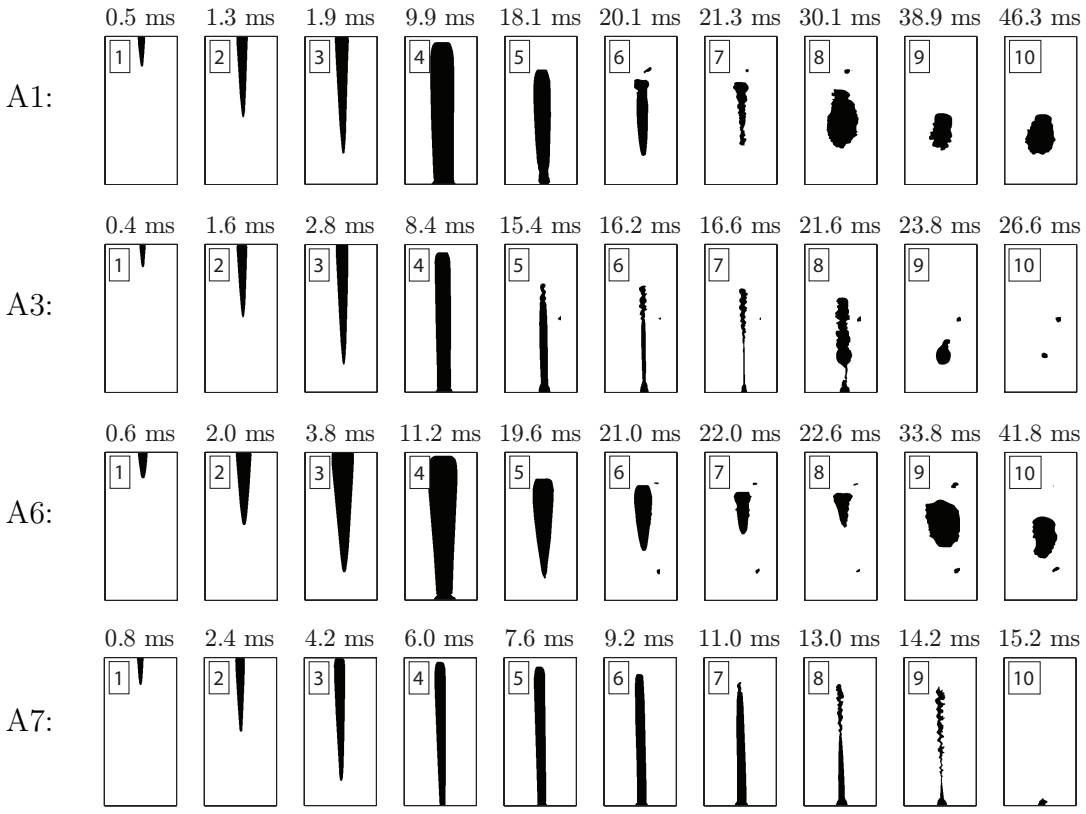

Figure 4.41: Instantaneous cavity contours extracted from high-speed video footage for all four test cases showing cavity growth, retraction from the free surface, collapse, and rebound (where present).

surface and collapse at the bottom. Observing the cavity behavior, it can be seen that it does appear to collapse nearly simultaneously through a significant portion of the depth (see times 6 through 8 in Figure 4.41). This suggests that a slight modification of the test parameters (i.e. initial velocity, mass, or cavitator radius) would lead to a shift in cavity behavior. For example, increasing initial velocity slightly would lead to a bottom-up collapse, more like Test A1, while a slight decrease in initial velocity would lead to a more pronounced top-down collapse, similar to Test A7.

Comparison of the experimental collapse depth to model predictions suggests similar conclusions about the effect of local three-dimensionality. The model agrees well with Tests A3 and A7, predicting a top-to-bottom collapse. For Tests A6 and A7, the model predicts a bottom-up collapse at the free surface. In reality, these two cases collapsed at some location nearer to the middle of the volume. The experimental results suggest that the local three-dimensional effects, surface seal in particular, are responsible for controlling the collapse depth in these cases. Here, the cavity detaches from the bottom surface and travels upward, meeting the upper surface of the cavity at some point in the middle of the volume that is determined my the amount of axial motion following surface seal.

4.9.2 Effect of Hydraulic Radius

To demonstrate the potential ramifications of confinement, we turn briefly to an exploration of the effect of hydraulic radius. Figures 4.42 and 4.43 show model results compared to experiment for Test A3. Three tank sizes were considered: 30 cm, 60 cm, and 120 cm, where 60 cm matches the hydroballistics tank used in the experiments. As expected, the local collapse time scales with hydraulic radius, as seen in Figure 4.42. For the smaller tank, collapse times are shorter as compared to experiment. For the larger tank, collapse takes longer.

More interesting, perhaps, is the change in total collapse behavior. In the experiment, the cavity collapsed in a largely top-down fashion, with nearly a third

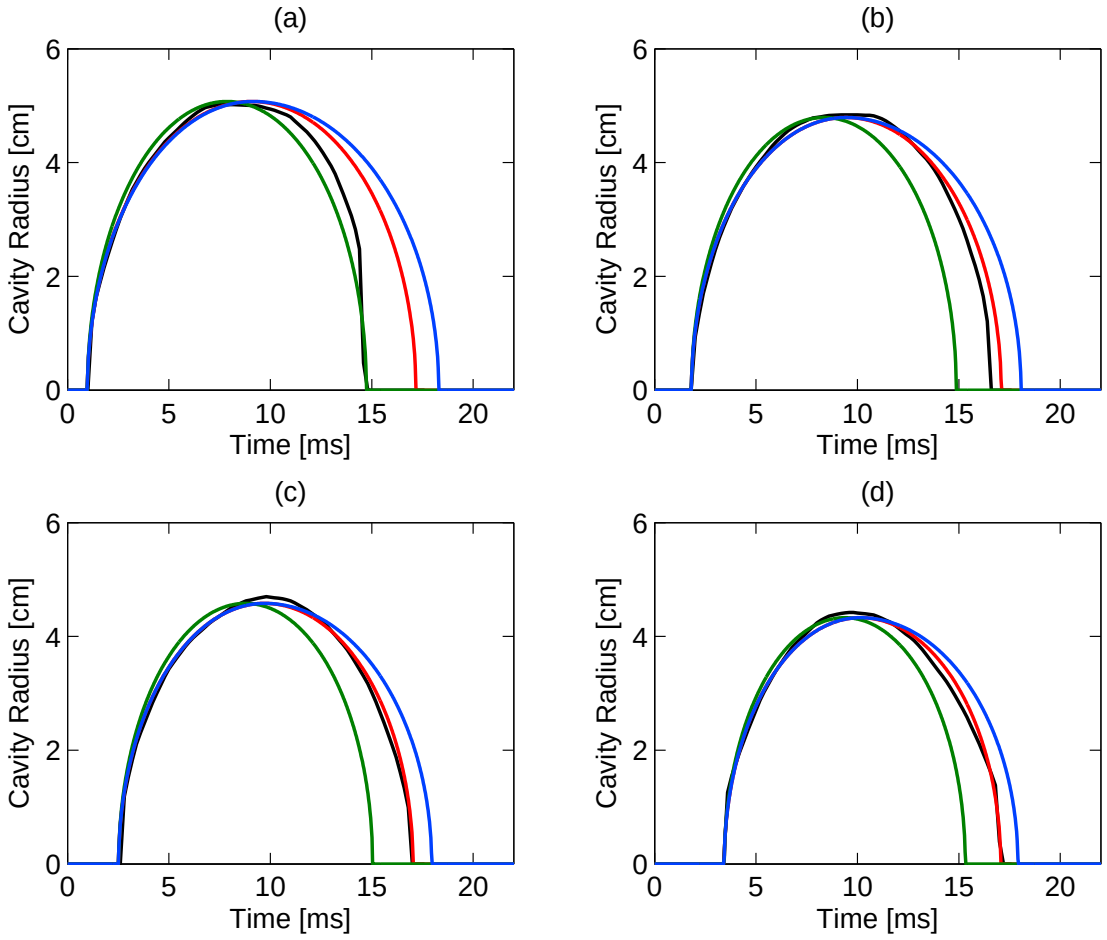

Figure 4.42: Cavity radius histories for Test A3. Experimental data is shown in black. Model results are shown for hydraulic radii of 30 cm (green), 60 cm (red), and 120 cm (blue). Slices are taken at depths of (a) 25 cm, (b) 45 cm, (c) 65 cm and (d) 85 cm.

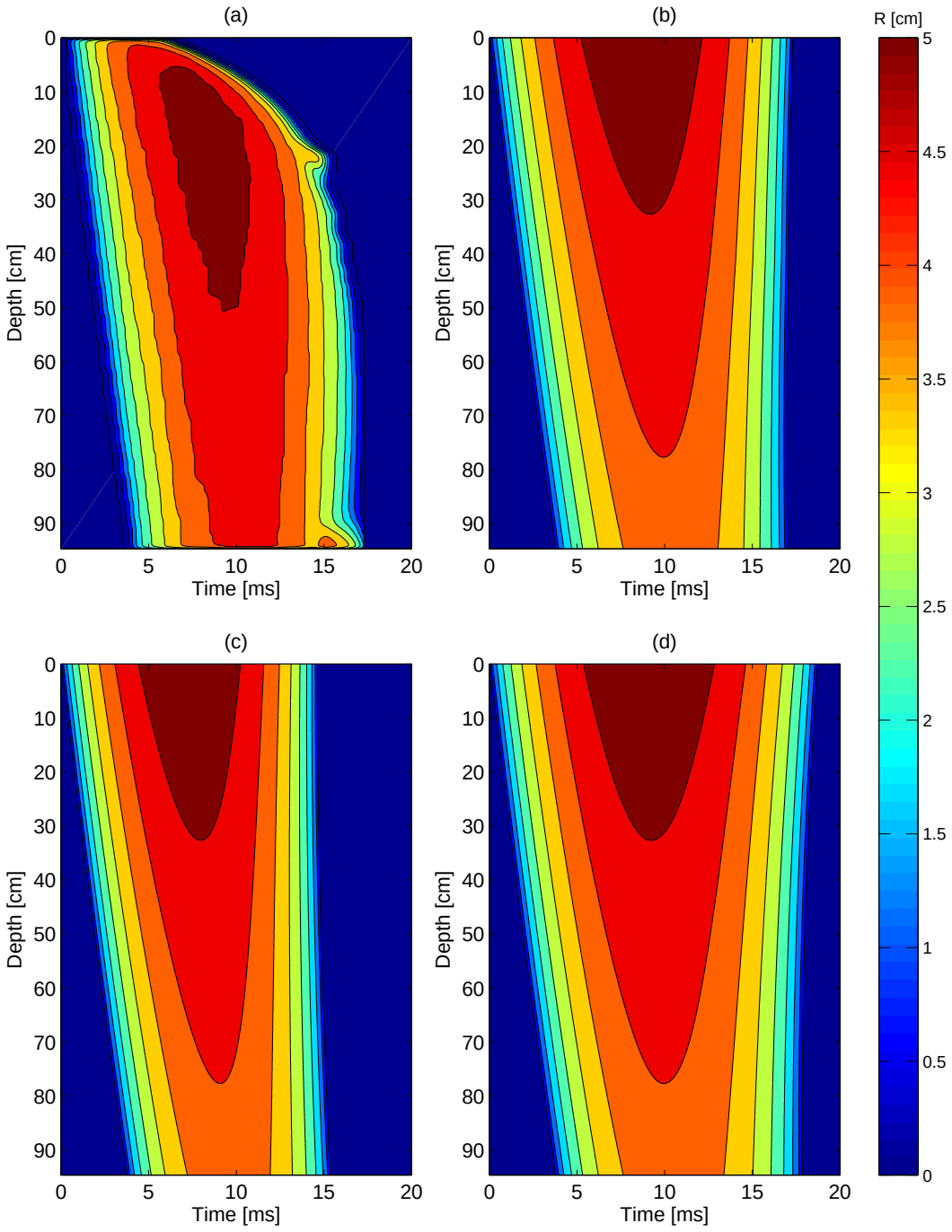

Figure 4.43: Cavity radius contours for Test A3 as a function of time and depth for (a) experimental data, model with (b) 60 cm hydraulic radius tank, (c) 30 cm hydraulic radius tank, and (d) 120 cm hydraulic radius tank.

of the length collapsing simultaneously, as seen in Figure 4.42a. This is replicated by the model with a 60 cm hydraulic radius (Figure 4.42b). For a smaller tank (Figure 4.42c), the top-down collapse behavior is even more pronounced, with the cavity following the projectile and no longer collapsing simultaneously throughout the depth, more akin to what was observed in Test A7. For a larger tank (Figure 4.42d), we see a reversal of this behavior, with the cavity pinching off near the bottom of the tank and collapsing upward, in a fashion similar to that seen in Test A1. This demonstrates the potential for tank size to play a large role in cavity behavior. In this case, we see that it can effect not only the collapse time, both on a local and global scale, but also change the cavity collapse behavior, shifting from top-down to bottom-up collapse. This has the potential to change the loads seen by structures in the vicinity of the cavity.

4.10 Conclusions

This chapter presented the results of an experimental study of the dynamics of the cavity created by a small supercavitating projectile entering shallow water at velocities of 194 m/s to 434 m/s. Pressures along the axis of penetration and near the impact site at the bottom of the tank were recorded with piezoelectric transducers. Cavity profiles were extracted from 5 kHz high-speed video to facilitate the analysis of local and gross cavity behavior.

The resulting data was compared to existing models by Lee et al. [3], and Bergmann et al. [2]. With some adjustments and consideration of tank wall effects, the adapted form of the Bergmann model predicts cavity dynamics well where the flow is primarily radial and local three-dimensional effects, such as surface seal are not dominant.

We find that, for the experimental data presented here, considering the hydraulic radius of the experimental tank greatly improves model results. This implies that the hydroballistics tank selected for this series of experiments influenced

cavity dynamics, potentially artificially shortening the collapse time. Further experiments in a larger tank are required to determine appropriate values for β_e and β_c for an effectively unbounded fluid for the parameter space covered by this work.

Further improvement could be gained by modeling projectile rotational motion, which is currently neglected. This would allow effects such as cavity impact to be considered, yielding an better prediction of cavity radius. For conditions where the cavity is larger relative to the length of the projectile, the magnitude of rotations due to oblique impact (as in Test A1) will be larger, meaning these considerations may be necessary to adequately model projectile trajectory. When modeling supercavitating bodies with actively-controlled cavitators, inclusion of body rotation would be mandatory.

Chapter 5

Summative Discussion

This work has idealized the cavity generated by a supercavitating projectile by assuming that the flow is composed of discrete uncoupled layers of incompressible fluid. The behavior of the actual flow can be controlled by some combination of three effects

First, the behavior can be volume-limited, which is to say that the flow is influencing all of the fluid "available" for motion. In the context of the experimental results presented in Chapter 4, this length scale is the hydraulic radius of the hydroballistics tank.

Another possibility is that the flow is compressibility-limited. In this case, the volume of the ambient fluid participating in the motion is set by the sound speed. When the cavity is first set into motion, an acoustic wave is radiated outward from the cavity wall. Ahead of the wave, the fluid is still stationary. Behind it, the cavity collapse motion has generated a finite radial velocity in the fluid. The amount of fluid available for the motion is set by how much has been set into motion by the acoustic wave.

The other possible modification is a breakdown of the one-dimensional flow assumption when there is a coupling between axial flow and radial flow. In this case, the flow at the leading edge and tail of the cavity create a limit on the participating volume. This causes, the flow looks like a one-dimensional collapsing cylinder in the inner region near the cavity wall. Further away, the flow resembles a dipole plus its image in the free surface. In their work, Bergmann et al. [2] use the parameter β to set the length scale defining inner and outer regions.

With the modeling and analysis presented here, we can begin to evaluate the

Table 5.1: Minimum and maximum dimensionless domain sizes for the four experimental cases presented in Chapter 4.

	$S^\star_{min}$	$S^\star_{max}$
A1	8.0	9.4
A3	11.4	12.7
A6	6.4	11.2
A7	16.7	20.8

relative magnitude of each of these effects for the experiments presented. The compressibility-limited collapse time can be found directly by evaluating the empirical fit given by Equation 3.23 for a driving pressure difference of 98.3 kPa. This gives a dimensionless collapse time of 2.34. Using Equation 3.14, the critical domain size, $S^\star_{crit}$, is then 175.

Observed minimum and maximum values for $S^\star$ are shown for all four test cases in Table 5.1. Here, the minimum, $S^\star_{min}$, is the hydraulic radius of the tank, 60 cm, divided by the maximum cavity radius. The maximum, $S^\star_{max}$, is the hydraulic radius divided by the minimum value of the local cavity maximum radius, that is to say the maximum radius of the cavity at its most slender point. We see that in all four cases, the value of $S^\star$ is well below the critical value of 175 required for fluid compressibility to control the behavior. This indicates that the cavity dynamics were possibly determined by the volume of the tank.

We could also try to roughly gage the effect of radial-axial flow coupling. Considering the contraction phase of the model discussed in Section 4.8, where the cavity collapses from its maximum, R_{max}, to zero, we have

$$R(z,t) = \sqrt{R^2_{max} - \frac{\Delta P}{\rho \beta_c} t^2}, \tag{5.1}$$

where $\beta_c = \log(S/R_{max})$. At the collapse time, $t = T_c$, the radius goes to zero,

giving

$$T_c = \sqrt{\frac{\rho\beta}{\Delta P} R_{max}^2}. \tag{5.2}$$

Applying the dimensionless collapse time (Equation 3.21) yields the succinct

$$T_c^\star = \sqrt{\beta} \tag{5.3}$$

Recklessly extrapolating the data presented by Bergmann et al. [2] suggests a first estimate for β_c of approximately 6, as seen in Figure 4.22. Evaluating, this gives a coarse estimate of 2.4 for the critical collapse time. Applying Equation 3.14, the critical domain size, $S_{crit}^\star$, is 182. This implies that if the flow were not influenced by the size of the hydroballistics tank, there may be a near balance between radial-axial flow coupling and compressibility in this case.

Future work should consider experiments conducted in hydroballistics tanks of varying hydraulic radius to evaluate this possibility. This would allow for further understanding of the compressibility-limited cavity collapse behavior in a very large fluid domain, providing an appropriate upper bound for the value of β analogous to those reported by Bergmann et al. [2] at lower Froude number. It would also facilitate observation of the effect of radial-axial flow coupling effects on collapse behavior.

Bibliography

[1] J. M Aristoff and J. W. Bush. Water entry of small hydrophobic spheres. *Journal of Fluid Mechanics*, 619:45, 2009.

[2] R. Bergmann, D. van der Meer, S. Gekle, A. van der Bos, and D. Lohse. Controlled impact of a disk on a water surface: cavity dynamics. *Journal of Fluid Mechanics*, 633:381–409, 2009.

[3] M. Lee, R. G. Longoria, and D. E. Wilson. Cavity dynamics in high-speed water entry. *Physics of Fluids*, 9(3):540–550, March 1997.

[4] M. P. Felix and A. T. Ellis. Laser-induced liquid breakdown-a step-by-step account. *Applied Physics Letters*, 19(11):484–486, 1971. doi: 10.1063/1.1653783.

[5] W. Lauterborn. High-speed photography of laser-induced breakdown in liquids. *Applied Physics Letters*, 21(1):27–29, July 1972.

[6] G. Birkhoff and F. H. Zarantanello. *Jets Wakes and Cavities*. Academic, New York, 1957.

[7] R. H. Cole. *Underwater Explosions*. Princeton University Press, Princeton, New Jersey, 1948.

[8] C. Herring. Theory of the pulsations of the gas bubble produced by an underwater explosion. Technical Report OSRD Report 236, Naval Surface Warfare Center Indian Head Division, 1941.

[9] Lord Rayleigh. On the pressure developed in a liquid during the collapse of a spherical cavity. *Phil. Mag.*, 34(200):94–98, 1917.

[10] J. B. Keller and I. I. Kolodner. Damping of underwater explosion bubble oscillations. *Journal of Applied Phys*, 27(10):1152–1161, October 1956.

[11] A. Prosperetti and A. Lezzi. Bubble dynamics in a compressible liquid. Part 1. First-order theory. *Journal of Fluid Mechanics*, 168:457–478, 1986.

[12] A. Lezzi and A. Prosperetti. Bubble dynamics in a compressible liquid. Part 2. Second-order theory. *Journal of Fluid Mechanics*, 185:289–321, 1987.

[13] A. Prosperetti. Bubbles. *Physics of Fluids*, 16(6):1852–1865, June 2004.

[14] D. Lohse, R. Bergmann, R. Mikkelsen, C. Zeilstra, D. van der Meer, M. Versluis, K. van der Weele, M. van der Hoef, and H. Kuipers. Impact on soft sand: Void collapse and jet formation. *Physical review letters*, 93(19):198003, 2004.

[15] R. Bergmann, D. van der Meer, M. Stijnman, M Sandtke, A. Prosperetti, and D. Lohse. Giant bubble pinch-off. *Physical Review Letters*, 96(15):154505, April 2006.

[16] A. J. Walton and G. T. Reynolds. Sonoluminescence. *Advances in Physics*, 33(6):595–660, 1984.

[17] M. P. Brenner, S. Hilgenfeldt, and D. Lohse. Single-bubble sonoluminescence. *Rev. Mod. Phys.*, 74(2):425–484, May 2002. doi: 10.1103/RevModPhys.74.425.

[18] M. S. Plesset and A. Prosperetti. Bubble dynamics and cavitation. *Annual Review of Fluid Mechanics*, 9:145–185, 1977.

[19] S. Fujikawa and T. Akamatsu. Effects of non-equilibrium condensation of vapor on the pressure wave produced by the collapse of a bubble in a liquid. *Journal of Fluid Mechanics*, 97:481–512, 1980.

[20] A. M. Worthington and R. S. Cole. Impact with a liquid surface, studied by the aid of instantaneous photography. *Philosophical Transactions of the Royal Society of London A*, 189:137, 1897.

[21] A. M. Worthington and R. S. Cole. Impact with a liquid surface studied by the aid of instantaneous photography. Paper II. *Philosophical Transactions of the Royal Society of London A*, 194:175–199, 1900.

[22] D. Gilbarg and R. A. Anderson. Influence of atmospheric pressure on the phenomena accompanying the entry of spheres into water. *Journal of Applied Physics*, 19:127, 1948.

[23] A. May and J. C. Woodhull. The virtual mass of a sphere entering water vertically. *Journal of Applied Physics*, 21:1285, 1950.

[24] A. May. Effect of surface condition of a sphere on its water-entry cavity. *Journal of Applied Physics*, 22:1219, 1951.

[25] A. May. Vertical entry of missiles into water. *Journal of Applied Physics*, 23: 1362, 1952.

[26] V. Duclaux, F. Caillé, C. Duez, C. Ybert, L. Bocquet, and C. Clanet. Dynamics of transient cavities. *Journal of Fluid Mechanics*, 591(1):1–19, 2007.

[27] J. M. Aristoff, T. T. Truscott, A. H. Techet, and J. W. M. Bush. The water entry of decelerating spheres. *Physics of fluids*, 22:032102, 2010.

[28] T. T. Truscott and A. H. Techet. Water entry of spinning spheres. *Journal of Fluid Mechanics*, 625:135–165, 2009.

[29] M. M. Mansoor, J. O. Marston, I. U. Vakarelski, and S.T. Thoroddsen. Water entry without surface seal: extended cavity formation. *Journal of Fluid Mechanics*, Under Consideration.

[30] H. H. Shi, M. Itoh, and T. Takami. Optical observation of the supercavitation induced by high-speed water entry. *Journal of fluids engineering*, 122(4):806–810, 2000.

[31] H. H. Shi and T. Takami. Some progress in the study of the water entry phenomenon. *Experiments in Fluids*, 30(4):475–477, 2001.

[32] H. H. Shi and M. Kume. An experimental research on the flow field of water entry by pressure measurements. *Physics of Fluids*, 13(1):347–349, 2001.

[33] H. H. Shi and M. Itoh. High-speed photography of supercavitation and multiphase flows in water entry. In *Proceedings of the 7th International Symposium on Cavitation*, 2009.

[34] Y. N. Savchenko. Supercavitation: Problems and perspectives. In *CAV 2001: Fourth International Symposium on Cavitation*. California Institute of Technology, 2001. URL `http://resolver.caltech.edu/CAV2001:lecture.003`.

[35] Y. N. Savchenko. Control of supercavitation flow and stability of supercavitating motion of bodies. Technical Report ADP012083, Defense Technical Information Center Report, 2001.

[36] I. N. Kirschner, N. E. Fine, J. S. Uhlman, and D. C. Kring. Numerical modeling of supercavitating flows. In *RTO AVT Lecture Series on "Supercavitating Flows"*, February 2001.

[37] D. Riabouchinsky. On steady fluid motion with a free surface. *Proceedings of the London Mathematical Society*, 19:206–215, 1920.

[38] C. E. Brennen. *Cavitation and Bubble Dynamics*. Oxford University Press, 1995.

[39] R. A. Handelsman and J. B. Keller. Axially symmetric potential flow around a slender body. *Journal of Fluid Mechanics*, 28(1):131–147, 1967.

[40] M. Lee. *Generation of shock waves by a body during high-speed water entry.* PhD thesis, Department of Mechanical Engineering, The University of Texas at Austin, December 1995.

[41] H. N. Oğuz and A. Prosperetti. Dynamics of bubble growth and detachment from a needle. *Journal of Fluid Mechanics Digital Archive*, 257:111–145, 1993.

[42] E. A. Lundstrom. Fluid dynamic analysis of hydraulic ram. Technical Report NWC TP 5227, Naval Surface Weapons Center, China Lake, CA, July 1971.

[43] A. Wardlaw, J. A. Luton, J. Renzi, K. Kiddy, and R. McKeown. The Gemini euler solver for the coupled simulations of underwater explosions. Technical Report IHTR 2500, Naval Surface Warfare Center Indian Head Division, Indian Head, MD 20640-5035, November 2003.

[44] S. K. Godunov. A finite difference method for the numerical computation of discontinuous solutions of the equations of fluid dynamics. *Mat. Sb*, 47(3): 271–290, 1959.

[45] B. van Leer. Towards the ultimate conservative differences scheme, V. A second order sequel to Godunov's methods. *Journal of Computational Physics*, 32:101–136, 1979.

[46] P. Colella. A direct Eulerian MUSCL scheme for gas dynamics. *SIAM Journal on Scientific and Statistical Computing*, 6:104, 1985.

[47] W. F. Noh and P. Woodward. SLIC (Simple Line Interface Calculation). In *Some Methods of Resolution of Free Surface Problems*, volume 59 of *Lecture Notes in Physics, Berlin Springer Verlag*, pages 330–340, 1976.

[48] J. H. Tillotson. Metallic equations of state for hypervelocity impact. Technical Report Naval Surface Weapons Center, 1962.

[49] D. Epstein and J. B. Keller. Expansion and contraction of planar, cylindrical, and spherical underwater gas bubbles. *The Journal of the Acoustical Society of America*, 52(3B):975–980, 1972.

[50] A. Prosperetti. The question of bubble dynamics in a compressible liquid. *Physics of Fluids*, 30(11):3626–3628, November 1987.